Observatoire cantonal de Neuchâtel - Université de Neuchâtel

# An intense, highly collimated continuous cesium fountain

Thèse présentée à la Faculté des Sciences
pour l'obtention du grade de docteur ès sciences
par:

**Natascia Castagna**

Physicienne licenciée de l'Università di Torino (Italie)

acceptée le 20 avril 2006 par les membres du jury:

| | |
|---|---|
| Prof. P. Thomann | Rapporteur |
| Dr. S. Guérandel | Corapporteur |
| Prof. T. Esslinger | Corapporteur |
| Prof. J. Faist | Corapporteur |

Neuchâtel, juillet 2006

**Mots clés**: horloges atomiques, atomes froids, refroidissement et piégeage d'atomes par laser.

**Keywords**: atomic clocks, cold atoms, laser cooling and trapping.

**Abstract** The realisation of cold and slow atomic beams has opened the way to a series of precision measurements of high scientific interest, as atom interferometry, Bose-Einstein Condensation and atomic fountain clocks. The latter are used since several years as reference clocks, given the high performance that they can reach both in accuracy and stability. The common philosophy in the construction of atomic fountains has been the pulsed technique, where an atoms sample is launched vertically and then falls down under the effect of the gravity. The Observatoire de Neuchâtel had a different approach and has built a fountain clock (FOCS1) operating in a continuous mode. This technique offers two main advantages: the diminution of the undesirable effects due to the atomic density (*e.g.* collisions between the atoms and cavity pulling) and to the noise of the local oscillator (intermodulation effect). To take full advantage of the continuous fountain approach however, we need to increase the atomic flux. The techniques chosen to reach this goal are an efficient transverse collimation together with more atoms to begin with. Here we report on a study of different transverse collimation techniques performed in a two-dimensional phase stable optical lattice (namely gray molasses and magnetically induced laser cooling) as well as the development and characterisation of a 2D-magneto-optical trap used to load the fountain. Best performances are reached in a $2D^+$-MOT configuration of such a pre-source, for which we detect an atomic flux 20 times greater than the one measured when the fountain is loaded by a Cs vapour. This gain could improve the atomic clock stability by a factor 6. An even better stability is expected after introducing a pre-cooling stage before performing the transverse collimation. This new configuration is currently under investigation and will be implemented in a second continuous fountain (FOCS2).

*A ma famille et à Claudio*

Université de Neuchâtel **uni**

# IMPRIMATUR POUR LA THESE

# An intense, highly collimated continuous Cesium fountain

**Natascia CASTAGNA**

UNIVERSITE DE NEUCHATEL

FACULTE DES SCIENCES

La Faculté des sciences de l'Université de Neuchâtel,
sur le rapport des membres du jury

MM. P. Thomann (directeur de thèse),
J. Faist, S. Guérandel (Paris)
et T. Esslinger (ETH Zürich)

autorise l'impression de la présente thèse.

Neuchâtel, le 16 avril 2006

Le doyen :

J.-P. Derendinger

■ **Faculté des Sciences**
■ Rue Emile-Argand 11 ■ CP 158 ■ CH-2009 Neuchâtel
■ Téléphone : +41 32 718 21 00 ■ Fax : +41 32 718 21 03 ■ E-mail : secretariat.sciences@unine.ch ■ www.unine.ch

# Acknowledgments

This work was funded by the Federal Office of Metrology and Accreditation (METAS) in Bern, the Swiss National Science Foundation and the Canton of Neuchâtel.

I would like to thank all my colleagues at the Observatoire cantonal de Neuchâtel for their kind collaboration and support during these four years. Their competence has often been of great help for the evolution of the work presented in this report. Thanks to all the staff, both technicians or physicians.

Thanks to Prof. Tilman Esslinger, Prof. Jerôme Faist and Dr. Stephane Guerandel for accepting to be a member of the jury for the defense of my thesis.

The study of the transverse collimation using a gray molasses or a magnetic field is part of a collaboration with our Russian colleagues Valera Yudin and Aleksei Taichenachev. The scientific discussions that we had with them have been of rare quality: thank you Valera and Aleksei!

Helpful discussions and opinion exchanges have been a constant in the "Cold atoms" team. My education as physician has grown up thanks to my colleagues and friends: Gregor Dudle, Alain Joyet, Alain Jornod, Mark Plimmer, Jocelyne Guéna, Ferenc Füzesi, Gianni Di Domenico and obviously my director of thesis Prof. Pierre Thomann.

I have enjoyed fantastic times with my friends here in Neuchâtel and I am truly grateful to all of them: Ariane, Veronique, Lydie, Carole, Gianni_CH, Gianni_IT, Sylvain, Roger, Yvan, Monique, Patrick, Rudi, Joanna, Marianne, Christoph, Marion and, a bit later, Evelina and Christian. Thanks to François Delaquis for participateing to my public presentation, I am well aware that it has been hard for him!

I am used to work until late at night, but I am not the only one, maybe it is something connected with the DNA of physicists from Torino: thanks to Emiliano for all the time spent together talking about physics and problems in the world at the Chauffage or at the Turquoise (until the day he became vegetarian) or at the Touring!

Thanks to all my friends in Italy for having kept in touch with me and for having offered their precious support with their email or by coming to see me directly here to make sure that I was fine! Amongst them: Marco, Dany,

Carlo, Paola, Roby, Claudio, Stefania, Mauro, Laura, Fabio, Andrea, Fulvia, Gianluca, Eugenio, Valerio, Gian, Sette etc.

Finally, let me thank my family that gave me the opportunity to study, that provided me the needed serenity to help my self-confidence to grow up and that has represented a great example of integrity and respect for the people in general ever since; concept that, after all, is even much important than physics!

# Contents

# Chapter 1

# Introduction

The realisation of cold and slow atomic beams has opened the way to a series of precision measurements of high scientific interest, as atom interferometry [1], Bose-Einstein Condensation (BEC) [2] and atomic fountain clocks [3, 4]. The latter are used since several years as reference clocks, given the high performance that they can reach both in accuracy and stability. The common philosophy in the construction of atomic fountains has been the pulsed technique, where an atoms sample is launched vertically and then falls down under the effect of the gravity. The Observatoire de Neuchâtel (ON) had a different approach and has built a fountain clock (FOCS1) operating in a continuous mode. This technique offers two main advantages: the diminution of the undesirable effects due to the atomic density (*e.g.* collisions between the atoms and cavity pulling) and to the noise of the local oscillator (intermodulation effect).
In this chapter we present the mean characteristics of the fountain clocks and the techniques used to obtain best performances.

## 1.1 Stability and accuracy

The quality of any clock is determined by the value of two parameters: the frequency stability and accuracy.

- The stability of an oscillator is a measurement of the uncertainty in the determination of its frequency after a given integration time $\tau$. The higher the stability, the shorter the time to evaluate the effect of a perturbation.

- The accuracy is a measure of the residual uncertainty with which the S.I. definition of the second is realised in a particular clock. The accuracy is determined by evaluating all the frequency biases and summing the associated uncertainties.

The clock stability is characterised by the Allan deviation $\sigma_y(\tau)$[1] (here $y = \Delta\nu/\nu_0$ are the fractional frequencies averaged over the time interval $\tau$):

$$\sigma_y(\tau) \approx \frac{1}{Q} \cdot \frac{1}{(S/N)} \cdot \frac{1}{\sqrt{\tau}} \cdot \frac{1}{A} \,. \tag{1.1}$$

where $Q$ is the quality factor[2], $(S/N)$ the signal-to-noise ratio, $\tau$ the integration time and $A$ is a factor that depends from the wave used to modulate the detected signal by using the lock-in technique. Typically, $A = \pi$ and, for cold atom fountains, $Q = 10^{10}$. The ratio $(S/N)$ in the shot noise limit is limited by the Poisson deviation of the detected atomic flux and in this limit we can write (see Ref. [5]):

$$(S/N) = \sqrt{\frac{\Phi}{2}} \,. \tag{1.2}$$

Thus one could improve the stability by increasing the atomic flux. This objective can be achieved in two ways: by increasing the flux at the source and by collimating the atomic beam to limit the spread due to the transverse temperature.

## 1.2 Performance of best atomic clocks

In Figs. 1.1 and 1.2 we present a scheme of the two different approaches used to build a fountain atomic clock, respectively the pulsed and the continuous technique. In both, atoms are captured by an optical molasses and launched vertically at a given longitudinal velocity, typically 3-4 m/s. In a pulsed fountain the atomic cloud passes through the microwave cavity (where there is the first $\pi/2$ pulse to induce the clock transition), reaches the apogee in the point where all the kinetic energy is converted in potential energy and then falls down retracing its steps. The beam passes again through the microwave cavity (where the clock transition is completed with the second $\pi/2$ pulse) and it is detected by the fluorescence induced by a probe laser beam. In a continuous fountain the atomic beam traces a parabolic flight, the two passages into the microwave cavity are spatially different and the atoms do not retrace their steps but fall down without superposition with the up-going beam. While in a pulsed fountain after the vertical launch the lasers used to capture the atoms sample are switched off, in the continuous fountain they are always lighted. The frequency accuracy of pulsed fountains is strongly

[1] One of the advantages of the Allan variance $\sigma_y^2(\tau)$ with respect to the classical variance is that the latter diverges for some commonly observed noise processes, such as random walk, *i.e.* the variance increases with increasing number of data points. The Allan variance instead converges for all noise processes observed in precision oscillator.

[2] The quality factor is given by the ratio between the frequency of the atomic transition $\nu_0$ and the FWHM $\Delta\nu$ of the atomic resonance.

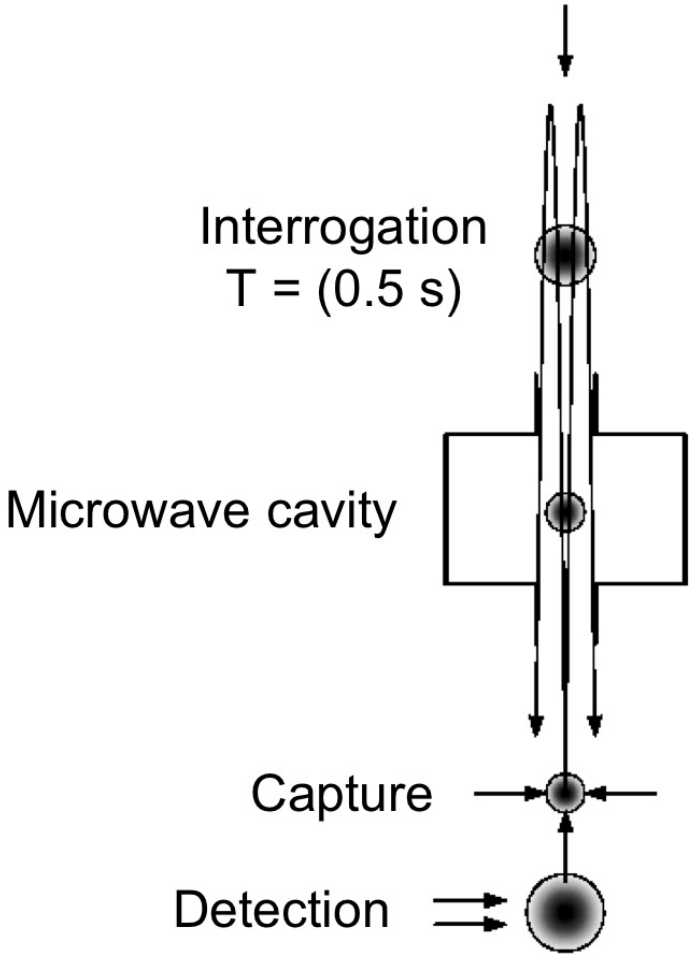


**Figure 1.1**: Scheme of a typical pulsed fountain. The atoms are launched vertically after capture performed using an optical molasses. The ballistic flight is completely characterised by the initial longitudinal velocity and the gravity. The two microwave pulses to induce the clock transition are separated by an interval of typically 0.5 s (that implies a FWHM of the central fringe of 1 Hz). The lasers that create the optical molasses are switched off after the launch and the detection is performed under the capture region.

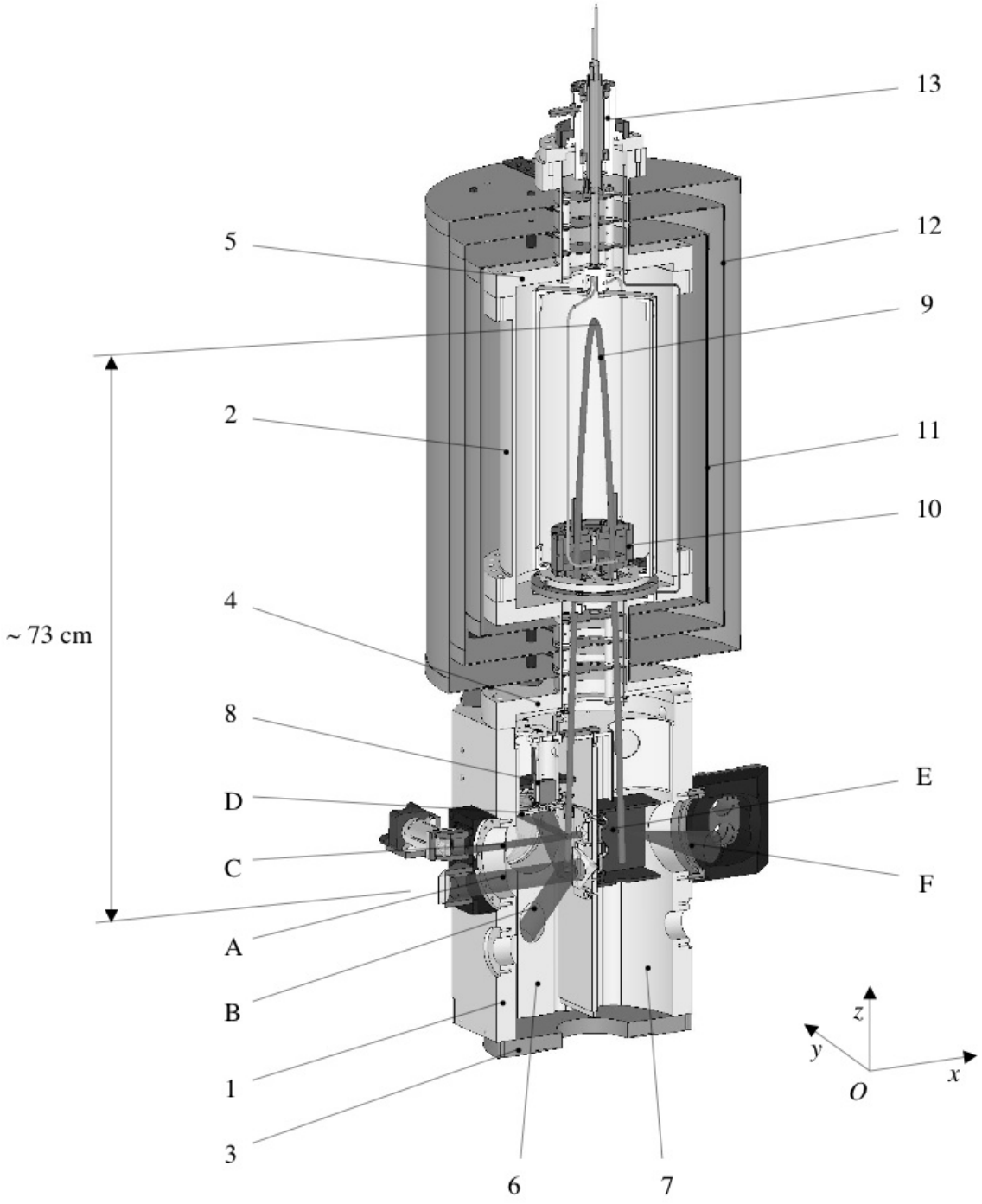


**Figure 1.2**: The continuous fountain FOCS1: 1. Lower module 2. Upper module 3,4,5. Transition flanges 6. Source region 7. Detection region 8. Light trap 9. Atomic beam 10. Microwave cavity 11. C-field 12. Magnetic shields 13. Rotative feedthrough A,B. Optical molasses laser beams C,D. Transverse collimation laser beams E. Detection laser beam F: Fluorescent light.

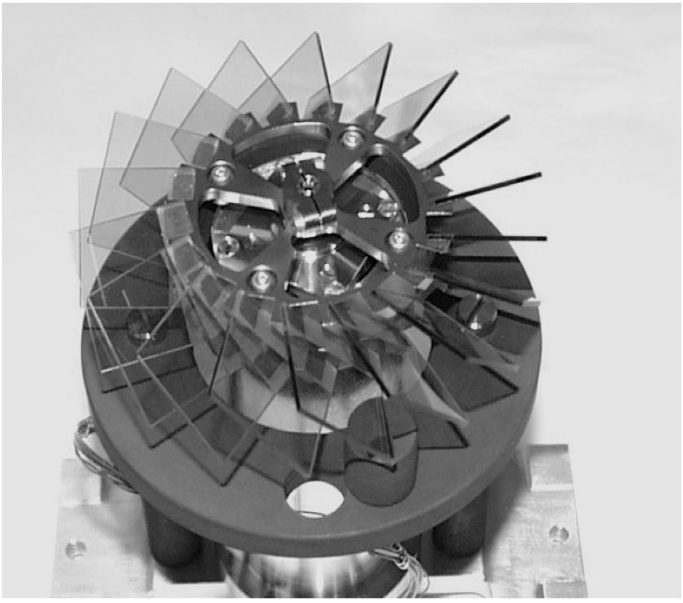

**Figure 1.3**: Picture of the light trap. The aim of this device is an attenuation of a factor $10^4$ of the light seen by the atoms during the interaction with the microwave. With the introduction of the light trap the frequency accuracy of the continuous fountain clock is not limited by the light shift.

affected (and in most cases, limited) by the effect of collisions between the atoms (collisional shift) and generally by atomic density-dependent effects (*e.g.* cavity pulling). The frequency stability is instead limited by the noise of the local oscillator (intermodulation effect, also known as Dick effect). Despite these disadvantages, the best fountain clocks in operation in the world are based on this technique and they reach stabilities in the order of $2{\cdot}10^{-13}$ at 1 s ($10^{-14}$ by using a cryogenic sapphire oscillator, see Ref. [6]) and accuracy of about $10^{-15}$ [4].
In the continuous fountain the atomic density is strongly reduced with respect to the pulsed one for the same average atomic flux and the intermodulation effect is cancelled with an opportune choice of the frequency modulation [7]. The accuracy is however limited by the perturbation due to the light seen by the atoms during the interaction with the microwave and coming from the optical molasses laser beams, always switched on (light shift). To solve this problem a light trap is mounted into FOCS1 (see Fig. 1.2, point 8) to attenuate this light of a factor $\sim 10^4$. More details about this device, shown in Fig. 1.3, in Refs. [8, 9]. The performance of FOCS1, currently under evaluation, is a frequency stability of $2.5{\cdot}10^{-13}$ at 1 s and an expected accuracy of $10^{-15}$. A better stability can be obtained by increasing the detected atomic flux (and without degradation of the accuracy, given the low atomic density); this is the aim of a new continuous fountain FOCS2, under construction. The techniques chosen to increase the detected flux are an efficient

transverse collimation together with more atoms to begin with. Ref. [10] reports on the characterisation of several collimation techniques operating in an optical molasses and realised in an experimental set-up. Other collimation techniques and the development of a pre-source are instead the object of this work and are briefly outlined in the next paragraph.

## 1.3 Outline of this work

- In chapter 2 we present the "state of the art" of the metrology by using cold atomic beams developed at ON: transverse temperatures and atomic fluxes measured with different collimation techniques and in different set-up. We calculate the fraction of the atoms detected from a given sample at the source and without collimation, showing then the effect of a low transverse temperature and its impact on the frequency stability. We calculate finally the factor that we can gain in flux before being limited by the collisional shift.

- In chapter 3 the experimental set-up used for investigating two collimation methods in an optical lattice is described. It is a vacuum system divided in modules and whose geometry is similar to the one of FOCS1. We use this set-up to study new techniques of cooling that could be implemented in FOCS2 and eventually retrofitted in FOCS1; the optical access to the atomic beam allows one to perform a complete diagnostic. All laser beams are prepared on an optical table and transported to the experimental set-up through polarisation-maintaining optical fibres.

- Chapter 4 presents the first collimation technique studied. We perform a laser cooling in a two-dimensional optical lattice with a polarisation gradient (we use a lin$\perp$lin configuration). We have studied a particular type of molasses, known as *gray molasses*, which has the advantage of accumulating the atoms in a dark state (a state that is not coupled to the light field) and for this reason the fluorescence emitted in the process is strongly reduced in comparison with the well known Sisyphus cooling. The atom cooling is obtained through a state coupled to a light field whose frequency is in the blue side of the atomic resonance; the atoms climb the potential hill, loosing their kinetic energy, and when they reach the top of the hill the optical pumping puts them into the non-coupled state. The repopulation of the coupled state (Zeeman mixing) is obtained by motional coupling: the atoms travel in a region where they become coupled to the light field, due to the position-dependent polarisation, and the cooling cycle starts again. With this technique we have reached a transverse temperature of 3.5 $\mu$K, while without collimation the measured transverse temperature was of 60 $\mu$K.

This reduction in temperature is translated in a flux increment by a factor ∼20.

- Chapter 5 presents the second collimation technique that we have implemented and characterised. It is known as *Magnetically Induced Laser Cooling* (MILC) and for certain aspects is very similar to the gray molasses cooling technique. There are again a state that is not coupled to the light field (whose frequency is in the blue of an atomic resonance) and a state that is sensitive to the light shift. The cooling cycle follows the same steps as in gray molasses, but here the Zeeman mixing is performed by an applied transverse static magnetic field. The two-dimensional optical molasses has no polarisation gradient (we use a lin‖lin configuration). With this technique we have obtained transverse temperatures as low as 5 $\mu K$, which means a gain in the detected flux by a factor 12.

- In chapter 6 we characterise a two-dimensional magneto-optical trap, used as *pre-source* to load the experimental fountain. The latter was until now fed by a cesium vapour; the production of a slow atomic beam is a widely employed technique to obtain a bigger atoms sample as source. The flux detected when the fountain is loaded by the pre-source shows a gain of a factor 20 with respect to the cesium vapor loading technique. Note that when we use the pre-source we can not perform the transverse collimation, the lasers needed for the latter being used for the former.

- In chapter 7 we summarise the results obtained in this work and we present some perspectives for future investigations, as the implementation of a pre-cooling step in the same optical lattice where we perform the transverse collimation. In the past we have studied the Zeeman-shift Raman sideband cooling [10], obtaining low temperatures but also a low atomic flux. We have also searched for a sign of Stark-shift Raman sideband cooling [11], with promising preliminary results. We attribute the partial failure of these cooling techniques to the still too high initial temperature of the atoms, because of which most of them are not captured into the potential wells of the optical lattice. We think that a pre-cooling step could improve the capture process and give a high atomic flux together with a low transverse temperature.
  We present also possible solutions for the intermodulation effect that becomes not negligible given the obtained gain in flux and calculate the light shift at the detection to be sure that we do not need a second light trap once the pre-source and a high performing collimation technique will be implemented in FOCS2.

# Chapter 2

# Cold atomic beams at ON

In this chapter we present the results obtained for different cooling techniques implemented either in the experimental fountain FOCS-X (see Chap. 3) or in FOCS1; we compare the measured atomic fluxes and from them we calculate the frequency stability associated with this flux.

## 2.1 Past work at ON

In the past 6 years various two-dimensional cooling techniques have been studied at the Observatoire Cantonal de Neuchâtel. In FOCS1 the implemented collimation mechanism is the Sisyphus cooling, realised with two independent laser beams in the classical polarisation configuration $\sigma^+ - \sigma^-$ (see Ref. [9, 8]). By using this technique we have reached a transverse temperature after collimation of 6-7 $\mu$K. Successively we have begun to work on FOCS-X with optical lattices built by a folded laser beam whose power is recycled; the advantage of this choice is the phase stability (Ref. [12, 13]) and the deep potential wells that allow an efficient atom cooling. In such a two-dimensional optical lattice we have performed first the Sisyphus cooling [10] and then the Zeeman-shift degenerate Raman sideband cooling [14]. With the former we have obtained a temperature as low as 3.6 $\mu$K and a detected atomic flux density of $36\times10^{10}$ at$\cdot$s$^{-1}\cdot$m$^{-2}$, while the latter yields a lower final transverse temperature (we have reached 1.6 $\mu$K) but is less efficient concerning the number of atoms captured inside the potential wells (only $7\times10^{10}$ at$\cdot$s$^{-1}\cdot$m$^{-2}$, a factor 5 smaller if we compare with the Sisyphus cooling). These results are summarised in Tab. 2.1 together with the detection area and the detected atomic flux (given by the detected flux density $\times$ the detection area).

From the values of the detected atomic flux presented into the Tab. 2.1 it is possible to evaluate the frequency stability using the Eq. 1.1, taking into account that only the atoms in the Zeeman sub-level $m_F$=0 contribute to the real detected flux in a fountain clock. Thus, dividing by 7 and taking a quality

**Table 2.1**: Comparison of the results obtained with a two-dimensional transverse collimation performed in FOCS1 or in FOCS-X in the past 6 years. $\varphi_{max}$ is the maximum atomic flux density (population of the 7 Zeeman sub-levels $m_F$), $S$ the detection surface, $T_{trans}$ the transverse temperature after the collimation and $\Phi_{det}$ the detected atomic flux. Note that the experimental fountain or FOCS1 where these techniques have been implemented are loaded by a Cs vapour whose pressure is of $\sim 10^{-8}$ mbar.

| | $\varphi_{max}$ (at·s$^{-1}$·m$^{-2}$) | S (m$^2$) | $T_{trans}$ ($\mu$K) | $\Phi_{det}$ (at·s$^{-1}$) |
|---|---|---|---|---|
| Sisyphus in FOCS1 | $2.8 \cdot 10^{10}$ | $0.5 \cdot 10^{-4}$ | 7 | $1.4 \cdot 10^{6}$ |
| Sisyphus in FOCS-X | $36 \cdot 10^{10}$ | $0.24 \cdot 10^{-4}$ | 3.6 | $8.6 \cdot 10^{6}$ |
| Sideband Zeeman in FOCS-X | $7 \cdot 10^{10}$ | $0.24 \cdot 10^{-4}$ | 1.6 | $1.7 \cdot 10^{6}$ |

**Table 2.2**: Comparison of the frequency stabilities at 1 s $\sigma_{1s}$ calculated from Eq. 1.1 for the detected atomic flux of Tab. 2.1.

| Cooling technique | $\Phi_{det}(m_F{=}0)$ (at·s$^{-1}$) | $\sigma$(1s) |
|---|---|---|
| Sisyphus in FOCS1 | $0.20 \cdot 10^{6}$ | $1.2 \cdot 10^{-13}$ |
| Sisyphus in EF | $1.23 \cdot 10^{6}$ | $4.5 \cdot 10^{-14}$ |
| Sideband Zeeman in EF | $0.23 \cdot 10^{6}$ | $1.0 \cdot 10^{-13}$ |

factor $Q$ of $10^{10}$ we obtain the stabilities reported in Tab. 2.2. Despite this calculation, a preliminary measurement of the frequency stability in FOCS1 differs from the expected value. As shown in Fig. 2.1, $\sigma$(1s) extrapolated from the experimental points is equal to $2.5 \cdot 10^{-13}$, a factor 2 higher than the calculated value. The reasons of this incongruence are not clear.

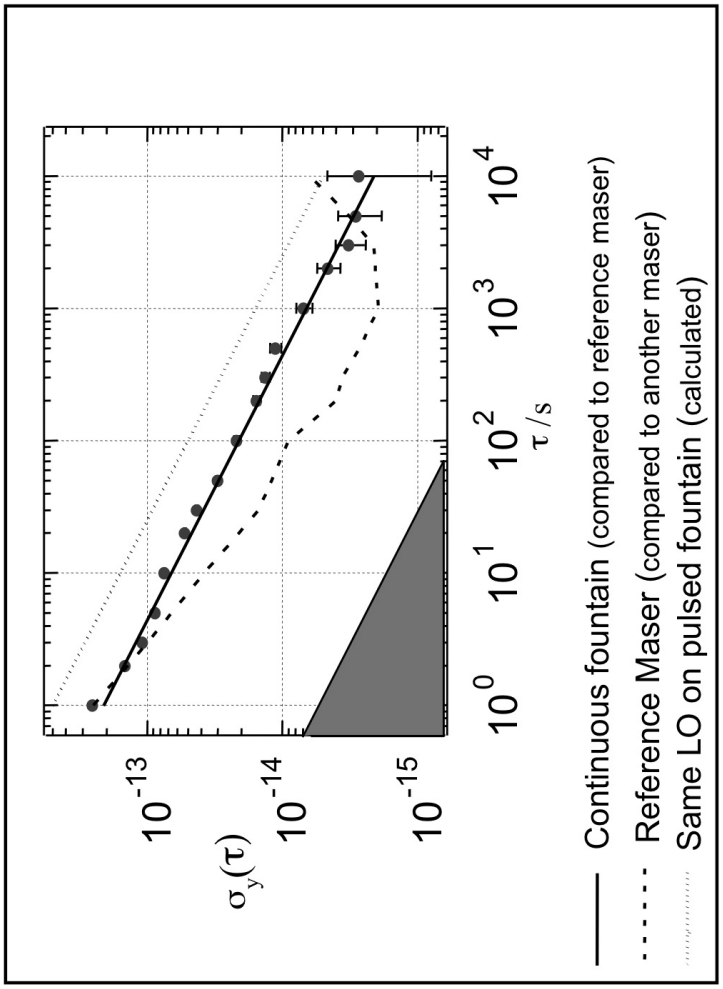


**Figure 2.1**: Result of a preliminary frequency stability measurement in FOCS1. The triangle in the corner of the graph represents the limit due to the instability of the local oscillator (intermodulation effect) in continuous operation. From the experimental points we extrapolate a frequency stability at 1 s equal to $2.5 \cdot 10^{-13}$. With the same local oscillator, pulsed operation would yield the calculated stability curve shown by the dotted line, degraded in this case by the intermodulation effect.

## 2.2 Total flux and detected flux

The detected atomic flux is a small fraction of the flux right above the source, due to the atomic beam transverse velocity and the corresponding beam divergence. To calculate this fraction we make the hypothesis that the transverse flux distribution is isotropic and decreases following a gaussian law. We can thus write:

$$\Phi_s(r) = \Phi_{tot} \cdot \frac{1}{\pi\ r_0^2} e^{-r^2/r_0^2} \tag{2.1}$$

Here $\Phi_s(r)$ is the initial flux, $\Phi_{tot}$ the total flux and $r_0$ the mean squared radius of the source, supposed to be smaller or of the same order than the radius $r_B$ of the two microwave feedthroughs (A and B in Fig. 2.2). This one is time-dependent:

$$r_0^2(t) = r_0^2(0) + v_{rms}^2 \cdot\ t^2 \tag{2.2}$$

where $v_{rms}$ is the mean squared atomic beam transverse velocity. The atoms pass once through the microwave cavity (label A in figure), reach the apogee of the parabolic flight and fall down. When they pass again through the microwave cavity (label B in figure), at the time $t_B$, the flux distribution will be:

$$\Phi_B(r) = \Phi_{tot} \cdot \frac{1}{\pi\ r_0^2(t_B)} e^{-r^2/r_0^2(t_B)} \tag{2.3}$$

where

$$r_0^2(t_B) = r_0^2(0) + v_{rms}^2 \cdot\ t_B^2 \tag{2.4}$$

and $v_{rms}$ is calculated by using the well known equation:

$$\frac{1}{2} M\ v_{rms}^2 = \frac{1}{2} k_B\ T \tag{2.5}$$

M being the atom mass, $k_B$ the Boltzmann constant and $T$ the transverse temperature. With the typical parameters reported in Tab. 2.3 we calculate $t_B$=0.64 s and $r_0(t_B)$ $\simeq$42 mm. This value is larger than $r_B$, thus the total atomic flux in B is limited by the size of the microwave cavity feedthrough and it can be write as:

$$\Phi_{tot}(r < r_B) \simeq\ \Phi_B(0) \cdot \pi\ r_B^2 = \frac{\Phi_{tot}}{\pi\ r_0^2(t_B)} \cdot \pi\ r_B^2 \simeq\ 0.01 \cdot \Phi_{tot} \tag{2.6}$$

Thus, for the considered parameters and for an atomic fountain without transverse collimation, the atomic flux detected at the end of the parabolic flight is only the 1% of the initial atomic flux.

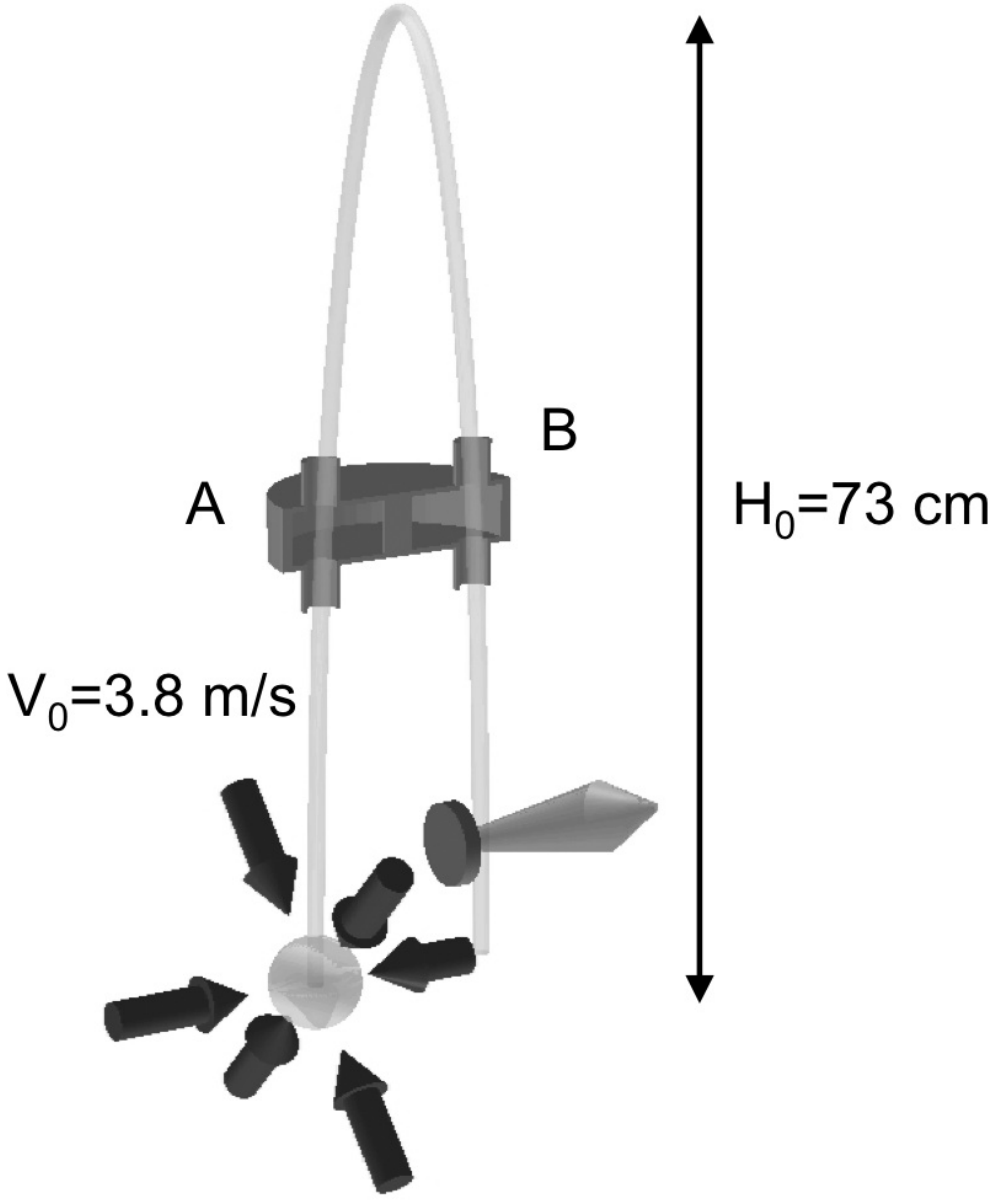


**Figure 2.2**: Flight path covered by the atomic beam. $v_0$ is the vertical launch velocity, $H_0$ the distance between the source and the apogee of the parabola and A and B the two interaction zones with the microwave.

**Table 2.3**: Typical parameters of the continuous fountain FOCS1.

| *Parameter* | *Notation* | *Value* |
|---|---|---|
| Initial beam radius | $r_0(0)$ | 3-6 mm |
| Effective feedthrough cavity radius | $r_B$ | 3 mm |
| Interaction time | $t_B - t_A$ | 0.5 s |
| Transverse temperature | T | 60 $\mu$K |
| Launch velocity | $v_0$ | 3.8 m$\cdot$ s$^{-1}$ |

## 2.3 Evaluation of the collisional shift

The collisions between the atoms during the interaction with the microwave give rise to a frequency shift of the hyperfine ground state levels known as collisional shift. For a laser-cooled cesium fountain frequency standard the perturbation due to the atom collisions yields a relative frequency shift given by (see Refs. [15, 16]):

$$\frac{\Delta\nu}{\nu_0} \simeq \ -0.8 \times 10^{-21} \cdot \overline{n} \tag{2.7}$$

where $\overline{n}$ is the mean atomic beam density in the continuous fountain above the microwave cavity, i.e. during the microwave interaction. A. Joyet has developed detailed numerical models to calculate the value of the mean atomic density in FOCS1 (see Ref. [8]). For a transverse and longitudinal temperature of respectively 5 $\mu$K and 100 $\mu$K (typical values for FOCS1) and taking into account the geometrical characteristics of the fountain, he has found $\overline{n}$=0.65 $n_0$, the latter being the estimated initial atomic density right above the source. From the same reference we know that

$$n_0 = \frac{\Phi_{meas}}{\pi \cdot \ r_0^2 \cdot \ v_0 \cdot (\frac{\Phi_{det}}{\Phi_0})_{calc}} \tag{2.8}$$

where $\Phi_{meas} \simeq \ 2{\times}10^5$ at$\cdot$s$^{-1}$ is the detected atomic flux measured in FOCS1, $r_0$=6 mm the mean quadratic radius of the atomic beam right above the source, $v_0$=3.8 m/s the launch velocity and $(\Phi_{det}/\Phi_0)_{calc}$=3.4% the calculated ratio between the detected and the initial atomic flux. By inserting these values in Eq. 2.8 we find $n_0 \simeq \ 1.3{\times}10^4$ at$\cdot$cm$^{-3}$ and thus a collisional shift of -0.67$\times10^{-17}$.
The obtained result confirms that the performance of the continuous fountain is not limited by the collisional shift; in particular, we can increase still further the atomic flux to improve the frequency stability (depending from $\Phi_{det}$) without loosing in frequency accuracy. For the second continuous fountain FOCS2, currently under construction, an atomic flux increased by a factor

$\simeq$40 with respect to FOCS1 is foreseen. We have already obtained this gain in the experimental fountain: a factor 2 comes from the realisation of the Sisyphus cooling in a phase stable optical lattice (see Ref. [10] and Tab. 2.1) and the remaining factor 20 comes from the introduction of a magneto-optical trap to load the source (see Chap. 6). The collisional shift that we would measure in FOCS2 for such an atomic flux is about -2.7$\times 10^{-16}$; the uncertainty on this value is compatible with the indicated budget of $4\times 10^{-16}$. On the other hand the frequency stability would be improved by a factor $\sqrt{40}$ with respect to FOCS1.

# Chapter 3

# Experimental set-up

In this chapter we present the experimental apparatus and the configuration of the optical table used for the transverse collimation measurements exposed in Chapters 4 and 5. We illustrate also the method used to detect the atomic flux. In Chap. 6 the set-up is changed and the optical table modified, so we will present there the new experimental set-up. We have reduced the description of the set-up to the bare essentials, the apparatus having already been described in detail in Ref. [10].

## 3.1 Vacuum system

The vacuum system is shown in Figs. 3.1 and 3.2. The pressure inside the experimental set-up is of the order of $10^{-9}$ mbar and kept constant by an ion pump Varian Star Cell whose pumping rate is 230 l/s. Its pumping elements were changed in December 2004 when we opened the experimental fountain to mount the pre-source. In the following we describe briefly the functionality of each of the four modules in Fig. 3.1 that compose the fountain. All modules are made from aluminium Avional AA 2007, a material useful because it is non magnetic, easy to work and with a negligible outgassing rate. Vacuum seals are made from mashed indium wire (diameter between 1 and 2 mm), which is compatible with aluminium and saves space compared with other metal gaskets.

- Source module (1): this module is used to capture the thermal cesium vapour that feeds the fountain in a 3D-optical molasses. The latter is formed by 3 pairs of counter-propagating laser beams exiting from the 5 collimators clearly visible in Fig. 3.1. Cesium is injected into this reservoir from a copper finger located in the lower part. By heating this tube, one can regulate the cesium pressure at around $10^{-8}$ mbar. This pressure is ascertained by absorption measurements of a probe

beam passing through the centre of the chamber. The internal walls of the module are painted with the Aquadag (graphite) for two reasons: graphite is a good getter for the cesium and an efficient remedy against stray light emanating from the source laser beams. More details about this module can be found in Ref. [8], the source configuration being the same as that of FOCS-1.

- Collimation module (2): here we perform the transverse collimation of the continuous atomic beam. Two sets of four windows (disposed along the $x$ and $y$ axes) separated vertically by 60 mm allow the realisation of a two-step collimation using a different cooling mechanism in each of the two regions. Otherwise, one can plan to use the first region for the collimation and the upper one for the diagnostic. Currently, we use only the upper plane in a geometry that depends on the cooling mechanism and is illustrated in the dedicated chapters.

- Detection module (3): the module has a rectangular shape. It is separated vertically by a graphite layer (see Fig. 3.2) to avoid any contamination in the detection region of the atoms and the laser light coming from the up-going atomic beam. In each part it is possible to perform the detection of the atomic beam (see accesses A and B in Fig. 3.2), by fluorescence and/or by absorption signal. The advantage of the access A is a higher signal than the one in B, but the transverse temperature measurement is better in B (higher resolution). Note that for the cooling mechanisms studied in this work we have used only the access B for a detection by fluorescence technique (well described at the end of this chapter), while to characterise the pre-source we shifted the detection vertically above the source (access A), and we have recorded simultaneously both the absorption and the fluorescence signals (see Chap. 6).

- Ballistic module (4): in this module the atomic beam performs the parabolic flight from the collimation plane until the detection region. There are no windows so as to protect the atoms from external optical perturbations. The greater the time of flight in this region, the more sensitive the measurements of transverse temperature.

## 3.2 Optical table

A scheme of the optical table is given in Fig. 6.3. All laser beams are transmitted from the table to the experimental apparatus through polarisation-maintaining optical fibres. Collimators at the fibre exit allow adjustement of beam diameters. The laser frequency is monitored or servo-controlled via

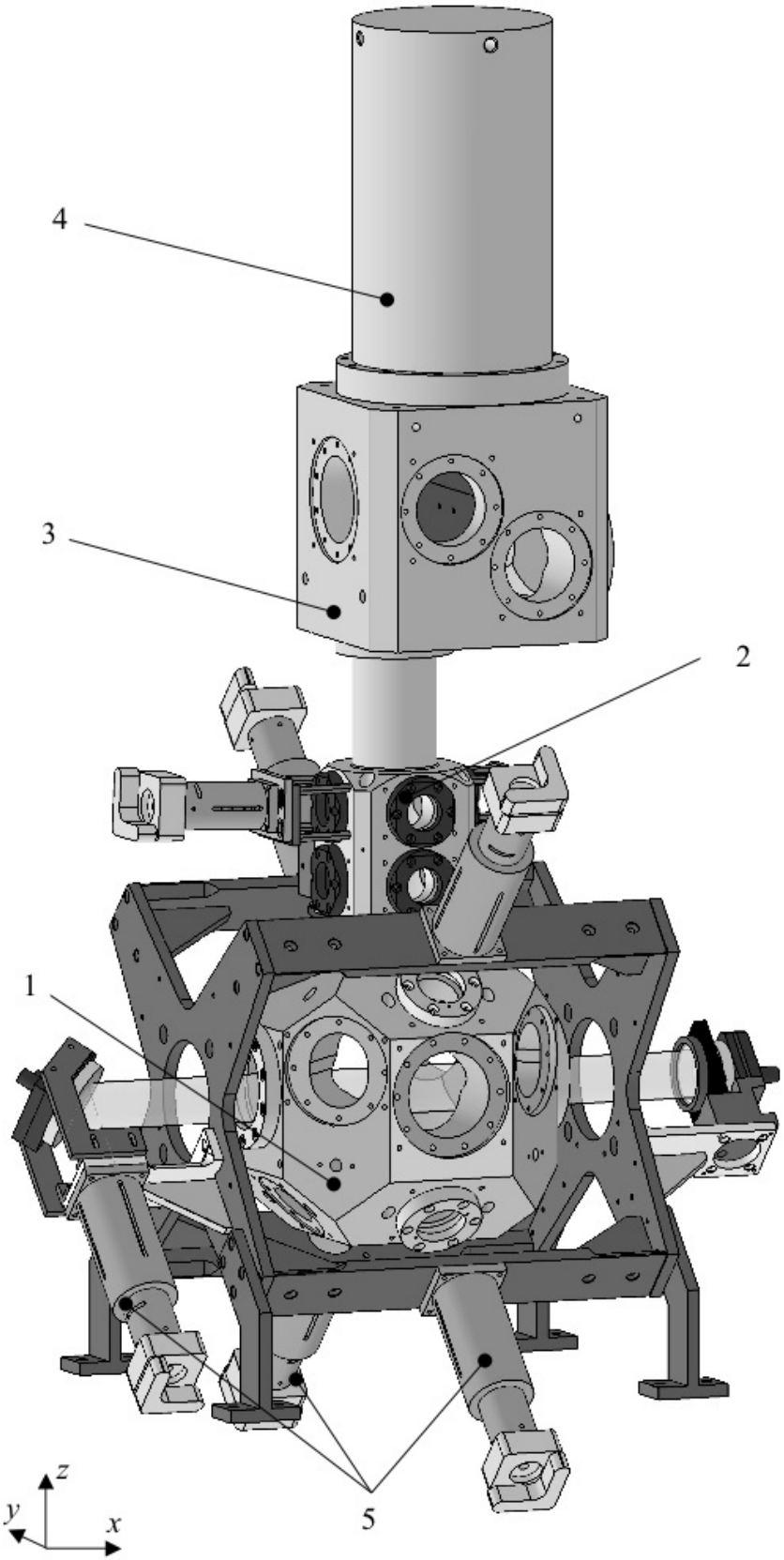


**Figure 3.1**: Experimental apparatus divided into 4 modules. 1 : source; 2 : transverse collimation; 3 : detection; 4 : ballistic flight. 5 : Collimators used to expand the laser beams. See text for more details.

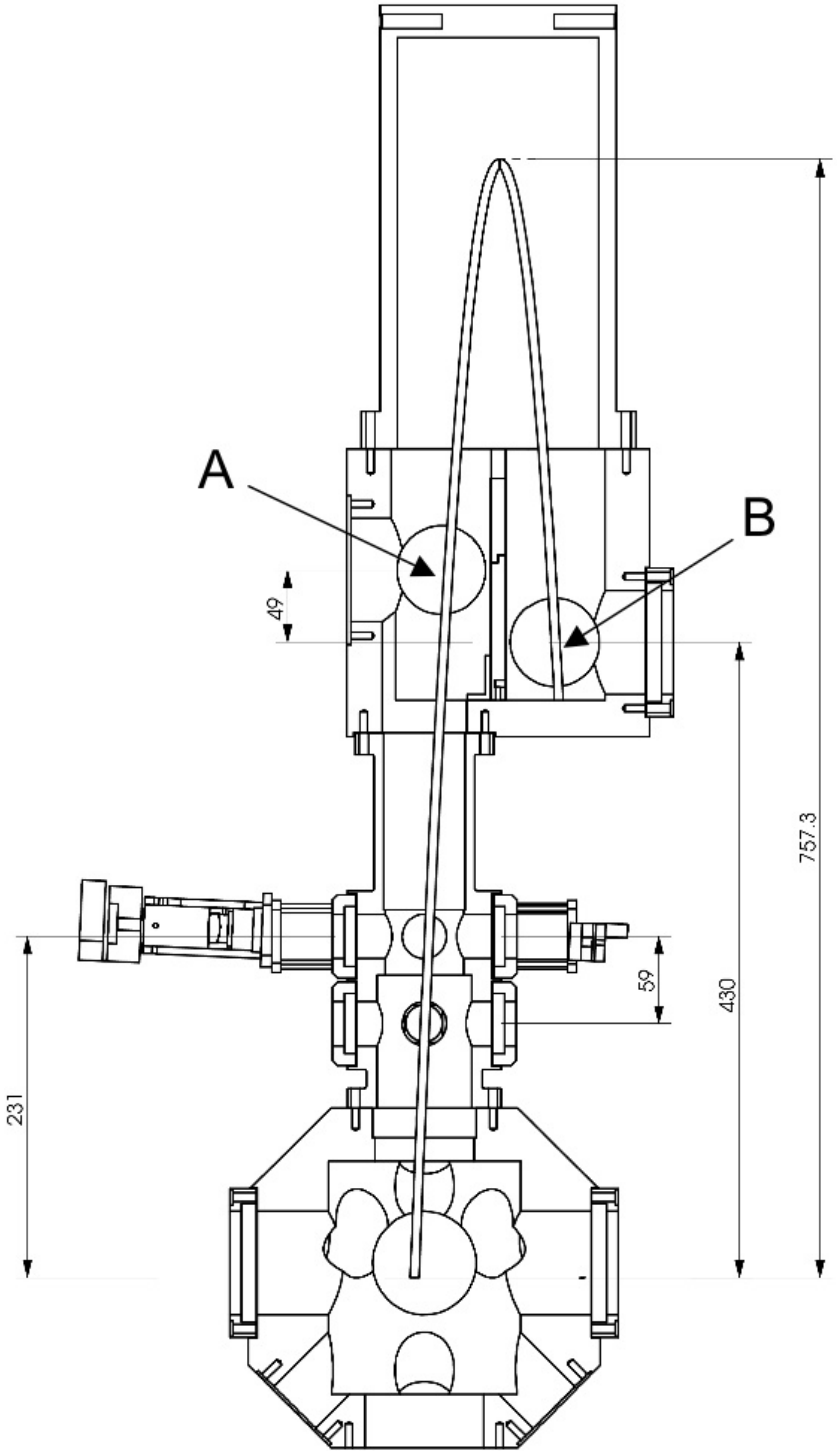


**Figure 3.2**: Experimental apparatus in a two-dimension view. The parabola represents the flight path of the atomic beam. A and B are the two accesses for the detection. The dimensions are in millimetres.

the saturated absorption signal inside a dedicated cesium cell ((17) in Fig. 6.3). In the following we present the lasers used for the source, the transverse collimation and the atomic beam detection.

### 3.2.1 Lasers for the source of the continuous atomic beam

The thermal cesium vapour that feeds our fountain is captured by a 3D-optical molasses in the module (1) of Fig. 3.1. The 3D-optical molasses is formed by six counterpropagating beams, red detuned by 12 MHz from the $F = 4 \rightarrow F' = 5$ transition[1] and circularly polarised (each pair of counterpropagating beams has opposite $\sigma^+ - \sigma^-$ polarisation). The horizontal retro-reflected beam ($x$-axis) is overlapped with a weak repumper beam (power 0.1 mW) locked to $F = 3 \rightarrow F' = 4$ transition and provided by a Distributed Bragg Reflector (DBR) laser ((3) in Fig. 6.3). It recovers into $F = 4$ the atoms pumped into $F = 3$. The central frequency of the upward and downward pairs of the 3D-optical molasses beams can be modified independently using different Acoustic-Optical Modulators (AOMs) to produce either a static or a continuous moving optical molasses [17]. The beams originate from a common laser ((1) in the scheme of the optical table, Fig. 6.3), an Extended Cavity Diode Laser (ECDL) offset-locked by 160 MHz above the $F = 4 \rightarrow F' = 4$ transition and amplified by injection into a Master Oscillator Power Amplifier (MOPA) used as an optical amplifier. The output of the MOPA (∼350 mW of power) is split in three components that pass through three AOM's centred near 80 MHz to produce the desired cooling frequencies. The power per beam is 7 mW and the waist radius 13 mm.

### 3.2.2 Lasers for the collimation of the continuous atomic beam

The lasers for the transverse collimation of the atomic beam lie in a plane 22 cm above the source (see Fig. 3.2) and tilted by 3 ° with respect to the horizontal. We need essentially two lasers, the cooling laser and the pumper laser. The former ((4) in Fig. 6.3) is a Fabry-Perot mounted in an extended cavity and amplified after passage into a MOPA. The cooling laser is either scanned across the Cs D2 line or locked to a specific frequency depending on the experimental requirements. A frequency beat[2] between this laser and the repumper laser already introduced in the previous subsection allows us to lock the cooling laser off resonance. Its typical power is between 3 and

[1] See Appendix A for a scheme of the energy levels of the $^{133}$Cs atom.

[2] The device that allows this frequency control was provided by Michel Lours of the BNM-SYRTE, Observatoire de Paris.

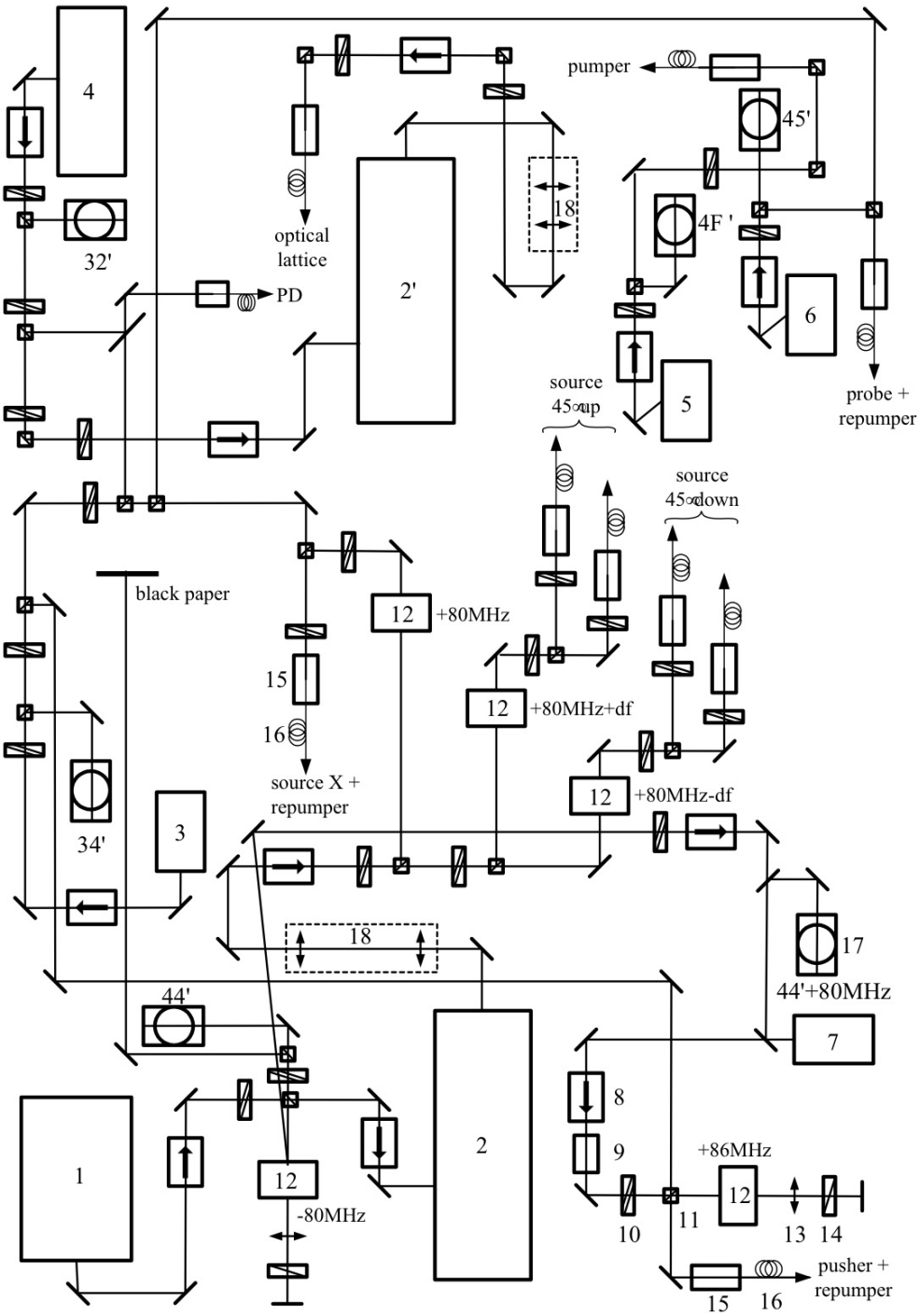


**Figure 3.3**: Layout of the optical table scheme. 1: master laser (ECDL); 2: optical amplifier (MOPA); 3: repumper laser (DBR); 4: cooling laser (ECDL); 5: pumper laser (ECDL); 6: probe laser (ECDL); 7: pusher laser (injected laser diode); 8: optical isolator; 9: astigmatic compensation prisms; 10: half-wave plates; 11: polarising beam splitter; 12: acoustic-optic modulator; 13: achromatic lenses; 14: quarter-wave plates; 15: optical fibres coupling; 16: polarisation maintaining optical fibres; 17: saturated absorption Cs cells; 18: telescope; PD: fast photo-detector for beat frequency measurements.

10 mW; the radius waist is 5.7 mm but the laser beam is truncated with a diaphragm at $r$=9 mm. The polarisation is always linear but we can change the polarisation gradient by rotating a half-wave plate situated at the exit of this fibre. The latter laser used for the collimation is a pumper laser (5) used to pump back into the initial ground state the atoms lost due to optical pumping toward the other ground state. For this role we have considered both the D1 and the D2 lasers, simply replacing on the optical table the first one with the other. It is in any case an ECDL (the diode is a Fabry-Perot) locked on the opportune atomic resonances. This laser has the same characteristics as the cooling laser but a typical power between 0.06 and 0.6 mW. Its polarisation does not play a role in the transverse collimation mechanism.

### 3.2.3 Lasers for the detection of the continuous atomic beam

When the atoms leave the collimation region, they perform a parabolic flight as shown in Fig. 3.2 and reach the detection region. The detection is realised by fluorescence induced by a probe laser (6). The laser is a Fabry-Perot diode mounted in an extended cavity and locked to $F = 4 \rightarrow F' = 5$ transition detected on a saturated absorption cell. This frequency can be shifted by a Zeeman coil around the cesium cell. The laser beam is retro-reflected by a mirror and the polarisation is circular. The radius waist is 2.8 mm but we truncate the radius at $r$=1 mm to obtain a laser beam homogeneous in intensity; its power is 1 mW, near the optical saturation. To detect all the atoms, both those in $F = 4$ and those in $F = 3$, the repumper laser (3), 0.3 mW of power, is overlapped with the probe laser; these two laser beams are injected into the same optical fibre. The last laser present on the optical table is the pusher laser (7). This is a Fabry-Perot diode injected from the component of the laser (1) that has been shifted by the AOM by 80 MHz above the $F = 4 \rightarrow F' = 4$ hyperfine transition frequency. It passes twice through an AOM and is further shifted by 86 MHz each time, so as to be at the $F = 4 \rightarrow F' = 5$ resonance frequency. The laser beam has a gaussian shape, with $\sigma$=12 mm (from which we calculate a waist radius of 24 mm) and is truncated to a diameter of 34 mm; the typical power is 0.8 mW and the beam intensity is homogenous. The role of this laser is to push away the wings of the atomic beam just before the collimation plane in order to know the exact transverse dimension of the atomic beam, an important parameter for the transverse temperature measurements (see Sec. 3.4). To get this we have inserted at the exit of the collimator a mask of the type shown in Fig. 3.4. The 90% of the atoms that pass outside the region -5 mm$< x <$+5 mm for -4 mm$< z <$+4 mm are pushed away. As the probe laser, also the pusher laser is overlapped with a weak component (power 0.04 mW) of the repumper

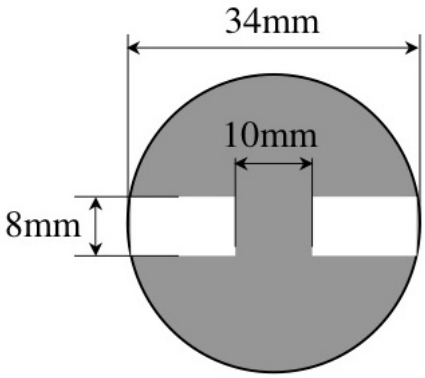


**Figure 3.4**: Mask inserted at the exit of the collimator of the pusher laser to push away the wings of the atomic beam before the collimation plane. The atomic beam transverse size is thus fixed at 10 mm.

laser (3).

## 3.3 Detection techniques of the atomic beam

The atomic beam detection is realised by fluorescence signal. A probe laser retro-reflected along the $y$-axis excites the atoms that pass through the detection region. The fluorescent light is collected by a photodetector Hamamatsu H1336-8BK and amplified using an electric circuit whose main components are an operational amplifier OP15 FJ, a feedback resistance of 500 MΩ and a feedback capacity of 1 pF. The photodetector is circular with a diameter of 6 mm; to focus onto it the fluorescence light emitted by the atoms excited by the probe laser, whose diameter is diaphragmed to 2 mm, we use a system of two Fresnel lenses $L_1$ and $L_2$ glued together, of identical diameter 100 mm and focal lengths $f_1$=254 mm and $f_2$=127 mm respectively. Since the ratio between the two focal lengths is equal to 2, we can map on the photodetector a region of the atomic beam twice larger (see Fig. 3.5). All the detection system (probe beam, detection optics and photodetector) can be translated together along the $x$-axis, allowing the measurement of the atomic beam profile.

The probe laser frequency is modulated on and off resonance by using Zeeman effect into a saturated absorption cell. The modulation amplitude is 20 MHz, value big enough to pass from the resonance condition to a negligible

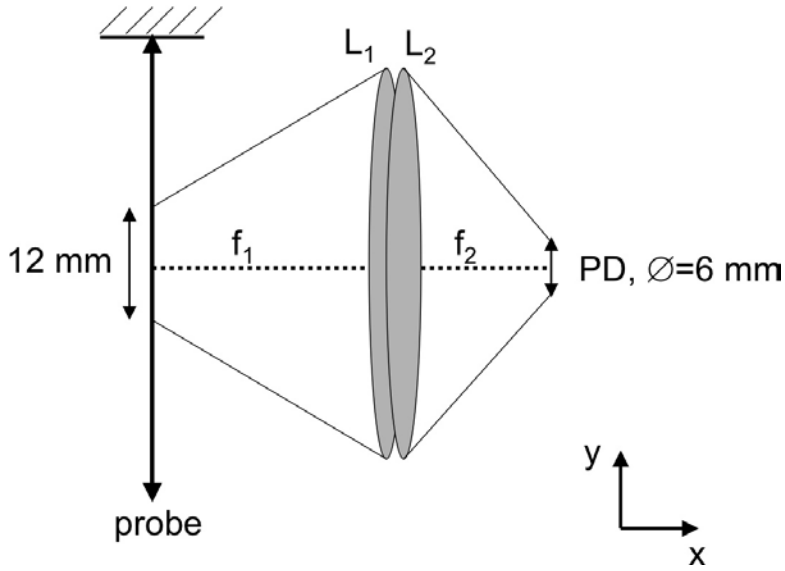


**Figure 3.5**: Scheme of the detection system. The photodetector (PD) collects the fluorescent light emitted by the atoms excited by the probe beam and focused with the use of two Fresnel lenses $L_1$ and $L_2$ (diameter 100 mm) whose focal lengths are $f_1$=254 mm and $f_2$=127 mm. The detection system can be moved along the $x$-axis.

fluorescence signal. The modulation frequency is 87 Hz, value below the cut-off of the photodetector ($\nu_c \sim 300$ Hz) and lower than the cut-off of the laser frequency control system ($\nu_{c_{laser}}$=1 kHz). The output signal of the photodetector passes through a lock-in amplifier for the de-modulation.

The spatial resolution of the fluorescence signal is limited by the cut-off frequency $\nu_{out}$ of the filter at the output of the lock-in amplifier. This resolution is given by $\delta x_{min} \sim L/(\nu_{out} \cdot \Delta t_{scan})$, where $\Delta t_{scan}$ is the duration of a position scan and $L$=50 mm is the length of the position scan. We have chosen $\nu_{out}$=3.3 Hz and we wish a resolution of about 1 mm. This implies $\Delta t_{scan}$ >20 s.

## 3.4 Transverse temperature measurement

We measure transverse temperatures by translating the whole detection system (probe and repumper lasers and detection optics) in the horizontal plane and measuring flux as a function of position. In this way the fluorescent light focalisation onto the photodetector and the stray light do not change. The data are fitted to a gaussian curve (collimated atoms) superimposed on a slope representing the wings of a much broader distribution of non-collimated atoms, whose transverse temperature is in the order of 60 $\mu$K (see Ref. [5]). The obtained profile is due to the expansion of the atomic beam between the collimation plane and the detection and its width, taking into account all the

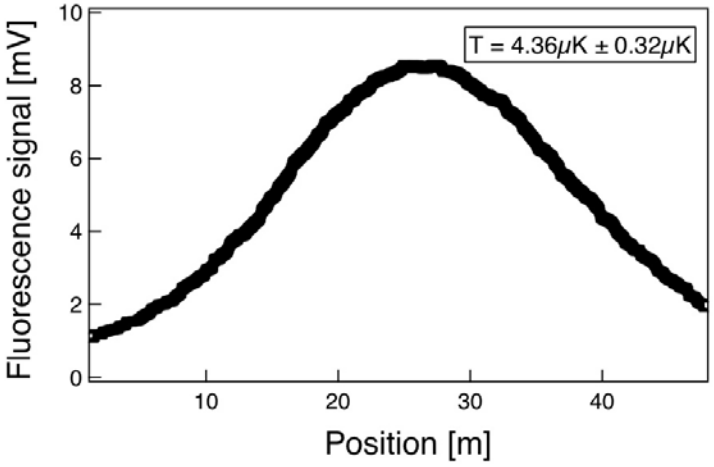


**Figure 3.6**: Example of measurement of the atomic beam profile after collimation using gray molasses technique. The gaussian profile is combined with a slope due to the not-collimated atoms. The theoretical fit matches very well the experimental points and is hardly visible in the graph. The error on the fluorescence signal is explained in the text.

sources of broadening, is proportional to the transverse temperature:

$$T_{transv} = \frac{M}{k_B} \cdot (\frac{\sigma(v_{cx})}{cos\theta})^2. \tag{3.1}$$

Here $M$ is the mass of the cesium atom, $k_B$ the Boltzman constant, $\theta$ the angle of the collimation plane with respect to the vertical and $\sigma(v_{cx})$ the standard deviation of the transverse velocity right after the collimation process. The latter is not directly accessible and it is calculated as shown in the next paragraph. An example of an atomic beam profile measurement with extrapolation of the transverse temperature is given in Fig. 3.6.

### 3.4.1 Sources of broadening

The size $\sigma(x_p)$ of the atomic beam is fixed by using the mask and the pusher laser beam already introduced in Chap. 3. The pusher laser is situated 59 mm below the collimation plane. It crosses transversally the atomic beam and pushes away the atoms lying in $|x| > 5$mm acting along a height of 8 mm. Thus the sources of broadening of the detected atomic beam profile are:

♢ The expansion between the pusher beam and the collimation plane. Given the transit time between these two regions ($t_{pc}$=19 ms) and a temperature of 60 $\mu$K we calculate an atomic beam expansion of $\sigma_{\Delta x_{pc}}$=1.16 mm.

♢ The probe laser beam dimension. The diameter of the probe beam is equal to 2 mm; this implies a standard deviation $\sigma(x_d)$=0.58 mm.

♢ The longitudinal temperature distribution. The ballistic flight being parabolic, the longitudinal temperature spread has a weight on the broadening of the detected atomic beam profile. This contribution is given by

$$\sigma(x_d)_{T_{long}} = \sqrt{\frac{k_B T_{long}}{M}} \cdot \ sin\theta \cdot \Delta t_{cd} \cdot [1 + \frac{v_{cz}}{\sqrt{v_{cz}^2 - 2g\Delta H_{cd}}}] \quad (3.2)$$

where $\theta$=3 °, $\Delta t_{cd}$=0.57 s is the time of flight between the collimation and the detection, $v_{cz}$=3.1 m/s is the vertical component of the velocity at the collimation plane and $\Delta H_{cd}$=199 mm is the vertical distance between the collimation and the detection. For a typical value of $T_{long}$=100 $\mu$K the broadening due to the longitudinal temperature is equal to 4.7 mm.

Finally, from the measured width $\sigma(x_d)_{meas}$ of the atomic beam profile we can calculate the transverse temperature right after the collimation using Eq. 3.1 where

$$\sigma(v_{cx}) = \frac{1}{\Delta t_{cd}} \cdot \sqrt{\sigma(x_d)_{meas}^2 - \sigma(x_d)^2 - \sigma(x_p)^2 - \sigma(x_{pc})^2 - \sigma(x_d)_{T_{long}}^2} \quad (3.3)$$

### 3.4.2 Sources of error

Before fitting the measured atomic beam profile with a theoretical curve it is necessary to evaluate the sources of uncertainty on the detected fluorescence signal $U_{fluo}(t)$ and on the probe position $x_d(t)$. We have essentially two different contributions to the total error:

- Uncertainty coming from shot noise on the fluorescence signal. Assuming an atomic flux in the order of $10^6$ atoms per volt, the fluctuation of the signal is given by $\Delta U_{sn}$=$10^{-6}\sqrt{N_{atoms}}$, where $N_{atoms}$=$10^6$U. Typical value of 5· $10^{-5}$V.

- We estimate a random error in the position of the probe laser beam of $\Delta$x=0.17 mm. To insert this error into the total uncertainty we use the differential expression $\Delta U_x$=$(\frac{dU}{dx})\Delta x$. Typical value of $10^{-5}$V.

The total uncertainty is obtained by gaussian propagation of these two errors and it is calculated for each measurement of $U_{fluo}(t)$.

## 3.5 Flux calibration

The calibration of the atomic flux is realised by the well known method of signal-to-noise ratio. This technique is independent from the characteristics of the optical system and thus particularly favourable. Even if a detailed description can be found in Ref. [10], we will give in the following (Sec. 3.5.2) a short memorandum of this method.

### 3.5.1 Fluorescence signal

The fluorescence signal $U_{fluo}$ detected by the photodetector at the end of the parabolic flight is proportional to the instantaneous atomic density in the detection volume $V_{det}$. On the other hand, we can calculate the flux density from the atomic density by multiplying the latter by the mean velocity $v_d$ of the atoms in the detection region:

$$U_{fluo}(t) = k_N \; n(t) \tag{3.4}$$

$$\varphi(t) = n(t) \cdot \; v_d \tag{3.5}$$

The atomic density being given by $n(t) = N_{at}(t)/V_{det}$, where $N_{at}(t)$ is the number of the atoms that transit in the detection region at the time $t$, we can write the fluorescence signal as:

$$U_{fluo}(t) = \eta_{PD} \cdot \hbar\omega \cdot \gamma_p \cdot \frac{\Omega_{det}}{4\pi} \cdot \eta_{opt} \cdot \; N_{at}(t) \tag{3.6}$$

where we have taken into account all the optics and detection parameters:

- $\eta_{PD}$ is the photodetector efficiency:

$$\eta_{PD} = S_{PD} \cdot \; R_f \tag{3.7}$$

  where $S_{PD}$=0.5 A/W is the photodetector responsivity and $R_f$=500 $M\Omega$ is the feedback resistance;

- $\hbar\omega$ is the fluorescence photons energy:

$$\hbar\omega = 1.05 \cdot \; 10^{-34} \cdot \; 2\pi \cdot \frac{c}{\lambda} \tag{3.8}$$

  where $c$=3·10$^8$ m/s is the light velocity and $\lambda$=852 nm is the cesium wavelength (D2 line);

- $\gamma_p$ is the scattering rate:

$$\gamma_p = \frac{\Gamma \cdot \; s_0/2}{1 + s_0 + (2\delta/\Gamma)^2} = 1.3 \cdot \; 10^7 \text{ s}^{-1} \tag{3.9}$$

where $\Gamma$ is the natural width, $s_0 = I/I_0$ the saturation parameter and $\delta$ the frequency detuning from the atomic resonance; $I = P_{tot}/2\pi\sigma^2$ is the maximum intensity at the centre of the probe laser and $I_0$=1.1 mW/cm$^2$ is the saturation intensity (the probe laser is $\sigma^+$ polarised);

- $\frac{\Omega_{det}}{4\pi}$ is the ratio between the detection solid angle and $4\pi$:

$$\Omega_{det} = \frac{\pi\ r_1^2}{f_1^2} \tag{3.10}$$

where $r_1$=50 mm and $f_1$=254 mm are the characteristics of the Fresnel lens indicated as $L_1$ in the previous chapter, Fig. 3.5. We find $\frac{\Omega_{det}}{4\pi}$=1%;

- $\eta_{opt}$ is the total optics efficiency:

$$\eta_{opt} = 0.98 \times\ 0.7 \times\ 0.7 \times\ 0.7 \tag{3.11}$$

where the first term is the transmission of the window while the others are the transmission of the two Fresnel lenses and the photodetector window;

- $N_{at}(t)$ as already said represent the number of atoms that pass through the detection region at the time $t$.

The probe laser beam has a diameter of 2 mm and a length of 12 mm, thus $V_{det}$=38 mm$^3$ and the mean velocity of the atoms in the detection region $v_d$ is 2.5 m/s. Replacing all the numerical values we find:

$$U_{fluo}(t) = k_N\ n(t) = k_\varphi \cdot \varphi(t) \tag{3.12}$$

$$\text{with } k_N = 7.7 \cdot\ 10^{-14}\ V \cdot\ m^3 \cdot\ at^{-1}$$

$$\text{and } k_\varphi = 3.1\ 10^{-14}\ V \cdot\ m^2 \cdot\ s \cdot\ at^{-1}$$

This method allows one to calculate the atomic flux density from the measured fluorescence signal, but it depends strongly on the detection parameters which are not always well known. For this reason, it is important to measure the constant $k_\varphi$ by another technique, namely the signal-to-noise ratio.

### 3.5.2 Signal-to-Noise ratio

We measure the d.c. fluorescence signal $S_{at}$ with a voltmetre and the total noise $B_{tot}$ with a spectrum analyser that gives us the power spectral density (PSD), measured in a frequency window such that $\nu < \nu_c$, where $\nu_c$ is the cut-off frequency already introduced and limits the region where the photodetector noise is white. In this region also $B_{tot}$ has to be white, condition necessary (but not sufficient) to make the hypothesis that the shot noise

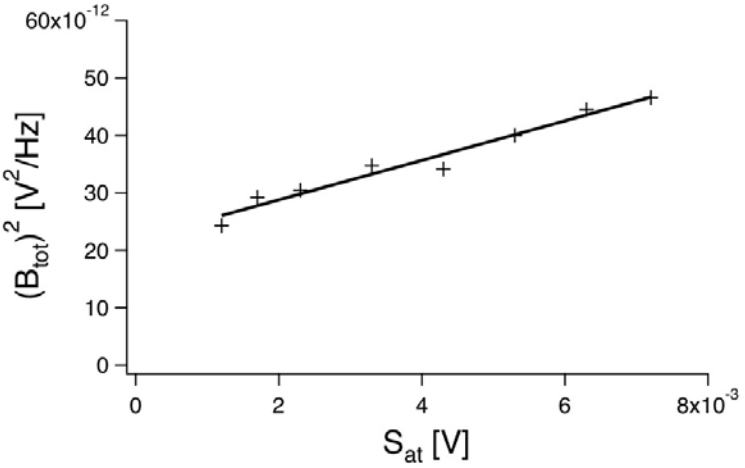


**Figure 3.7**: Measurement of $S_{at}$ as a function of $B_{tot}^2$ for different values of the atomic flux. The data points are well fitted by a straight line. From the linear fit we obtain the values of $B_0$ and $k_\varphi$: $B_0 = 4.6 \cdot\ 10^{-6}$ V/$\sqrt{Hz}$ and $k_\varphi$=4.1$\cdot\ 10^{-14}$ V$\cdot$ m$^2\cdot$ s$\cdot$ at$^{-1}$. This calibration has been made using Sisyphus transverse cooling.

dominates over the other sources of noise. We need to know the atomic noise $B_{at}$, but we assume that:

$$B_{tot} = \sqrt{B_{at}^2 + B_0^2} \tag{3.13}$$

where $B_0$ represents all the other sources of noise and we do the hypothesis that they do not depend from the atomic flux. The relation between the signal-to-noise ratio and the flux density, as exposed in Ref. [5], is given by:

$$(\frac{S_{at}}{B_{at}})^2 \equiv \frac{\overline{U_{fluo}(t)}^2}{PSD(\nu < \nu_c)} = \frac{1}{2}\overline{\varphi(t)}S_{det} \tag{3.14}$$

where $S_{det}$=24 mm$^2$ is the detection area. Replacing Eqs. 3.12 and 3.13 into the equation above we find finally:

$$B_{tot}^2 - B_0^2 = \frac{2\ k_\varphi}{S_{det}} \cdot\ S_{at} \tag{3.15}$$

We have then measured $S_{at}$ and $B_{tot}$ for different values of the atomic flux and we have performed a linear fit. The result of the most recent calibration is shown in Fig. 6.10. We can remark that the experimental data are well interpolated by a straight line, confirming the hypothesis made on $B_0$, namely that the dominating contribution to the noise PSD is atomic shot noise.

From the linear fit we find the value of $k_\varphi$:

$$k_\varphi = 4.1 \cdot\ 10^{-14}\ V \cdot\ m^2 \cdot\ s \cdot\ at^{-1} \tag{3.16}$$

This value confirms the result of the previous calibration (see Ref. [10]) and is in good agreement also with the value calculated by the fluorescence method (see Eq. 3.12). In all our experimental results we have used this value of $k_\varphi$ to calibrate the atomic flux, this technique being independent from the detection parameters as already mentioned at the beginning of this section.

### 3.5.3 Flux density, maximum flux density and total flux

For clarity we define here the flux density, the maximum flux density and the total flux. What we measure moving horizontally the detection system is the flux density $\varphi(x, y)$; this curve is well fitted by a gaussian:

$$\varphi(x,y) = \frac{\Phi_{tot}}{2\pi\sigma_x\sigma_y} \cdot \exp(-\frac{(x-x_0)^2}{2\sigma_x^2}) \cdot \exp(-\frac{(y-y_0)^2}{2\sigma_y^2}) \tag{3.17}$$

where $\Phi_{tot}$ is the total flux and $\sigma_{x(y)}$ the standard deviation along $x(y)$. We assume that $\sigma_x$=$\sigma_y$ (we can not measure $\sigma_y$), hypothesis based on the fact that the transverse cooling process acts isotropically. The flux density would be also a function of $z$ but we can neglect this variable the detection system being always at the same level.

The maximum flux density $\varphi(x_0, y_0)$ is the flux density measured in the atomic beam centre. The graphs presented in this work show this quantity.

The total flux is easily calculated by the maximum flux density using the equation:

$$\Phi_{tot} = 2\pi\sigma_x\sigma_y \cdot \varphi(x_0, y_0). \tag{3.18}$$

# Chapter 4

# 2D laser collimation induced by a polarisation gradient

In this chapter we present studies of two-dimensional transverse laser collimation of a continuous cold cesium fountain using a 2D-optical lattice with a polarisation gradient. We focus our attention particularly on the $F = 3 \Rightarrow F' = 2$ transition, for which we observe a collimation effect when the cooling laser is locked on the blue side of the atomic resonance, while we do not analyse the already well known Sisyphus cooling on the red side of the $F = 4 \Rightarrow F' = 5$ transition. We study the effect of a static magnetic field applied in the plane of the optical lattice and compare the results with the similar work performed in other laboratories. Part of the work presented here is also discussed in Ref. [18].

## 4.1 Introduction

Laser cooling of atoms in magneto-optical traps and in optical molasses relies on Sisyphus cooling working on a cycling transition of the type $F \Rightarrow F' = F + 1$. For these transitions the cooling laser is tuned on the red side of the atomic resonance ($\delta = \omega_L - \omega_{at} < 0$) and the equilibrium between the cooling effect due to the fluorescence rate (absorption process followed by spontaneous emission of a photon of higher energy) and the heating effect due to the same fluorescence rate generated by the photon recoil, gives the final temperature. This kind of molasses is called *bright molasses* for the high coupling between atoms and light field. Since the years '90 in various atomic physics group, especially in France by the team of Grynberg ([19, 20, 21, 22, 23]), atom cooling using the transitions $F \Rightarrow F' = F$ and $F \Rightarrow F' = F - 1$ has been studied. In these cases there is at least one ground state that is not coupled to the light field and atoms are accumulated into these, resulting in a reduced emitted fluorescence, hence the name of *gray molasses*. The low photon scattering rate reduces the interaction between atoms and thus a cold

atomic sample of higher density and possibly lower temperature than the one produced by *e.g.* a magneto-optical trap or by bright molasses is expected.

Here we have studied atom cooling in a two-dimensional optical molasses whose polarisation gradient is in a configuration lin⊥lin. The cooling laser frequency was scanned over all the cesium D2 line and we have observed both red and blue detuned Sisyphus cooling. We present a detailed study of the blue Sisyphus cooling using the $F = 3 \Rightarrow F' = 2$ transition (gray molasses), analysing the variation of the final temperature and detected flux density as a function of various parameters (cooling laser detuning, intensity and beam diameter, pumper laser power and frequency, applied transverse static magnetic field). We have measured the minimum temperature of 3.5 $\mu$K when the cooling laser power was equal to 3.5 mW and for a detuning of 3$\Gamma$ (where $\Gamma$=2$\pi\cdot$5.22 MHz is the natural width of the Cs D2 line); corresponding to this temperature we have detected, at the end of the parabolic flight, a flux density of $\sim 2.7\times10^{11}\mathrm{at\cdot s^{-1}\cdot m^{-2}}$.

## 4.2 Physics of the cooling mechanism in gray molasses

The cooling mechanism in gray molasses is illustrated in Fig. 4.1 for a one-dimensional model. It relies on a Sisyphus effect between states $|C\rangle$ coupled to the light field whose light shift is spatially modulated and states $|NC\rangle$ not coupled for which the corresponding optical potentials are independent of position and flat. The frequency of the cooling laser being in the blue side of the atomic resonance (for a configuration $F \Rightarrow F' = F$ or $F \Rightarrow F' = F-1$), the optical potentials of the coupled states are above the flat potential of the non-coupled states. The transition rate between non-coupled and coupled states and viceversa is position dependent. The former is maximum when the light intensity is minimum, *i.e.* when the light shift of the coupled state is minimum (A in Fig. 4.1). The latter is proportional to the light intensity, as a regular optical pumping rate, thus the atoms are pumped back into the non-coupled state with higher probability when they are in the region of maximum light shift (B in Fig. 4.1), at the top of the potential hill. In this way for each cycle the atoms lose the kinetic energy equivalent to the potential energy gained by the atom after it has climbed the potential hill.

For the transition $F = 3 \Rightarrow F' = 2$ in which we are interested the non-coupled states are, for example in a point where the polarisation is $\pi$, the Zeeman sub-levels $m_F = \pm 3$ while the other states are coupled. From studies realised by Boiron *et al.* (Ref. [20]) on the same cesium atomic transition but in a six-beam gray optical molasses we know that the final temperature reached in this cooling mechanism as a function of the light shift parameter $\Omega_R^2/(\delta\Gamma)$ (where $\Omega_R$ is the Rabi frequency) for various detuning

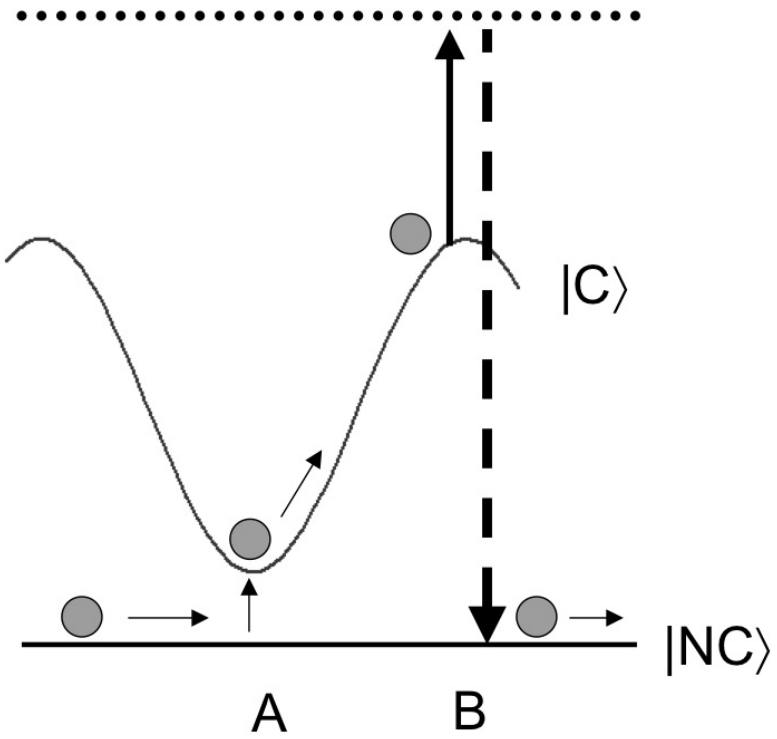


**Figure 4.1**: Cooling mechanism in a gray molasses for a one-dimensional model. Motional coupling between coupled and non-coupled states is position dependent. Transitions from the non-coupled state $|NC\rangle$ and the coupled state $|C\rangle$ take place in A, where the light shift of the coupled state has a minimum, while the ones from the coupled state to the non-coupled take place in B, where the light intensity has a maximum. In this way atoms have climbed a hill of potential energy before returning to the non-coupled state loosing kinetic energy for each cycle.

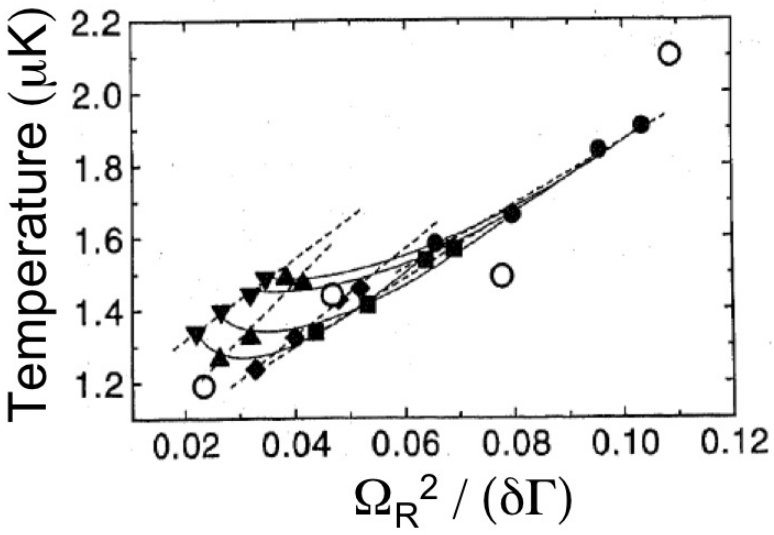


**Figure 4.2**: Temperature of atoms in gray molasses as a function of the light shift parameter $\Omega_R^2/(\delta\Gamma)$ for different intensities and detunings: dashed lines at constant detunings, from left to right, $\delta/\Gamma$=6.8, 5.7, 4.5 3.4 and 2.3; solid lines at constant intensities, from top to bottom, $\Omega^2/\Gamma^2$=0.25, 0.22, 0.18 and 0.16. For a given intensity, there is a clear optimum in detuning. Open circles: numerical results of a three-dimensional quantum Monte Carlo calculation at a fixed detuning of 5Γ. This picture is taken from Ref. [20].

and intensities has the shape presented in Fig. 4.2. We observe a linear dependence of the temperature from the intensity (dashed line) as well as from $1/\delta$ for detuning smaller than 4Γ. For bigger detuning we observe a temperature increasing not expected from the $\Omega_R^2/\delta$ linear dependence law (see Ref. [24]); the heating effect is attributable to the influence of the $F = 3 \Rightarrow F' = 3$ transition that is nearer (it is at only 150 MHz, *i.e.* 28Γ, from the $F = 3 \Rightarrow F' = 2$ transition) and the non-coupled state becomes coupled, though weakly. As we will see in the Sec. 4.4 our experimental results show a qualitative agreement with the ones obtained in Ref. [20].

Finally, we want to emphasize a characteristic difference between bright and gray molasses. In bright molasses the cooling laser is tuned to the *red* side of an atomic transition of the type $F \Rightarrow F' = F+1$, thus in the optical pumping process the atom absorbs a photon of lower energy than the one emitted successively by spontaneous emission and Doppler cooling happens; instead in gray molasses the cooling laser is tuned to the *blue* side of an atomic transition of the type $F \Rightarrow F' = F-1$ or $F \Rightarrow F' = F$, thus in the optical pumping process the atom absorbs a photon of higher energy than the one emitted successively by spontaneous emission and no Doppler cooling is possible, we observe on the contrary Doppler heating. For this reason when we deal with gray molasses we need a pre-cooling step that produces atoms with a kinetic energy in the range of 70-100 $\mu$K. In Ref. [20] (and in general in all the work of the Grynberg group) this pre-cooling is realised using a three-

dimensional magneto-optical trap; we have used instead a three-dimensional optical molasses (Ref. [17]).

## 4.3 Experimental set-up

The experimental set-up (depicted in Fig. 5.6a) is the same used in Ref. [10] to perform the sideband Raman cooling induced by Zeeman effect. We load a source of cesium atoms by a thermal vapour whose pressure is $p \simeq 10^{-8}$ mbar. The atoms are captured in a 3D-optical molasses and then launched vertically with the moving molasses technique. More details about the source can be found in Ref. [17] as well as in Chap. 6.

We perform the collimation in a 2D-optical lattice, 22 cm downstream of the source, in a plane tilted by $3\,^\circ$ with respect to the horizontal. The lattice beams are reflected from gold-coated mirrors to maximise reflectivity (R>97%) and minimise birefringence; improvement is expected from silver ones. The chosen configuration is shown in Fig. 5.6b. Note that this scheme assures both phase stability and symmetry and allows power recycling. For a detailed analysis of the lattice stability see papers [13, 14]. Our study of gray molasses implies a polarisation gradient, thus the half-wave plates slow axis is tilted by an angle $\alpha$ with respect to the vertical $z$-direction (typically $\alpha$=22.5 °), while the quarter-wave plate slow axis is aligned along the vertical ($\beta$=0 °, thus the optical lattice configuration is lin$\perp$lin). The compensation of the magnetic field guaranties that $\mathbf{B} \simeq 0$ with an uncertainty of 5 mG. The lasers that allow the collimation are two: a cooling laser and a pumper laser. The former has a waist radius of 5.7 mm truncated at $r$=9 mm and can be locked on either $F = 3 \rightarrow F'$ or $F = 4 \rightarrow F'$ transitions. A beat between this laser and the repumper laser (see below) allows the setting of the frequency control. Its typical power is limited to few milliwatt. The pumper laser, that pumps back into $F = 3$ the atoms lost due to optical pumping toward $F = 4$ (or viceversa, depending on the cooling laser frequency), has the same characteristics of the cooling laser and its power is below 1 mW. Its polarisation plays no role.

From the collimation plane the atoms beam traces a parabolic path and reaches the detection region after a time of flight of 0.57 s. The detection is realised collecting the fluorescence light emitted isotropically by the cesium atoms excited by a probe laser retro-reflected along the $y$-axis . The probe laser is locked on the $F = 4 \rightarrow F' = 5$ cycling transition, has a power near the saturation and is diaphragmed to 2 mm. Overlapped with it, a repumper laser (power 0.3 mW) allows the detection of the atoms in both $F = 3$ and $F = 4$ hyperfine ground states. More information about the detection in Chap. 3.

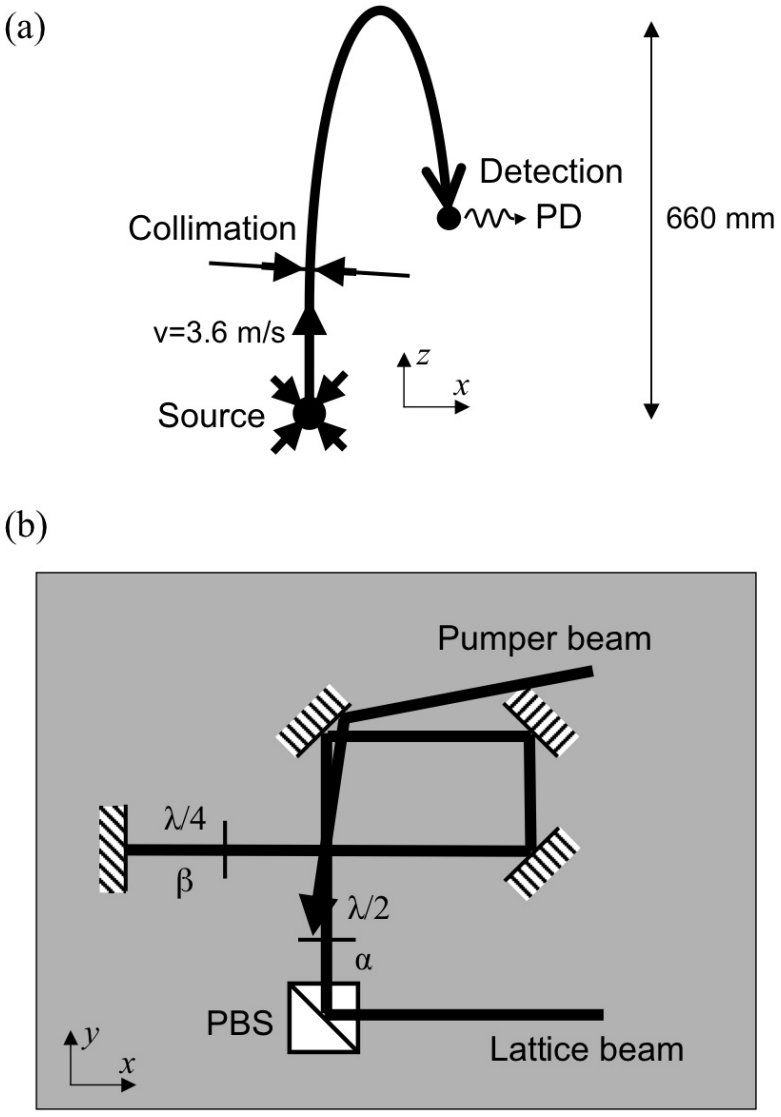


**Figure 4.3**: Scheme of the experiment. a) Vertical plane. The source of the cold atoms continuous beam is a moving molasses of six beams, four of which are shown in the vertical plane. More details about the source in Ref. [17]. PD: photo-detector. b) Beams geometry in the collimation plane. PBS: polariser beam splitter. $\lambda/2$: half-wave plate; the slow axis is tilted by an angle $\alpha$ with respect to the $Oz$ axis. $\lambda/4$: quarter-wave plate; the slow axis is tilted by an angle $\beta$ with respect to the $Oz$ axis. The initial polarisation of the lattice beam is vertical. This figure is taken from Ref. [10] with the kind permission of the author.

## 4.4 Results

In this section we present the experimental results obtained studying the cooling mechanism in a two-dimensional gray molasses for different configurations of the cooling laser and as a function of the various parameters (cooling beam diameter, power and detuning, polarisation gradient, applied transverse static magnetic field, etc.). The pumper laser plays an important role in the efficiency of the cooling process; for each configuration of the gray molasses we have considered all the possible pumping transitions, using first a laser diode on the D1 Cs line and then changing with another diode on the D2 line. After a general overview to check if we find the atomic collimation expected from the theory in the blue side of the $F \Rightarrow F' = F$ and $F \Rightarrow F' = F - 1$ transitions and in the red side of the $F \Rightarrow F' = F + 1$ transition, we study in detail the cooling on the $F = 3 \Rightarrow F' = 2$ atomic resonance and we compare our results to the ones obtained by other laboratories.

### 4.4.1 Measurements with the D1 pumper laser

**Cooling laser scan over the $F = 3 \Rightarrow F' = 2, 3, 4$ transitions**

The first measurements are a scan of the cooling laser frequency over the atomic resonances the $F = 3 \Rightarrow F' = 2, 3, 4$. We have detected the fluorescence signal proportional to the atomic flux at the end of the parabolic flight for the two possible configurations of the D1 pumper laser (linearly polarised) and for different values of the cooling laser power. The pumper laser power was kept fix to 0.6 mW. The results are shown in Fig. 4.4; the upper graph corresponds to a configuration with the pumper laser locked on the $F = 4 \Rightarrow F' = 3$ atomic resonance, the lower one to the pumper laser on the $F = 4 \Rightarrow F' = 4$ transition. As expected from the theory, we have found two peaks due to cooling respectively on the blue side of the $F = 3 \Rightarrow F' = 2$ and $F = 3 \Rightarrow F' = 3$ transitions. Instead there is no evidence of cooling in the region of the $F = 3 \Rightarrow F' = 4$ transition where was expected the cooling mechanism works on the red side of the resonance. We explain the absence of the peak by remarking that this one is a very open transition for both configurations of the pumper laser. Note that the pumper laser is more efficient when it is locked on the $F = 4 \Rightarrow F' = 4$ transition, consistently with the branching ratio of the involved atomic states (see Appendix A); moreover the transition $F = 4 \Rightarrow F' = 3$ has two dark states while $F = 4 \Rightarrow F' = 4$ only one, thus only for this the latter one works better. We note also that the situation where both the cooling peaks are maximised is with a laser power of 10 mW, while for higher values of the power the collimation is worst, probably due to the fact that the pumping rate becomes to high and the atoms are pumped to the non-coupled state

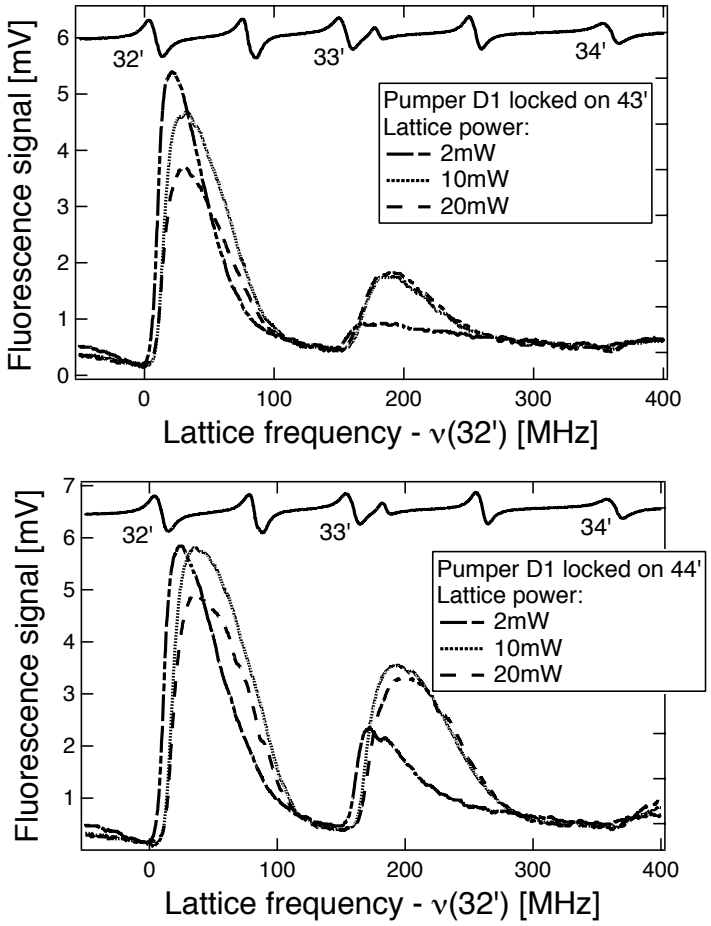


**Figure 4.4**: Cooling laser frequency scan over the $F = 3 \Rightarrow F' = 2, 3, 4$ transitions for different values of the total laser power. The D1 pumper has a power of 0.6 mW and is locked on the 43' atomic transition in the upper graph and on the 44' in the lower one. The upper curve in both graphs is the saturated absorption error signal that we use as reference.

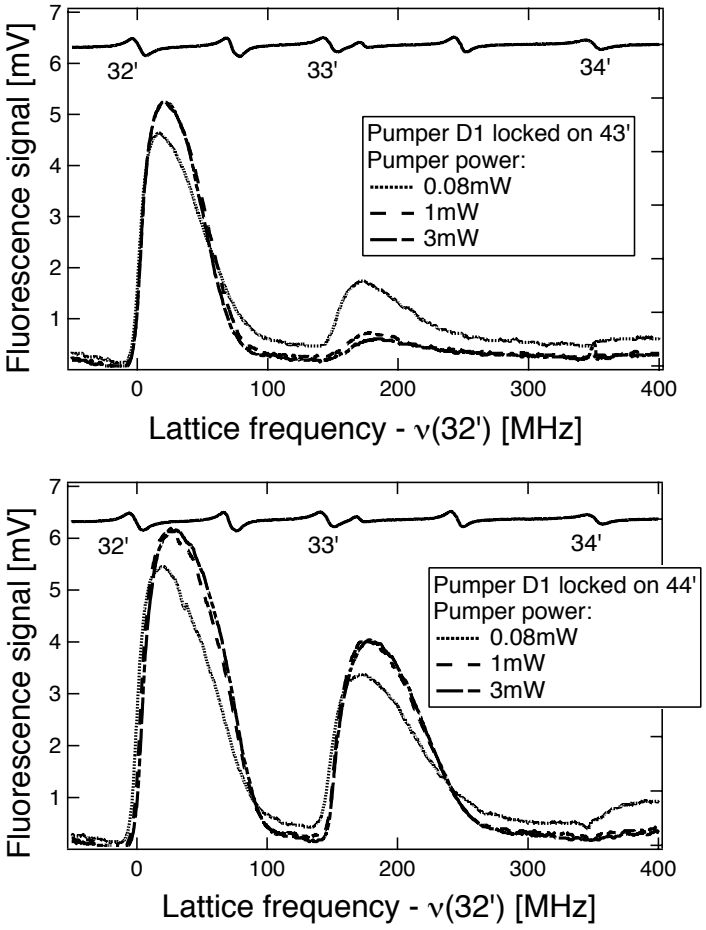


**Figure 4.5**: Cooling laser frequency scan over the $F = 3 \Rightarrow F' = 2, 3, 4$ transitions for different values of the D1 pumper laser power, locked on the 43' atomic transition in the upper graph and on the 44' in the lower one. The cooling laser has a power of 10 mW. The upper curve in both graphs is the saturated absorption error signal that we use as reference.

before reaching the top of the potential hill.

Then we have kept constant the cooling laser power to the optimal value of 10 mW and we have repeated the measurements for different pumper laser powers (Fig. 4.5). The result is almost the same to the one obtained in the previous experiment, and the ideal pumper laser power is around 1 mW.

### Cooling laser scan over the $F = 4 \Rightarrow F' = 3, 4, 5$ transitions

Here the cooling laser is tuned to the $F = 4 \Rightarrow F' = 3, 4, 5$ transitions and the D1 pumper laser is locked either on $F = 3 \Rightarrow F' = 3$ or on $F = 3 \Rightarrow F' = 4$. We have done the same kind of measurements already presented in the previous paragraph, keeping fix first the pumper power to 0.6 mW (Fig. 4.6) and then the cooling laser power to 10 mW (Fig. 4.7). The

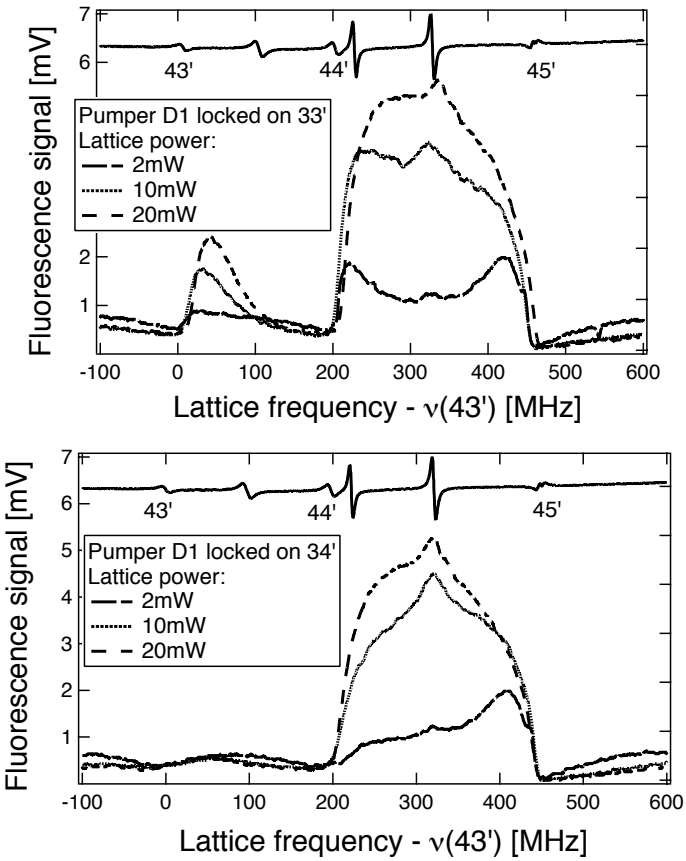


**Figure 4.6**: Cooling laser frequency scan over the $F = 4 \Rightarrow F' = 3, 4, 5$ transitions for different values of the total laser power. The D1 pumper has a power of 0.6 mW and is locked on the 33' atomic transition in the upper graph and on the 34' in the lower one. The upper curve in both graphs is the saturated absorption error signal that we use as reference.

result is an evident sign of cooling in the blue side of the $F = 4 \Rightarrow F' = 4$ transition (gray molasses) and in the red side of $F = 4 \Rightarrow F' = 5$, the latter one being the classic Sisyphus cooling. These two mechanisms work together even better than separately, because the atoms find themselves in a situation where they have to climb first the potential well red-shifted and then the one blue-shifted before being pumped back to the initial state, loosing kinetic energy. From the graphs we can see that this time a cooling power of 20 mW would improve the collimation process, while for the pumper laser the power could be reduced to 0.1 mW. The configuration with the pumper laser locked on $F = 3 \Rightarrow F' = 3$ allows a better re-pumping of the atoms back to $F = 4$ and the branching ratio coefficients confirm this experimental result. What is somewhat surprising is the absence of a peak in the blue side of the $F = 4 \Rightarrow F' = 3$ transition when the pumper laser is locked on $F = 3 \Rightarrow F' = 4$: even if this pumper configuration is not

the optimal one, one would expect to observe a little sign of collimation, as we have in the similar $F = 3 \Rightarrow F' = 2$ transition. We try to explain this behavior by analysing the probability amplitude between the Zeeman sub-levels (Clebsch-Gordan squared coefficients, see Appendix A) for the transition $F = 4 \Rightarrow F' = 3$ and with a pumper locked on $F = 3 \Rightarrow F' = 4$. We consider here the easier situation where the polarisation for both the cooling laser and the pumper laser is $\pi$ (quantization axis along $z$). The cooling mechanism works between the most coupled state $m_F$=0 and the non-coupled state $m_F$=4; the optical pumping is maximum at the top of the potential hill, *i.e.* in $m_F$=0. The atoms that fall into $F = 3$ go either into $m_F$=0 or $m_F$=1, sub-levels strongly coupled to the light field, and they are pumped back to $F = 4$ in a Zeeman sub-level with low $m_F$. In this way they can gain kinetic energy descending the potential hill in part (if they are pumped to the non-coupled $m_F$=4 state), or completely (if they fall again into $F = 3$ where they will be pumped toward a coupled state). On the other hand this effect of the pumper laser is present also for the cooling in the blue side of the $F = 3 \Rightarrow F' = 2$ atomic resonance, but we did not observe it because the transition being closed, the pumper laser is definitively less important.

**Role of the repumper laser superimposed to the probe laser beam**

With the aim of studying in details the cooling optimal conditions in the blue side of the $F = 3 \Rightarrow F' = 2$ atomic resonance, we have checked once again the better configuration of the pumper laser as well as the role of the repumper laser superimposed to the probe laser at the detection. The result, obtained for a cooling laser power of only 2 mW and a pumper power of 0.06 mW, is shown in Fig. 4.8. From the comparison between the graphs b) and c) we find again a higher fluorescence signal when the pumper laser is locked on the $F = 4 \Rightarrow F' = 4$ transition. We note also the important role of the repumper beam at the detection for the same graphs, giving us the information that the greater part of the atoms are in $F = 3$. Fig. 4.8a) has been obtained with the pumper laser switched off: we observe that there is still a sign of cooling for the transition $F = 3 \Rightarrow F' = 2$ and the repumper beam is less important, given the absence of the pumper laser.

### 4.4.2 Detailed study of the $F = 3 \Rightarrow F' = 2$ transition

With the cooling laser and the pumper laser locked respectively on the blue side of the $F = 3 \Rightarrow F' = 2$ and on the $F = 4 \Rightarrow F' = 4$ transitions we have studied the efficiency of the cooling mechanism as a function of some parameters, namely the influence of a static magnetic field, the cooling laser power, detuning, intensity and polarisation gradient.

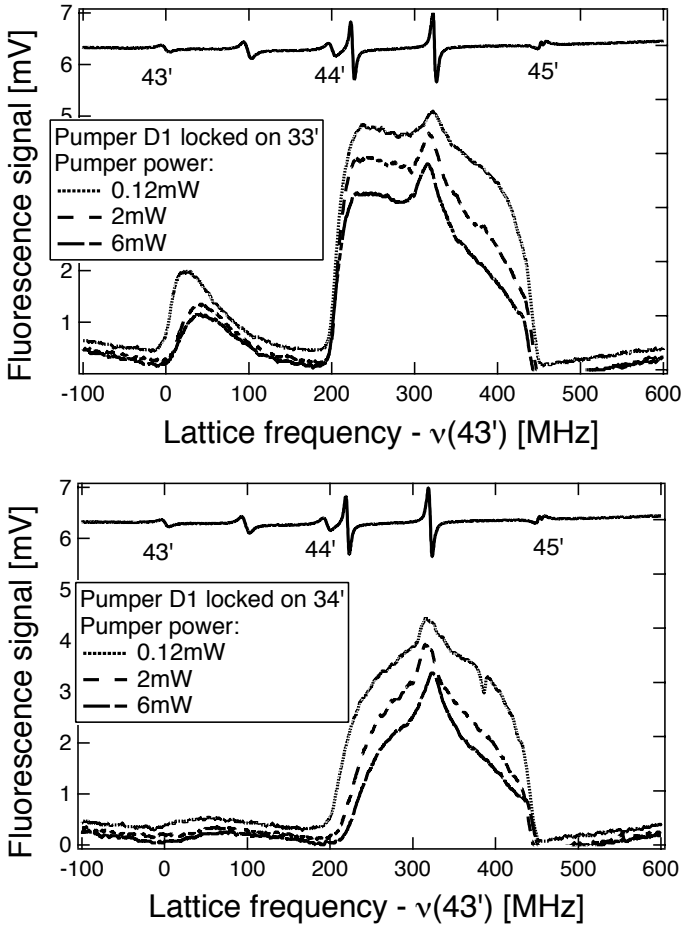


**Figure 4.7**: Cooling laser frequency scan over the $F = 4 \Rightarrow F' = 3, 4, 5$ transitions for different values of the D1 pumper laser power, locked on the 33' atomic transition in the upper graph and on the 34' in the lower one. The cooling laser has a power of 10 mW. The upper curve in both graphs is the saturated absorption error signal that we use as reference.

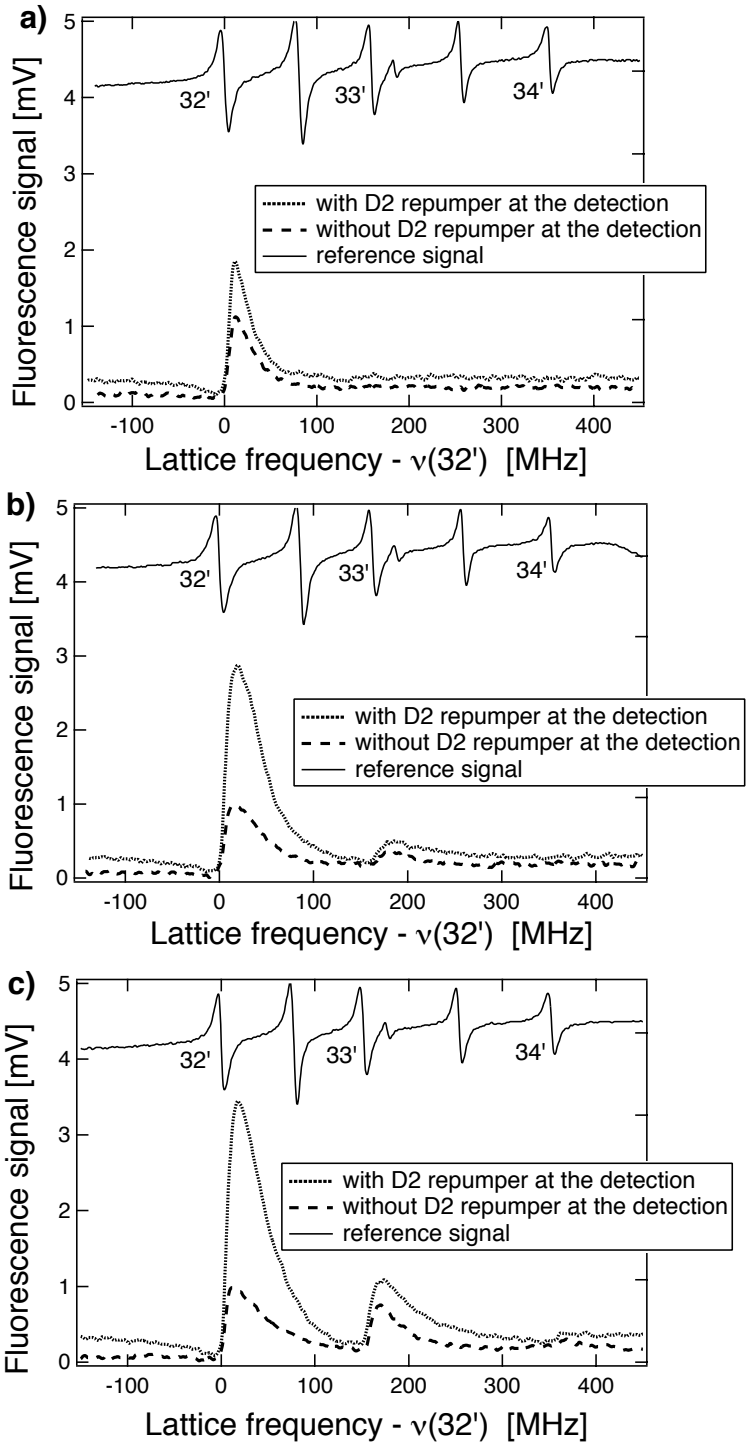


**Figure 4.8**: Cooling laser frequency scan over the $F = 3 \Rightarrow F' = 2, 3, 4$ transitions. The D1 pumper is switched OFF in a), locked on the 43' atomic transition in b) and on the 44' in c). The dotted line corresponds to the case where the D2 repumper superimposed to the probe laser is ON. The dashed line when it is switched OFF. The upper curve in all the three graphs is the saturated absorption error signal that we use as reference. Cooling laser power equal to 2 mW and pumper laser power (when present) to 0.06 mW.

### Effect of a static magnetic field

We have study how the atomic flux and the transverse temperature vary when we apply a static magnetic field along one of the three axes. The magnetic field is generated by a current circulating in a pair of coils in the region where we perform the collimation. The result, reported in Fig. 4.9 for weak variations of the magnetic field around $\mathbf{B}$=0 is a symmetric shape for both temperature and atomic flux, where the symmetry axis is given by the point of zero magnetic field. In this point the atomic flux is maximum (we have detected up to $1.3{\cdot}10^{11}\mathrm{at}{\cdot}\mathrm{s}^{-1}{\cdot}\mathrm{m}^{-2}$ when the magnetic field is applied along the $y$-axis) and the transverse temperature minimum ($T$=3.5$\mu$K). This measurement underlines the fact that a magnetic field destroys the cooling mechanism, then we need to know which is the point of zero-magnetic field. In practice, we have found this point looking for the maximum of the atomic flux. Another interesting remark is that the temperature seems to reach a maximum and then go down again for strong values of the magnetic field. For this reason we have decided to extend our study to stronger values of the magnetic field (see Fig. 4.10). The obtained curves are quite noisy, especially for the temperature, but qualitatively we find again a maximum in temperature at around $T$=10 $\mu$K followed by a region of strong magnetic field where it goes down reaching a new equilibrium temperature of $T$=6 $\mu$K. Regarding the atomic flux, it decreases with the increasing of the magnetic field amplitude. These measurements do not depend from the direction of the magnetic field and have been obtained for a cooling laser power of 5 mW, blue-detuned of 3$\Gamma$ with respect to the $F = 3 \Rightarrow F' = 2$ transition and a pumper power of 0.6 mW. We can compare the results obtained with a strong magnetic field to the ones presented in Ref. [22] and reported in Figs. 4.11 and 4.12. The experimental conditions are quite similar, the main difference is that in Ref. [22] the authors work with a three-dimensional gray molasses while we perform the collimation in a two-dimensional one. The explanation of the low temperatures reached for strong magnetic field amplitudes has to be searched in the different configuration of the atomic system that can not be described as presented here in Sec. 4.2. In fact, in this case the Zeeman shift induced by the magnetic field and the light shift induced by the detuning invert their role and the Hamiltonian is diagonal in the basis where the Zeeman sub-levels are the eigenstates while the optical pumping acts as a small perturbation. We did not investigate this new cooling mechanism, already described for example in Ref. [2, 21, 22].

### Temperature dependence from cooling laser power at fixed detunings

Always with the cooling laser locked on the blue side of the $F = 3 \Rightarrow F' = 2$ atomic resonance we have studied the variation of the final temperature as

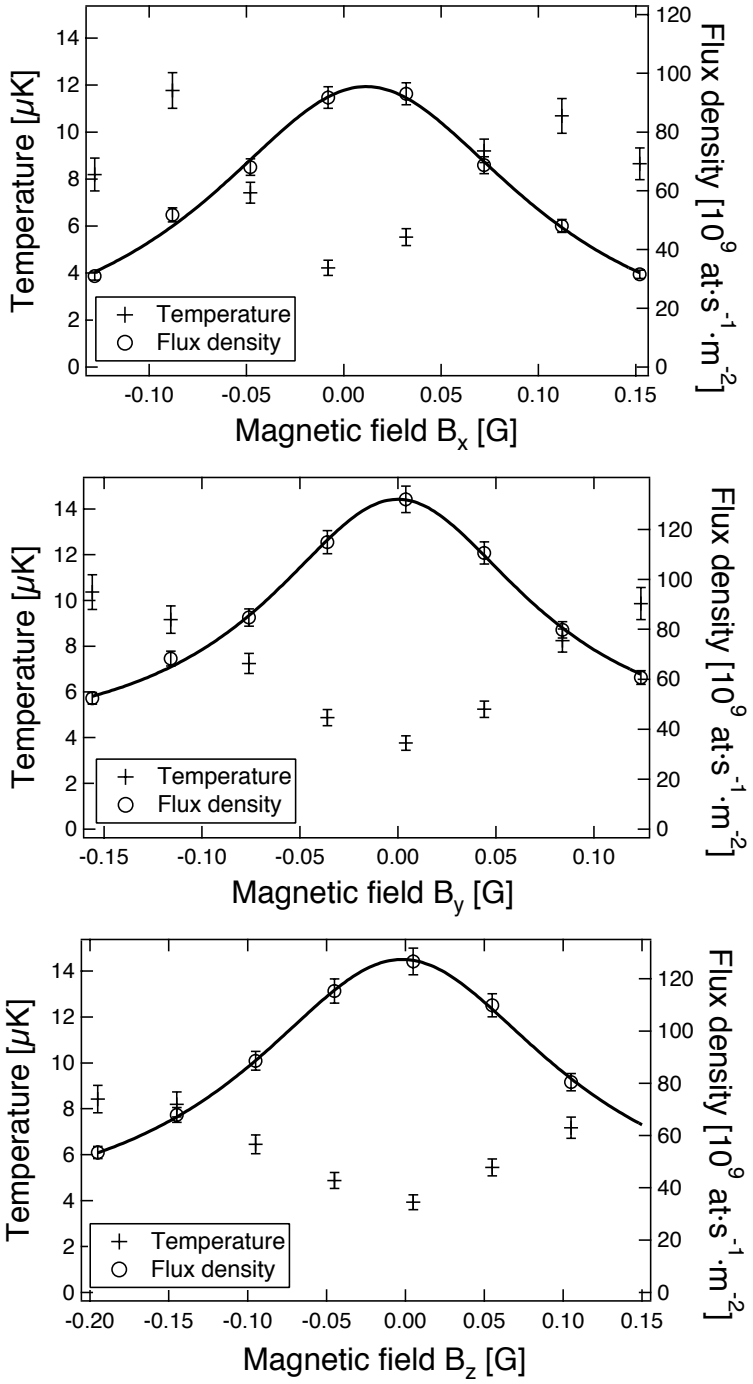


**Figure 4.9**: Transverse temperature and maximum flux density as a function of a weak static magnetic field applied, from top to bottom, along the $x$-axis, the $y$-axis or the $z$-axis. The curve between the data of the flux density serves simply as a guide to the eye.

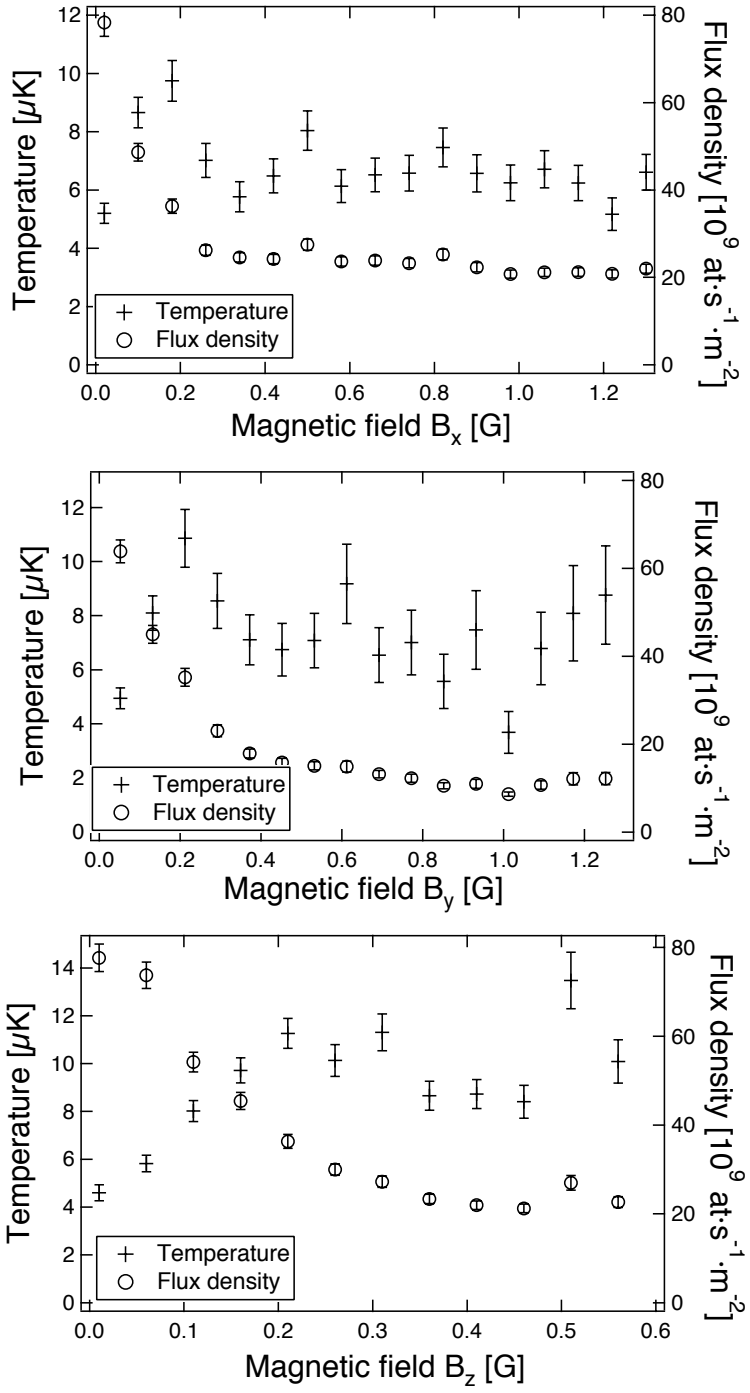


**Figure 4.10**: Transverse temperature and maximum flux density as a function of a strong static magnetic field applied, from top to bottom, along the $x$-axis, the $y$-axis or the $z$-axis.

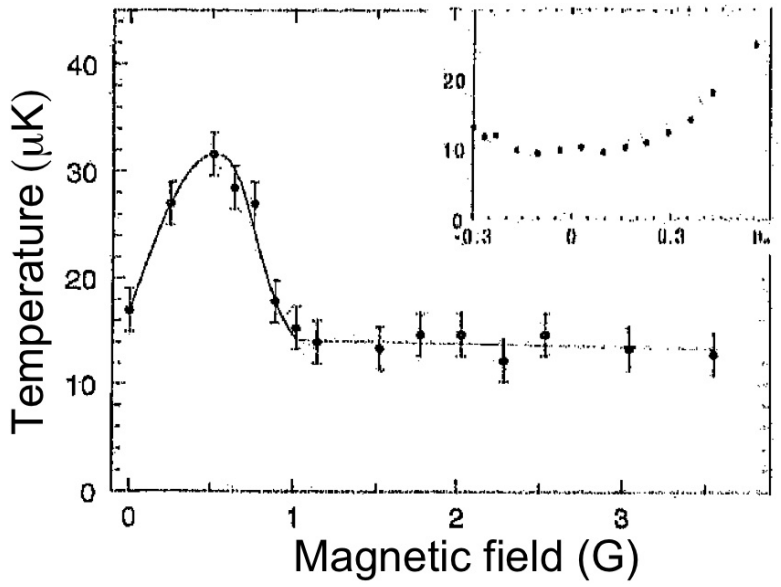


**Figure 4.11**: Variation of the atomic kinetic temperature with the amplitude of a static magnetic field applied along the $z$-axis. The inset shows the detail near B=0. Both curves correspond to a detuning of the molasses field of $5\Gamma$ and an intensity per beam (for a total of six beams ) of 2 mW/cm$^2$. The curve through the data is not fitted and serves simply to guide the eye. This graph is taken from Ref. [22].

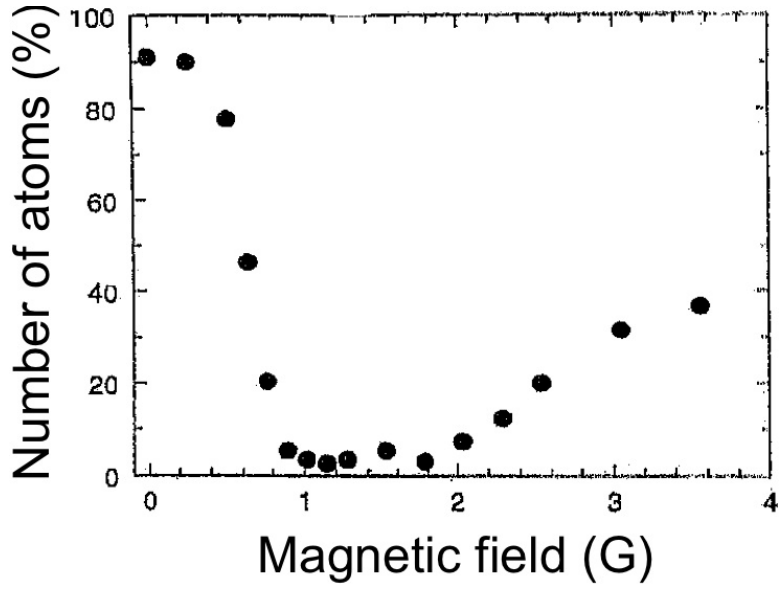


**Figure 4.12**: Variation of the number of atoms in the gray lattice with the amplitude of a static magnetic field applied along the $z$-axis. The 100% stays for the number of atoms in the magneto-optical trap that produces a cold atomic beam at 70 $\mu$K. The graph is taken from Ref. [22].

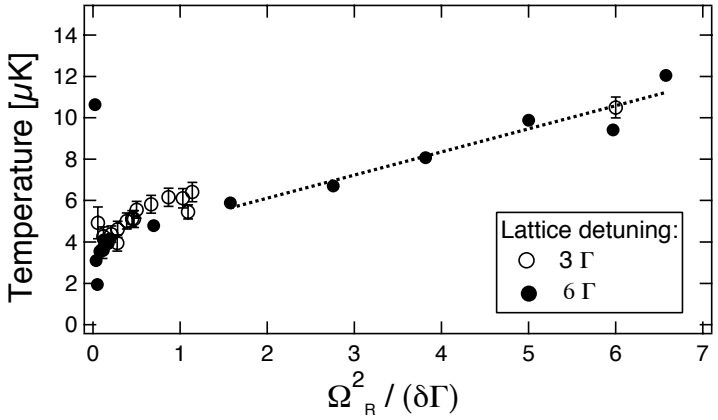


**Figure 4.13**: Variation of the transverse temperature as a function of the light-shift parameter $\Omega_R^2/(\delta\Gamma)$ for a detuning of $3\Gamma$ (open circles) and of $6\Gamma$ (full circles). The pumper laser is locked on the $F = 4 \Rightarrow F' = 4$ transition and has a power of 0.6 mW.

a function of the light-shift parameter $\Omega_R^2/(\delta\Gamma)$ (where $\Omega_R$ is the Rabi frequency) for different fixed detunings $\delta$. The result, shown in Fig. 4.13, is consistent with the universal intensity-detuning law [24]: the temperature varies linearly with the cooling beam intensity. At fixed power, we have obtained lower final temperatures with a cooling laser detuning of $6\Gamma$ compared with the ones obtained with a detuning of $3\Gamma$ but, for a detuning of $9\Gamma$ (not shown in the graph), the temperature goes up again. This behavior is similar to the one found by Boiron *et al.* in Ref. [20] and shown in Fig. 4.2. The authors attribute the heating effect at high detuning to the influence of the nearer $F = 3 \Rightarrow F' = 3$ atomic resonance. The non-coupled $m_F$=3 Zeeman sub-level becomes thus weakly coupled.

### Search for the optimum polarisation gradient and cooling beam diameter and detuning

Finally we have studied the variation of the transverse temperature and the atomic flux as a function of other cooling laser parameters. In Fig. 4.14 we present the graph obtained changing the degree of the linear polarisation between $0\,^\circ$ (configuration lin$\|$lin, vertical) and $45\,^\circ$ (configuration lin$\|$lin, horizontal). As expected, without a polarisation gradient we have no cooling, while for the lin$\perp$lin configuration (half-wave-plate at $22.5\,^\circ$) there is a maximum in the atomic flux. The temperature is almost constant and equal to 3.5 $\mu$K in the region where there is a polarisation gradient (the final temperature depends on the transit time through the gray molasses rather than on the polarisation gradient), while it increases elsewhere (even if not well visible in the picture, due to the problem of extrapolate the temperature

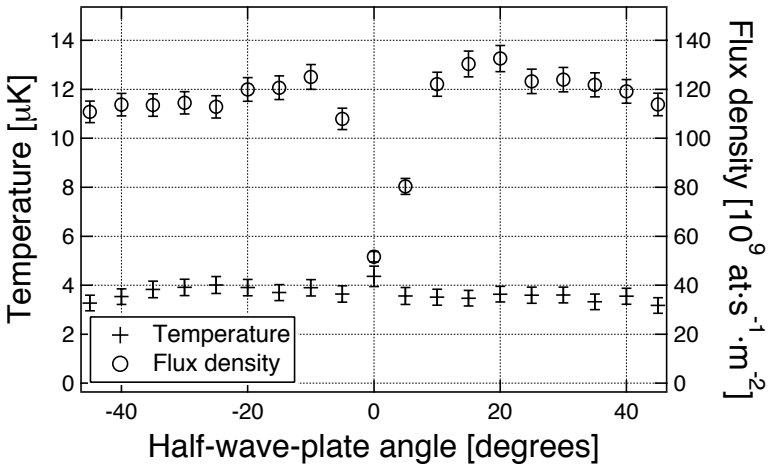


**Figure 4.14**: Variation of the transverse temperature and atomic flux as a function of the polarisation gradient. This measurement is obtained for a cooling laser detuning of 3Γ and power of 5 mW.

from a fit over an atomic beam profile almost null in amplitude). Then we have varied the cooling laser beam diameter (kept until now to the maximum value of 18 mm) between 4 and 18 mm. The result, presented in Fig. 4.15, shows that the atomic flux increases with the increasing of the cooling beam size. This behavior is well understandable by considering that the cooling mechanism, for a fixed polarisation gradient, depends from the transit time of the atoms through the collimation region and this one is proportional to the cooling beam size. The transverse temperature has instead an oscillating shape around the value of 5 $\mu$K.

The last measurement, before switching to a D2 pumper laser configuration, is the search for the optimum detuning in the blue side of the $F = 3 \Rightarrow F' = 2$ transition, to confirm the value of $\delta$=3Γ used previously. The result, obtained with the typical cooling laser parameters, is shown in Fig. 4.16.

### 4.4.3 Measurements with the D2 pumper laser

We have performed a study of the cooling mechanism when we replace the D1 pumper laser with a D2 one. In Figs. 4.17 and 4.18 we present a scan of the cooling laser over the transitions $F = 3 \Rightarrow F' = 2, 3, 4$ and $F = 4 \Rightarrow F' = 3, 4, 5$ respectively, for both the configurations of the D2 pumper laser, as we have done in Figs. 4.5 and 4.7 with the D1 diode. The best configuration of the pumper laser is when it is locked on the $F = 4 \Rightarrow F' = 3$ and on the $F = 3 \Rightarrow F' = 4$ transitions respectively. It is evident in Fig. 4.18 the effect of a more favourable branching ratio. In Figs. 4.19 and 4.20 we have measured the transverse temperature and the atomic flux as a function

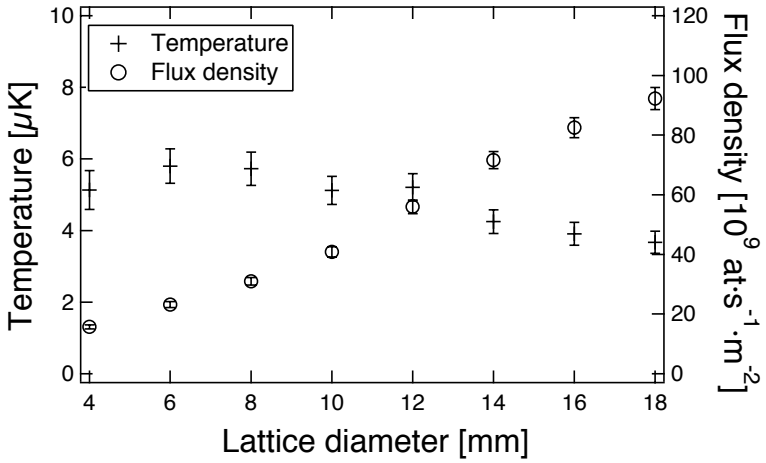


**Figure 4.15**: Variation of the transverse temperature and atomic flux as a function of the cooling laser diameter. This measurement is obtained for a cooling laser detuning of 3Γ and power of 5 mW. The polarisation gradient is lin⊥lin.

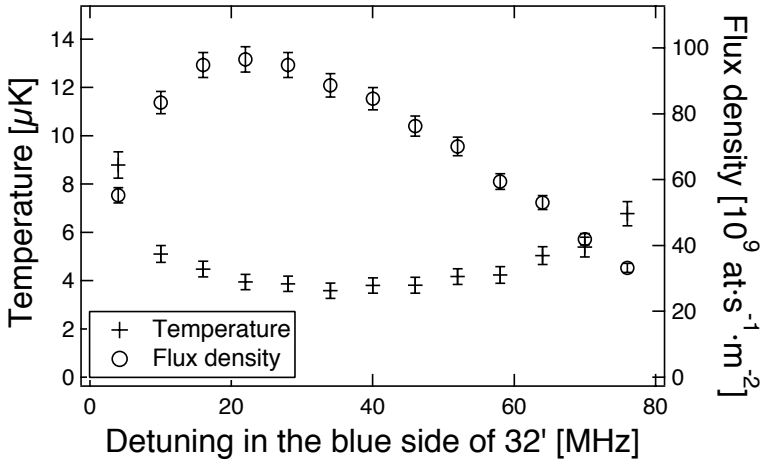


**Figure 4.16**: Variation of the transverse temperature and atomic flux as a function of the cooling laser detuning. This measurement is obtained for a cooling laser power of 5 mW. The polarisation gradient is lin⊥lin.

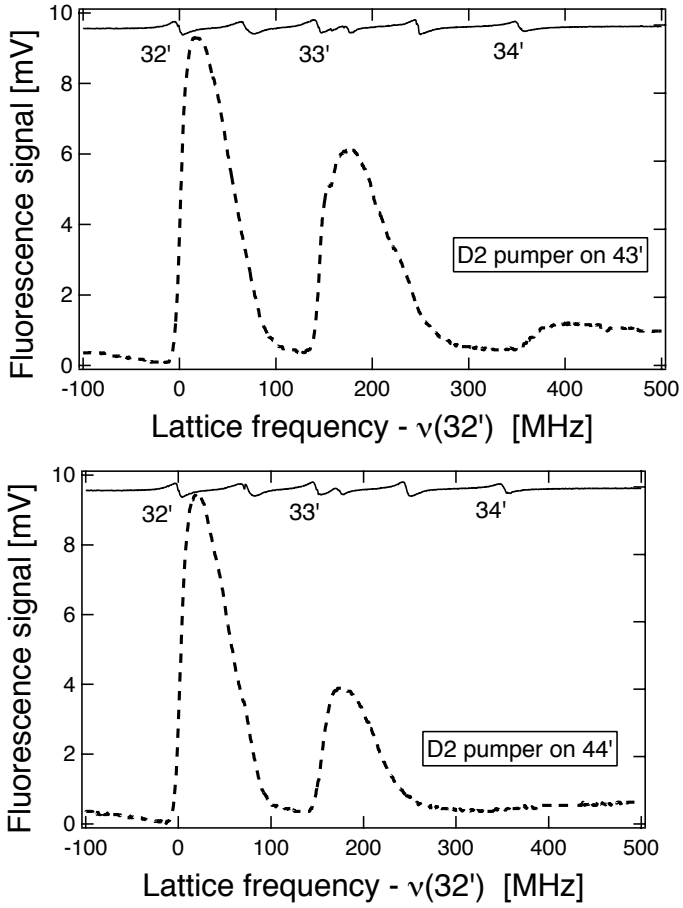


**Figure 4.17**: Cooling laser frequency scan over the $F = 3 \Rightarrow F' = 2, 3, 4$ transitions for a cooling laser power of 10 mW. The D2 pumper has a power of 0.1 mW and is locked on the 43' atomic transition in the upper graph and on the 44' in the lower one. The upper curve in both graphs is the saturated absorption error signal that we use as reference.

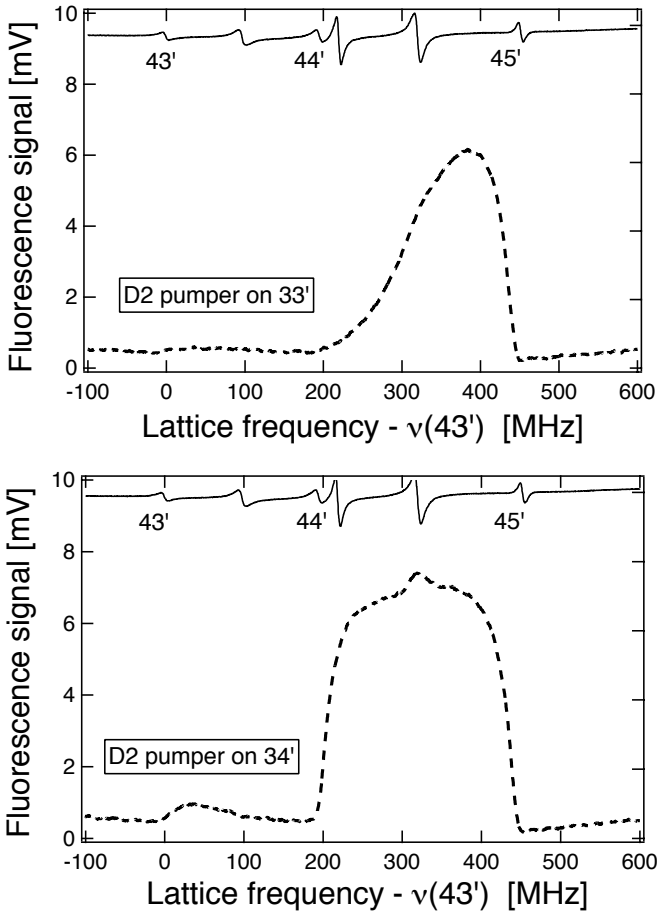


**Figure 4.18**: Cooling laser frequency scan over the $F = 4 \Rightarrow F' = 3, 4, 5$ transitions for a cooling laser power of 10 mW. The D2 pumper has a power of 0.1 mW and is locked on the 33' atomic transition in the upper graph and on the 34' in the lower one. The upper curve in both graphs is the saturated absorption error signal that we use as reference.

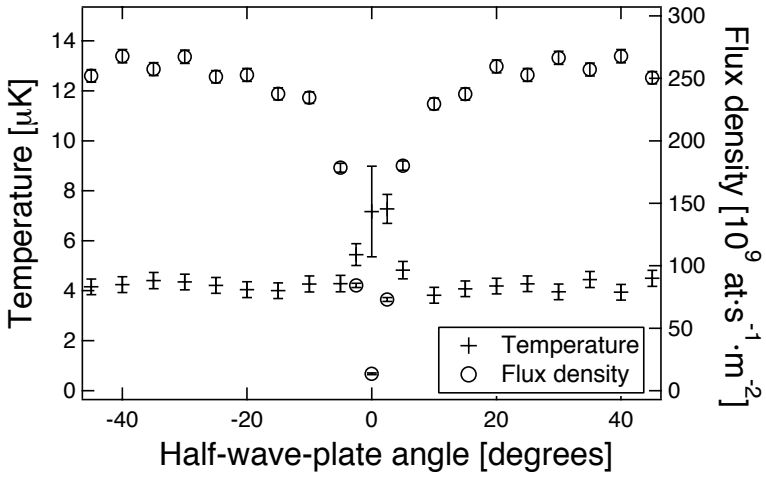


**Figure 4.19**: Variation of the transverse temperature and atomic flux as a function of the polarisation gradient. This measurement is obtained for a cooling laser detuning of 3Γ and power of 3.5 mW. The D2 pumper laser power is 0.12 mW.

of the polarisation gradient and of an applied magnetic field along the $y$-axis when the cooling laser (power 3.5 mW) is locked 3Γ on the blue side of the $F = 3 \Rightarrow F' = 2$ transition. The pumper power is equal to 0.12 mW. The obtained results are substantially similar to the ones obtained with the D1 pumper laser regarding the minimum transverse temperature: it reaches again $T \sim 3.5\ \mu$K. The maximum flux density is instead higher and equal to $\sim 2.7 \cdot 10^{11}$ at$\cdot$s$^{-1}\cdot$m$^{-2}$ for a cooling laser power lower than the one used with the configuration with the D1 pumper laser. This result we attribute to the more favorable branching ratio coefficients of the D2 line in comparison with the D1 one.

## 4.5 Conclusion

To summarise the results obtained in this chapter, we can underline the following points:

- We have observed the cooling mechanism due to the gray molasses as expected from the theory on the transitions of the type $F \Rightarrow F' = F$ and $F \Rightarrow F' = F - 1$.
- We have observed the classical Sisyphus cooling in the red side of the transitions $F \Rightarrow F' = F + 1$; this mechanism can work together with the one that operates in the blue side of $F \Rightarrow F' = F$ (gray molasses).
- The gray molasses cooling mechanism ceases to work if we apply a static magnetic field; this characteristic allows one to find the zero-magnetic field point looking for the maximum of the atomic flux.

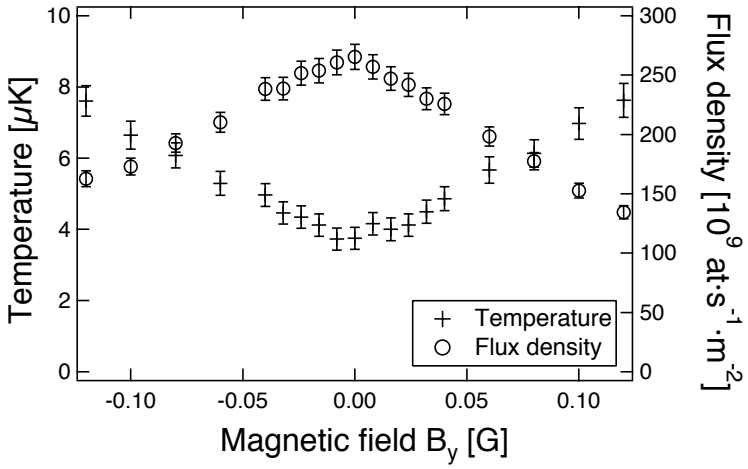


**Figure 4.20**: Variation of the transverse temperature and atomic flux from the amplitude of a weak static magnetic field. This measurement is obtained for a cooling laser detuning of 3Γ and power of 3.5 mW. The D2 pumper laser power is 0.12 mW.

- Using a D1 pumper laser we have measured the minimum transverse temperature $T$=3.5 $\mu$K and the maximum flux density $\varphi$ ∼1.3·10$^{11}$ at·s$^{-1}$·m$^{-2}$ for a cooling laser power of 5 mW and a detuning of 3Γ.
- Switching to a D2 pumper laser we have obtained as best values $T$=3.5 $\mu$K and $\varphi$ ∼2.7·10$^{11}$ at·s$^{-1}$·m$^{-2}$ for a cooling laser power of only 3.5 mW and a detuning of again 3Γ.
- A comparison between the results obtained with this cooling technique and those obtained with the Sisyphus cooling (see Chap. 2 and Ref. [10]) shows however a reduction of the detected atomic flux for a similar transverse temperature.

The aim of the study of this collimation technique was an improvement of the results obtained by performing the Sisyphus cooling in a two-dimensional phase stable optical lattice. We expected lower transverse temperatures and higher atomic flux, due to the low fluorescence rate typical of the gray molasses. The obtained results are thus disappointing. We attribute the not so efficient atom cooling to a transit time (limited by the cooling laser beam size, 18 mm of diameter) of the atoms through the cooling region of only 6 ms, together with an initial temperature of the atomic beam of ∼60 $\mu$K. In a gray molasses there is no Doppler cooling, thus a too high initial temperature may reduce the atomic flux in comparison with a bright molasses (classical Sisyphus cooling), where coexist both Doppler and sub-Doppler cooling.

# Chapter 5

# 2D laser collimation induced by a transverse B-field

We saw in the previous chapter that a transverse laser collimation of an atomic beam can be realised using a polarisation gradient. In its absence, collimation can still be achieved if a transverse magnetic field is applied. The phenomenon, known as MILC (Magnetically Induced Laser Cooling) has been well described since the end of last century by the Metcalf group for a transition $J \Rightarrow J+1$. A corollary of this is the use of such a technique to cancel transverse magnetic fields *in situ*. In this chapter we describe a study of laser collimation of a continuous cesium beam induced by a transverse magnetic field for the less analysed transition $F = 3 \Rightarrow F' = 2$ of the D2 line and its implications for field cancellation. Part of the work presented here is also discussed in Ref. [25].

## 5.1 Introduction

Although MILC was described over a decade ago [26, 27], most of the work has been on $J \Rightarrow J+1$ transitions. Indeed, we observe the effect for red-detuned molasses using the $F = 4 \Rightarrow F' = 5$ component of the Cs D2 line. By contrast, published data on $J \Rightarrow J-1$ transitions are rarer. The group of Metcalf mentions results for the textbook case of 1D collimation of a thermal $^{87}$Rb beam on the $F = 1 \Rightarrow F' = 0$ transition in a weak transverse magnetic field with no polarisation gradient ($\sigma^+$ $\sigma^+$, [28]) and obtained unpublished data for the lin$\|$lin case [29]. The only work on Cs of which we are aware is that of Valentin *et al.* [30] who studied the $F = 3 \Rightarrow F' = 2$ component of the D2 line. In that work and in the experiments of Metcalf's group [26, 27], a thermal atomic beam was collimated in a 1D standing wave to sub-Doppler transverse temperatures in either strong magnetic fields (Larmor frequency $\Omega \geq$ ground-state light shift $\Delta_{LS}$) or weak ones ($\Omega < \Delta_{LS}$). In all of the above, results describe cooling to zero transverse velocity in low fields and

non-zero velocity in high fields. All calculations were numerical simulations and, to the best of our knowledge, no analytical expression for the transverse temperature $T_\perp$ as a function of $B_\perp$ is ever given. Our own experimental work is different in that it concerns 2D collimation of a continuous Cs fountain using an optical lattice with parallel linear polarisation vectors; the magnetic fields are always weak ($B_\perp < 1.2$ G) and the atoms, already cold to begin with, (longitudinal temperature 75 $\mu$K, $T_\perp$=60 $\mu$K) are transversely cooled to about 5 $\mu$K.

In this chapter, we present a detailed study of this particular cooling mechanism including the influence of applied transverse magnetic fields on the atomic flux and final temperature for the case of an $F \Rightarrow F-1$ transition. We show that, even if the mechanism appears on the blue side of the atomic transition, it is different from usual gray molasses in two respects. First, gray molasses requires a polarisation gradient, which is not the case here. Second, the mechanism requires a transverse magnetic field, which is known to destroy gray molasses (see Ref. [21] and Chap. 4). In fact, we have found it to be a more sensitive tool than the latter for *in situ* compensation of residual transverse fields at the milligauss level. We outline the experimental arrangement then present the results obtained. Then we compare our situation with gray molasses ($F \Rightarrow F$ or $F-1$ with a polarisation gradient). To gain some physical insight, we present analytical calculations for magnetically induced 1D cooling of a $J = 3/2 \Rightarrow J' = 1/2$ transition in linearly polarised light. We obtain expressions for the friction and diffusion coefficients and thereby $T_\perp$ *versus* $B_\perp$. These reproduce both the general behaviour and the magnitude of results for 2D cooling using the more complicated $F = 3 \Rightarrow F' = 2$ transition. Lastly, we present the transverse magnetic field cancellation procedure based on real-time measurement of the atomic flux.

## 5.2 Cooling mechanism

The MILC process can be easily explained by a simple 1D-model for both the transitions $J \Rightarrow J+1$ and $F \Rightarrow F$ or $F-1$ in the limit of a weak magnetic field. In the following we present a scheme of the cooling mechanism for these two configurations.

### 5.2.1 Configuration $J \Rightarrow J+1$

Let's consider a 1D-standing wave of circular polarisation $\sigma^+$ and negative detuning $\delta < 0$. Atoms travelling through the standing wave are pumped into the state $m_J = +J$, then climb the potential hill and reach the region where there is no light shift (no light); here the magnetic field makes a mixing

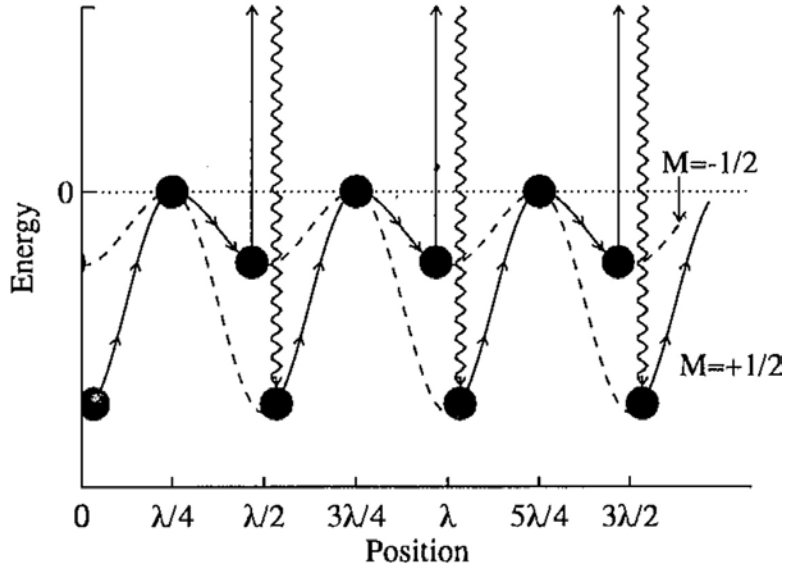


**Figure 5.1**: Spatial dependence of the light shifts of the ground-state sub-levels of the $J = 1/2 \Rightarrow J' = 3/2$ transition for the case of a purely $\sigma^+$ standing wave that has no polarisation gradient, and is appropriate for magnetically induced laser cooling. The arrows show the path followed by atoms being cooled in this arrangement. Atoms starting at $z$=0 in the strongly light-shifted $m_J = +1/2$ sub-level must climb the potential hill as they approach the node at $z$=$\lambda/4$. There they undergo Zeeman mixing in the absence of any light and may emerge in $m_J = -1/2$ sub-level. They will then gain less energy as they approach the antinode at $z$=$\lambda/2$ than they lost climbing into the node. Then they are optically pumped back to the $m_J = +1/2$ sub-level in the strong light of the antinode, and the process repeats until the atomic kinetic energy is too small to climb the next hill. Each optical pumping event results in absorption of light at a lower frequency than emission, thus dissipating energy to the radiation field. This picture is taken from Ref.[2].

between the different Zeeman sub-levels, atoms are re-distributed in states less coupled with laser light and when they descend the potential hill they gain less energy than they lost climbing the hill. Once in the antinode the optical pumping put the atoms back in the $m_J = +J$ state. Fig. 5.1, taken from Ref.[2], shows a picture of the cooling process in the particular case $J = 1/2 \Rightarrow J = 3/2$.

For an efficient cooling mechanism two conditions are required on the atom velocity $v$: first, $v$ must be high enough to guarantee the non adiabatic condition; second, $v$ must be small in order that the transit time through the region of the antinodes allows the optical pumping to work. Thus, if $\Omega$ is the Zeeman precession frequency and $\gamma_p$ the optical pumping rate, we need:

$$\Omega < kv < \gamma_p \tag{5.1}$$

where $k$=$2\pi/\lambda$ is the wave vector. When these conditions are satisfied and the laser frequency is red-detuned with respect to the atomic resonance frequency, sub-Doppler cooling using MILC can be observed.

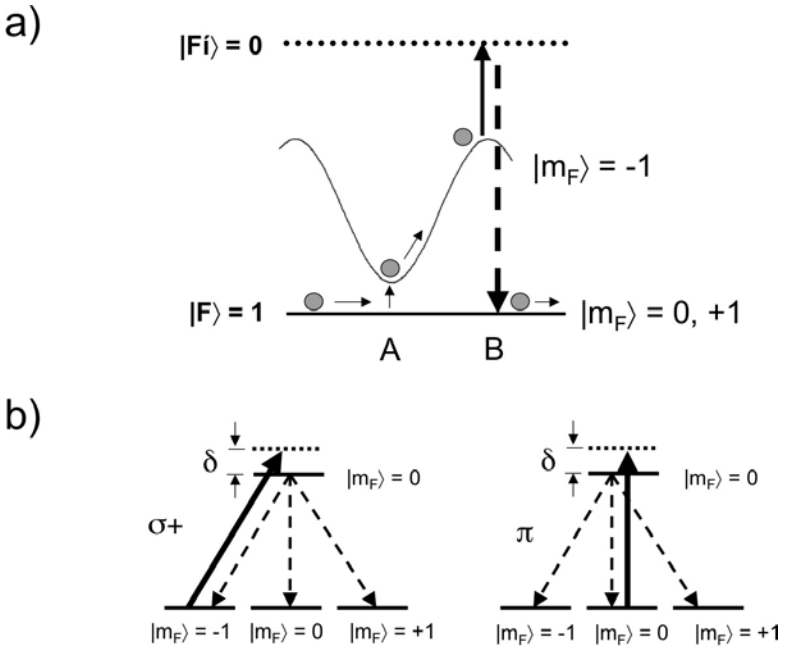


**Figure 5.2**: Spatial dependence of the light shifts of the ground-state sub-levels of the $F = 1 \Rightarrow F = 0$ $^{87}$Rb transition for the case of a purely $\sigma^+$ standing wave that has no polarisation gradient. Optical pumping put the atoms in the non-coupled dark Zeeman sub-levels $m_F = +1$ or $m_F = 0$. They stay in these states until they reach the node of the coupled $m_F = -1$; here the three sub-levels are degenerate and the Zeeman shift is comparable with the light shift. Population mixing induced by the magnetic field repopulates the coupled $m_F = -1$ sub-level, atoms climb the potential well and once on the top of the hill they undergo optical pumping back to the non-coupled states. Each optical pumping event results in absorption of light at a higher frequency than emission but the energy dissipation occurs after the population mixing, when atoms climb the potential hill. This cooling process works also for a linear $\pi$ polarised light field, as shown in b). This figure is adapted from Ref. [29].

### 5.2.2 Configuration $F \Rightarrow F - 1$ or $F$

The MILC process for such configuration is depicted in Fig. 5.2 for a transition in the blue of $F = 1 \Rightarrow F' = 0$ and again circular $\sigma^+$ polarisation of the standing wave. Atoms that enter the standing wave in $m_F = -1$ climb the potential hill and are then optically pumped in the $m_F = 0$ or $m_F = +1$ dark states, not coupled with the light field. They travel in these states until they reach the region where the light shift of the coupled state is zero. Here all the Zeeman sub-levels are degenerate and magnetic field population mixing occurs, so the process starts again.

Requirements on the atoms velocity introduced in the previous paragraph have to be satisfied also in this configuration. Note that here the laser frequency detuning is in the blue side of the atomic resonance, so $\delta > 0$.

In our own experiment, the MILC has been realised in a 2D-optical lattice linearly polarised; we locked the laser frequency on the blue side of the $F =$

$3 \Rightarrow F' = 2$ atomic transition of the $^{133}$Cs $D_2$ line. In this less easy configuration the $m_F = \pm 3$ Zeeman sub-levels play the role of the non-coupled states while the other sub-levels are strongly coupled to the light field. In fact the influence of the adjacent $F' = 3$ excited state induces a modulated light shift of the two non-coupled states, though rather weak. The Sisyphus mechanism breaks down for very weak magnetic field when an atom moving at the recoil velocity $\hbar k/M$ passes too quickly through the region of efficient B-mixing for optical pumping to occur. This explains qualitatively the peak in temperature and the dip in the flux near $B_\perp = 0$ (see later the experimental results, Figs. 5.11 and 5.12). Let us estimate the Zeeman splitting at which it happens. The spatial size $x$ of the region where the B-mixing works is defined by

$$\frac{\Omega_R^2 \cdot (kx)^2}{\delta} \approx \Omega \tag{5.2}$$

that is the optical energy shift is comparable with the Zeeman splitting. In the formula $\Omega_R \sin kx \simeq \Omega_R kx$ is the local Rabi frequency in the vicinity of the well bottom averaged over the lattice volume and $\delta$ is the frequency detuning. An atom with the recoil velocity crosses this region in a time $\tau = x/(\hbar k/M)$. Replacing $x$ and multiplying the previous expression by $\Omega^2$ we obtain

$$\frac{\Omega_R^2}{\delta} \cdot \ k^2 \cdot (\frac{\hbar\ k}{M})^2 \cdot (\tau\ \Omega)^2 \approx \Omega^3 \tag{5.3}$$

For efficient mixing in this time period we need $(\tau\ \cdot \Omega) \geq 1$, so finally we find the relation:

$$\Omega \geq [4 \cdot \frac{\Omega_R^2}{\delta} \cdot \ \omega_r^2]^{1/3} \tag{5.4}$$

where $\omega_r$ is the recoil frequency $(\hbar\ k^2/2M)$. This power law is confirmed experimentally (see Fig. 5.14) over a range of 30 in laser power.
In the limit of very low atom velocities and for a three-state model of the atom, our Russian colleagues V. Yudin and A. Taichenachev have calculated numerically the expression of the force acting on the atoms as a function of the atom velocity and the variation of the transverse temperature and flux density as a function of the applied magnetic field. A typical result of these calculations is shown in Figs. 5.4 and 5.5. In the former we can see a linear dependence very close to $v$=0 and then a series of Raman resonances (for $mkv \simeq \Omega$ [27]), while in the latter we observe a quadratic variation of the transverse temperature with the magnetic field amplitude that we find again in our experimental data, as well as a little difference between the magnetic field value that minimises the temperature and the one that maximises the flux density (see Sec. 5.4, Fig. 5.11). A qualitative picture of the adiabatic

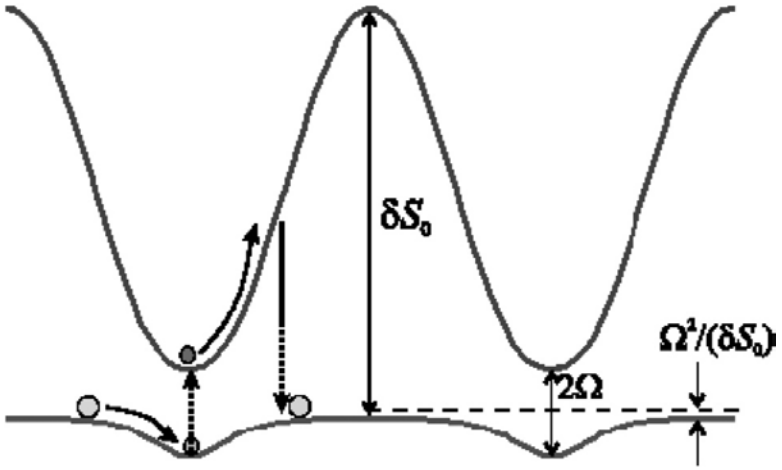


**Figure 5.3**: Adiabatic potentials and radiative transitions between them for an atom moving in positive direction. Circles indicate the stationary dressed-state populations. The modulated light shift of the non-coupled level arises from off-resonant coupling with the excited $F' = 3, m_F = 3$ level. $\Omega$ is the Zeeman splitting, $S_0 = 2\ \Omega_R^2/\Gamma^2$ the on-resonance saturation parameter and $\delta$ the laser frequency detuning. Note that due to the low velocity of the atom the optical pumping put the atom back into the non-coupled state before it could reach the top of the potential hill.

potentials and cooling principle is given in Fig. 5.3. The kinetic energy dissipated per cycle is of the order of the Zeeman energy.

## 5.3 Experimental set-up

The experimental set-up (depicted in Fig. 5.6a) is the same used in Ref. [10] to perform the sideband Raman cooling induced by Zeeman effect. We load a source of cesium atoms by a thermal vapour whose pressure is $p \simeq 10^{-8}$ mbar. The atoms are captured in a 3D-optical molasses and then launched vertically with the moving molasses technique. More details about the source can be found in Ref. [17] as well as in Chap. 6.

We perform the collimation in a 2D-optical lattice, 22 cm above the source, in a plane tilted by $3^\circ$ with respect to the horizontal. The lattice beams are reflected from gold-coated mirrors to maximise reflectivity (R>97%) and minimise birefringence; improvement is expected from silver ones. The chosen configuration is shown in Fig. 5.6b. Note that this scheme assures both phase stability and symmetry and allows power recycling. For a detailed analysis of the lattice stability see papers [13, 14]. Our study of MILC does not imply a polarisation gradient, thus the quarter- and half-wave plates slow axes are aligned along the vertical $z$-direction: $\alpha$=$\beta$=$0^\circ$. The transverse magnetic field **B** is aligned along the $y$-direction and its typical value is of 70 mG, which corresponds to a Zeeman splitting of 24.5 kHz (see

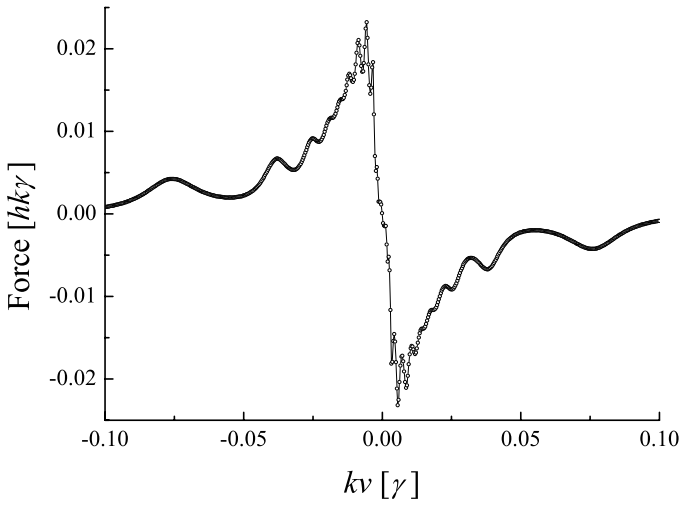


**Figure 5.4**: Three-state model. Variation of the spatially averaged force in $\hbar k\Gamma$ units versus $kv/\Gamma$. The detuning $\delta = 3\,\Gamma$, the Zeeman splitting $\Omega = 0.01\,\Gamma$, and the Rabi frequency $\Omega_R = \Gamma$. Note that in the picture the natural width $\Gamma$ is indicated as $\gamma$.

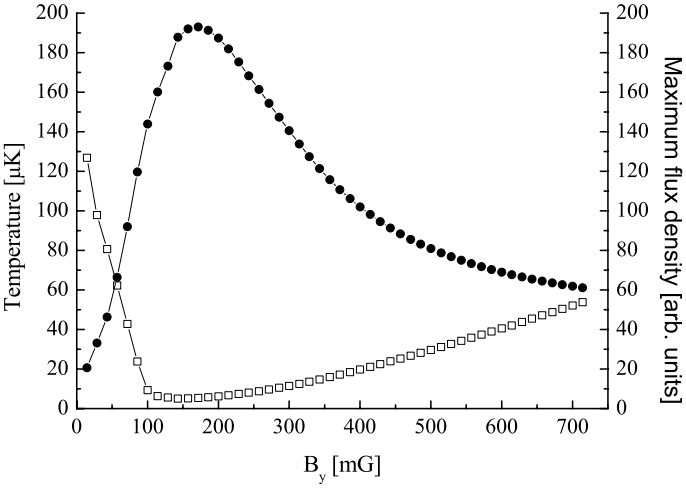


**Figure 5.5**: Three-state model. Maximum flux density (•) in arbitrary units and the temperature (○) in microkelvin versus magnetic field in mG. The parameters are $\delta = 3\Gamma$, $\Omega_R = \Gamma$. There is qualitative agreement with the experiment (see Fig. 5.13).

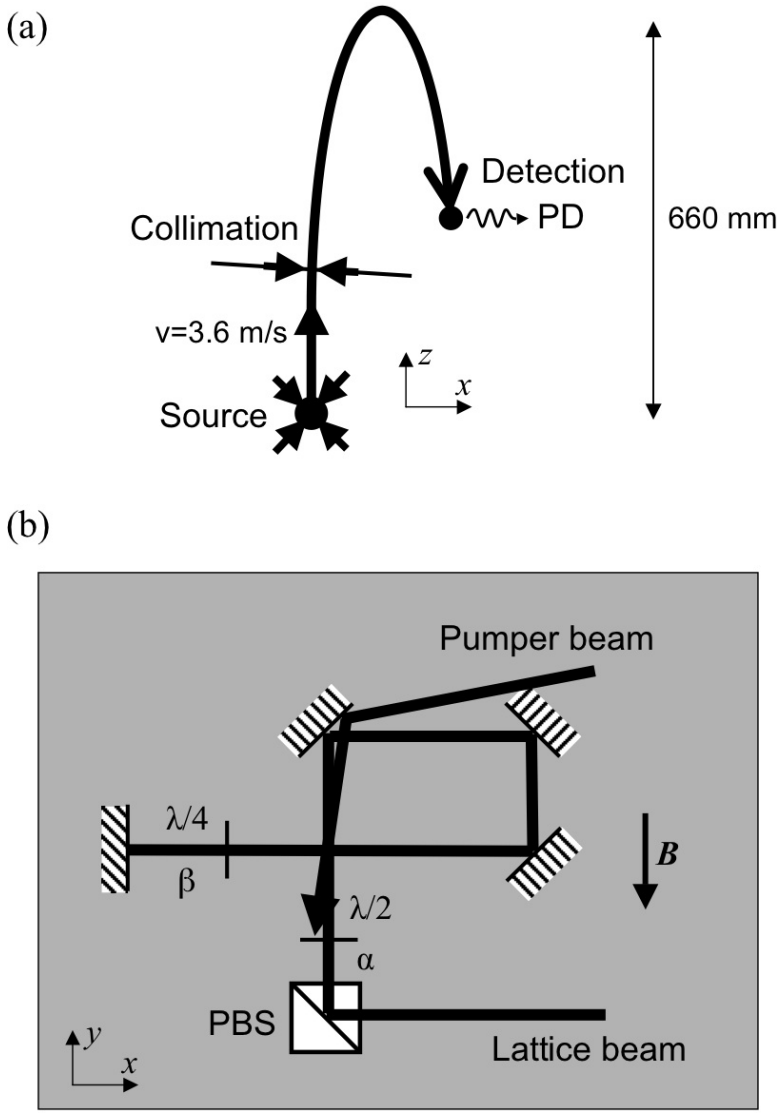


**Figure 5.6**: Scheme of the experiment. a) Vertical plane. The source of the cold atoms continuous beam is a moving molasses of six beams, four of which are shown in the vertical plane. More details about the source in Ref. [17]. PD: photo-detector. b) Beams geometry in the collimation plane. PBS: polariser beam splitter. $\lambda/2$: half-wave plate; the slow axis is tilted by an angle $\alpha$ with respect to the $Oz$ axis. $\lambda/4$: quarter-wave plate; the slow axis is tilted by an angle $\beta$ with respect to the $Oz$ axis. The initial polarisation of the lattice beam is vertical. This figure is taken from Ref. [10] with the kind permission of the author.

Appendix A). The lasers that allow the collimation are two: a cooling laser and a pumper laser. The former has a waist radius of 5.7 mm truncated at $r$=9 mm and can be locked on either $F = 3 \rightarrow F'$ or $F = 4 \rightarrow F'$ transitions. A beat between this laser and the repumper laser (see below) allows the setting of the frequency control. Its typical power is limited to few milliwatt. The latter, used to pump back into $F = 3$ the atoms lost due to optical pumping toward the ground state $F = 4$ (or viceversa, depending on the cooling laser frequency), has the same characteristics as the cooling laser and its power is below 1 mW. Its polarisation plays no role.

From the collimation plane the atoms beam traces a parabolic path and reaches the detection region after a time of flight of 0.57 s. The detection is realised collecting the fluorescent light emitted isotropically by the cesium atoms excited by a probe laser retro-reflected along the $y$-axis . The probe laser is locked on the $F = 4 \rightarrow F' = 5$ cycling transition, has a power near the saturation and is diaphragmed to 2 mm. Overlapped with it, a repumper laser (power 0.3 mW) allows the detection of the atoms in both $F = 3$ and $F = 4$ hyperfine ground states. More information about the detection and the transverse temperature measurement in Chap. 3.

## 5.4 Results

We have realised a detailed study of the cooling mechanism for the transition $F = 3 \Rightarrow F' = 2$. The influence of the cooling laser frequency detuning, its power and its optical diameter on the detected density flux has been analysed as well as the role of the pumper laser frequency and the intensity of the applied transverse magnetic field . We have tried both the D1 and D2 lines for the pumper laser frequency, replacing the ECDL on the optical table. The cooling mechanism has been observed also in a configuration $F \Rightarrow F' = F + 1$ with the cooling laser tuned to the $F = 4 \Rightarrow F' = 3, 4, 5$ transitions.

### 5.4.1 Cooling on the blue side of the $F = 3 \Rightarrow F' = 2$ transition

#### Measurements with the D1 pumper laser

The first measurement made is a study of the variation of the detected fluorescence signal for a frequency scan of the cooling laser. We store at the same time its saturated absorption error signal to identify the hyperfine components. The result, shown in Fig. 5.7, confirms that the cooling mechanism works in the blue side of the 32' transition (and also on the blue side of the 33'). The upper graph is obtained using the D1 pumper locked on the 43' atomic resonance, for the second one we locked it on the 44' resonance. The

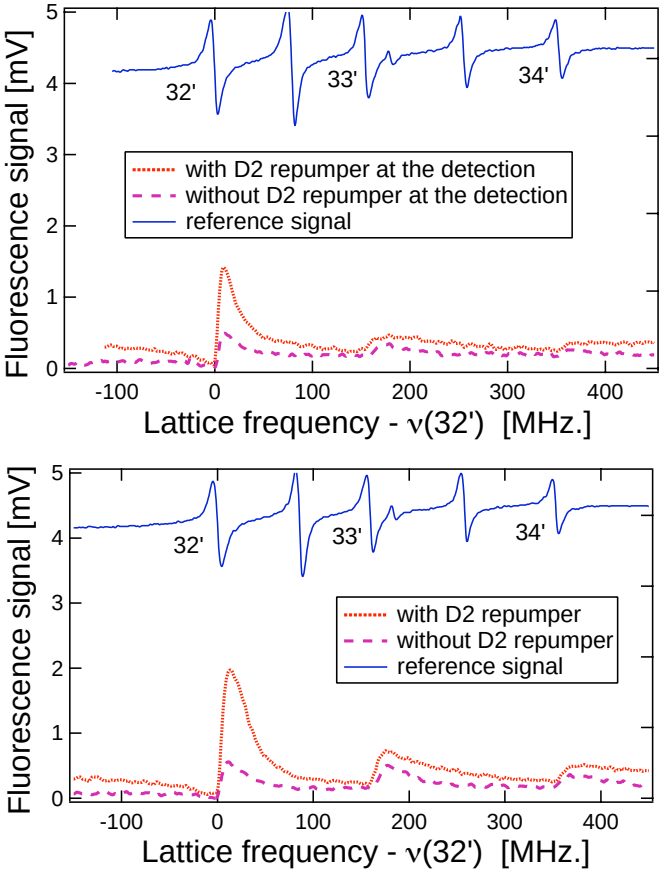


**Figure 5.7**: Cooling laser frequency scan around the resonance frequency 32'. The D1 pumper is locked on the 43' atomic transition in the upper graph and on the 44' in the lower one. The dotted line corresponds to the case where the D2 repumper superimposed to the probe laser is ON. The dashed line when it is switched OFF. The upper curve in both graphs is the saturated absorption error signal that we use as reference.

D2 repumper laser, superimposed to the probe laser, allows the detection of atoms lying in either $F = 3$ or $F = 4$ ground states. The dashed line in both graphs corresponds to a situation where we have switched OFF this repumper laser.

The experimental conditions were: cooling laser power 2 mW and D1 pumper laser power 0.06 mW; the other parameters as set in Sec. 5.3. We note that the detected cold atoms flux is enhanced for the configuration with the pumper laser locked on 44'. This is consistent with the branching ratio in spontaneous emission for the $^{133}$Cs D1 line: optical pumping toward $F = 3$ is more efficient from $F' = 4$ rather than $F' = 3$ (see Appendix A). We note also the strong reduction of the detected atomic flux when the repumper laser superimposed to the probe laser is OFF; this means that most of the atoms lie in the $F = 3$ ground state.

We have repeated this measurement without the D1 pumper laser, again

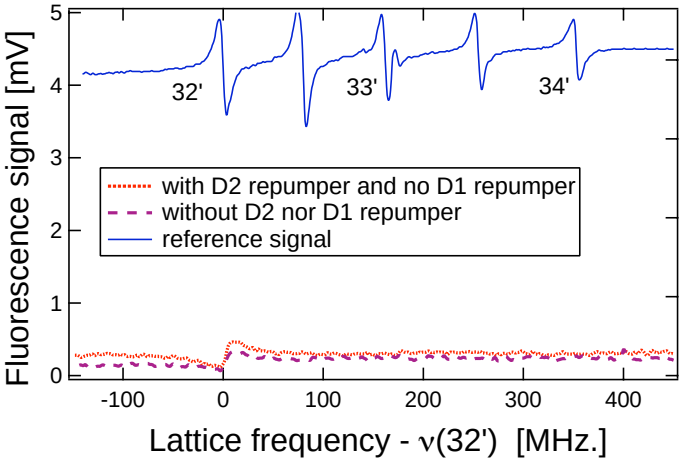


**Figure 5.8**: Same conditions of the fig. 5.7 but now the pumper laser is OFF.

for the two situations with and without repumper laser at the detection and always for a cooling laser power of 2 mW. The result, in Fig. 5.8, is a very weak detected flux, due to the loss of almost all atoms during the cooling process: the atoms are pumped into $F = 4$ and definitively lost before they can be cooled.

We have searched then for the frequency detuning of the cooling laser that optimises the detected atomic flux focusing our study in the blue side of the 32' hyperfine transition; for this purpose we have increased the power of both the cooling laser and the pumper laser (locked on the 44') to 5 mW and 0.6 mW respectively. The transverse magnetic field is kept at 70 mG. In Fig. 5.9 one can see the result of this measurement, giving an optimal frequency detuning of +20 MHz. The calibration of the atomic flux is obtained by signal to noise ratio (details of the calibration in the previous chapter). The transverse temperature reaches the minimum value of 5 $\mu$K.

Before switching to a configuration with a D2 pumper (rather than the D1 used until now) we have analysed how the transverse temperature and the atomic flux change as a function of the cooling laser beam diameter. To do this we have inserted a diaphragm between the exit of the optical fibre and the polariser beam splitter (see Fig. 5.6) and we have changed its aperture from 4 to 18 mm by step of 2 mm. The experimental conditions are the same of the previous measurement. As shown in Fig. 5.10 the bigger the cooling laser beam diameter the better the cooling effect. When we reduce the size of the optical lattice (with the diaphragm) we reduce also the transit time of the atoms through the optical lattice; this yields a less efficient cooling. On the other hand we can not increase the cooling laser beam diameter beyond 18 mm for geometrical reasons.

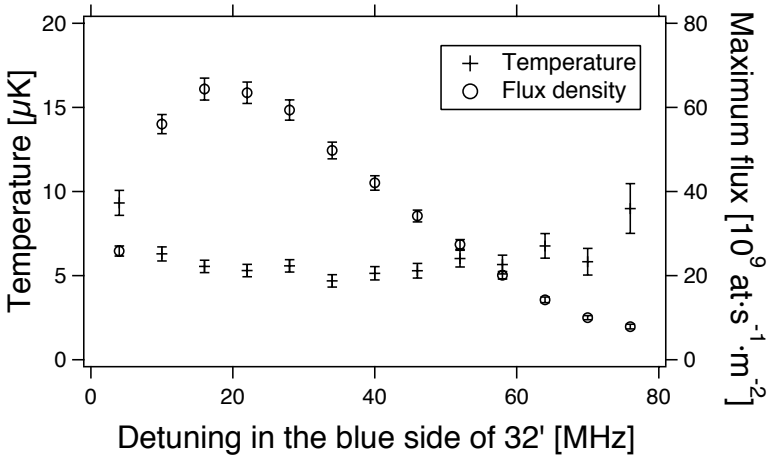


**Figure 5.9**: Transverse temperature and atomic flux density as a function of the frequency detuning of the cooling laser around the atomic transition 32'. The cooling laser power is 5 mW. The pumper laser, locked on the 44' transition of the D1 line, has a power of 0.6 mW. The applied transverse magnetic field along the $y$-axis is 70 mG.

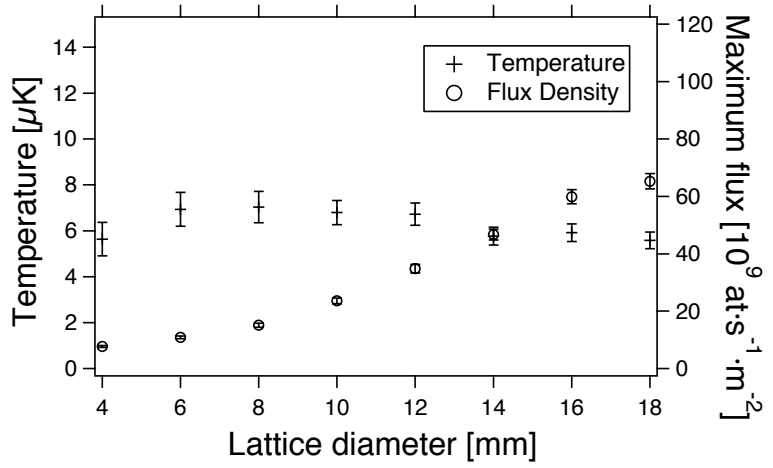


**Figure 5.10**: Maximum atomic flux density and transverse temperature as a function of the diameter of the cooling laser beam. Experimental conditions: D1 pumper laser locked on 44' (power 0.6 mW) and cooling laser frequency locked 20 MHz on the blue side of the 32' transition (power 5 mW). Transverse magnetic field of 70 mG.

**Measurements with the D2 pumper laser**

We have replaced the D1-ECDL with another ECDL that emits on the D2 Cs line. Except this, the optics is unchanged. This time the branching ratio in spontaneous emission is more favorable for a pumper laser locked on 43' rather than 44' hyperfine transition (see Appendix A). With a pumper laser power of 0.1 mW and the cooling laser (power 3.5 mW) locked 20 MHz on the blue side of the 32' atomic resonance we have measured the atomic flux density and the transverse temperature as a function of the applied transverse magnetic field. The result, shown in Fig. 5.11, is a curve symmetric with respect to $\overrightarrow{B}$=0. The atomic flux density has two maxima ($\varphi$=1.8·10$^{11}$ at·s$^{-1}$·m$^{-2}$) corresponding to $\overrightarrow{B}$= ±70 mG and falls down when $\overrightarrow{B}$ decreases toward zero. The transverse temperature, if we neglect the points where the applied magnetic field is almost null, is well fitted by a parabola, in agreement with the theoretical calculations (see Fig. 5.5) and reaches a minimum value of 5 $\mu$K.

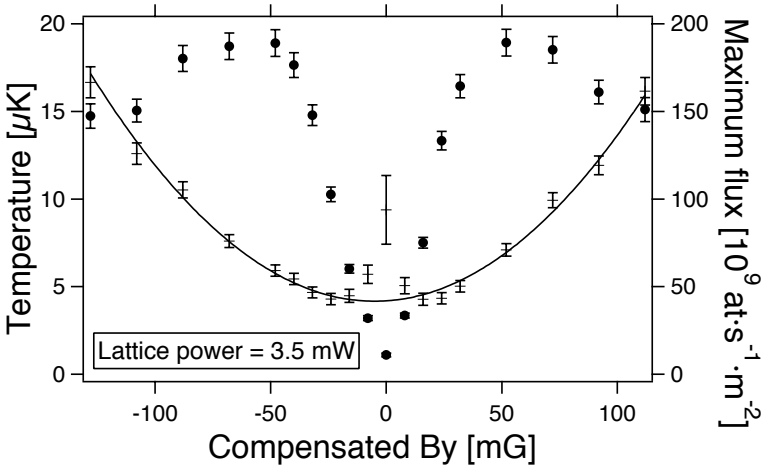


**Figure 5.11**: Transverse temperature (crosses) and maximum atomic flux density (circles) obtained for different values of the applied transverse magnetic field. There is no polarisation gradient of the optical lattice. Note that the cooling mechanism breaks down when $\mathbf{B}_y$=0. Experimental parameters: cooling laser locked 3Γ above the 32' transition, 3.5 mW power; D2 pumper locked on 43', 0.1 mW power. As expected from theoretical predictions, the transverse temperature distribution is well fitted by a parabola.

We have repeated this measurements for several values of the cooling laser power (Figs. 5.12 and 5.13). The shape of the atomic flux *vs* the applied transverse magnetic field is particularly interesting. We remark that the value of the magnetic field that optimises the flux density is a function of the cooling laser power. As a consequence, the width of the dip between the two maxima (let's call it *DeltaB*) increases with the cooling laser power. We have performed a study of the variation of *DeltaB* as a function of this power in a Log-Log scale (Fig. 5.14) to test the cube root dependence found with

theoretical considerations (Eq. 5.4). The distribution of the experimental points is well fitted by a linear fit $y = a + bx$ with $b$=0.35±0.04, value well consistent with the cube root dependence.

The last measurement made has been the search for the cooling laser frequency detuning that optimises the flux density and the transverse temperature (as we already did in the configuration with the D1 pumper laser). In Fig. 5.15 we present the results obtained for three different values of the cooling laser power, namely 2 mW, 4 mW and 8 mW. The more favorable frequency detuning is between 3 and 4 Γ, with a little tendency to increase for higher values of the cooling laser power. We know from the theoretical introduction that for an efficient cooling the transit time of the atoms through the optical lattice must be bigger than the optical pumping time. If the optical pumping rate is too strong, the atoms can be pumped into the ground hyperfine level before they have climbed the potential well until the node, as depicted in Fig. 5.16. The atoms move from the antinode until the top of the potential well in a time $\Delta\, t{=}\lambda/(4v)$, where $v$ is the atoms velocity. The optical pumping rate must be comparable with the inverse of this time:

$$\gamma_p = \frac{s_0 \cdot\ \Gamma/2}{1 + s_0 + (2 \cdot\ \delta/\Gamma)^2} \approx \frac{1}{\Delta\, t} \tag{5.5}$$

For a cooling laser total power of 4 mW ($s_0 \approx$10) and assuming an atom velocity of 10 cm/s we find the optimal frequency detuning $\delta/\Gamma$=3.5, value in good agreement with the experimental result. If now we increase the cooling laser power then the ratio $\delta/\Gamma$ has to be increased in order to satisfy the condition written in Eq. 5.5, confirming the shift of the optimal detuning value.

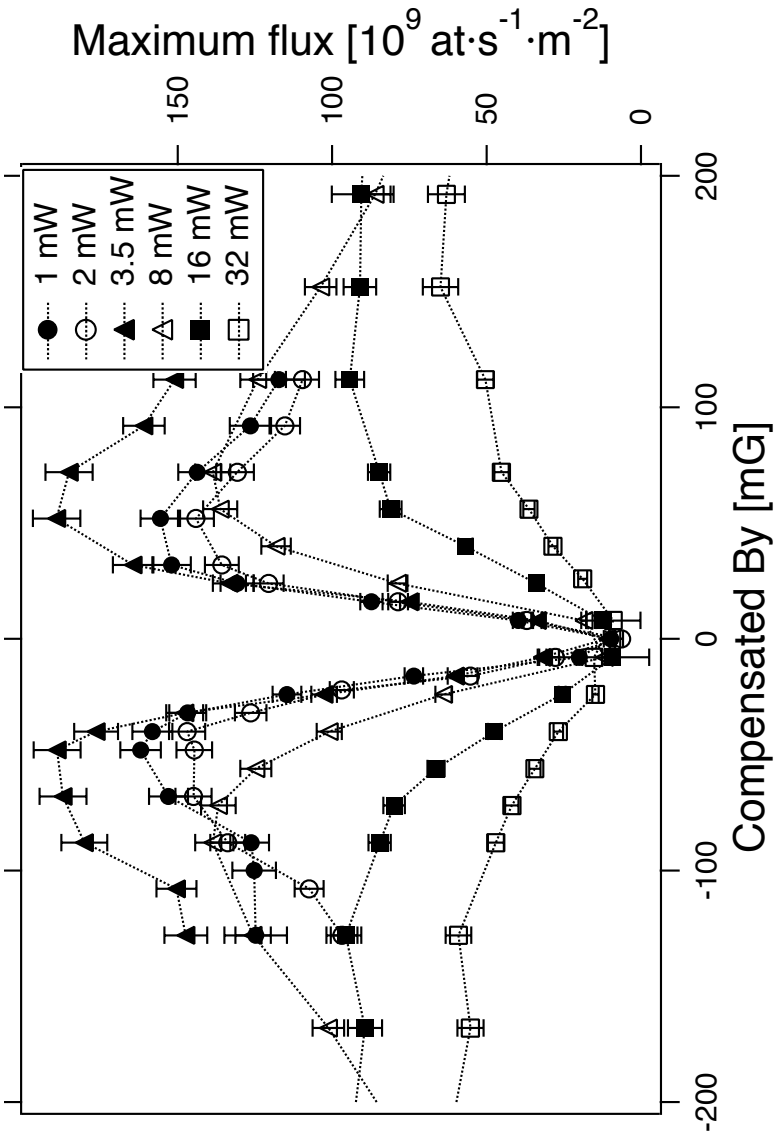


**Figure 5.12**: Atomic flux density variation as a function of the applied transverse magnetic field for different cooling laser power values. Experimental parameters as in Fig. 5.11. Note that the width of the dip depends from the cooling laser power, as explained in the text.

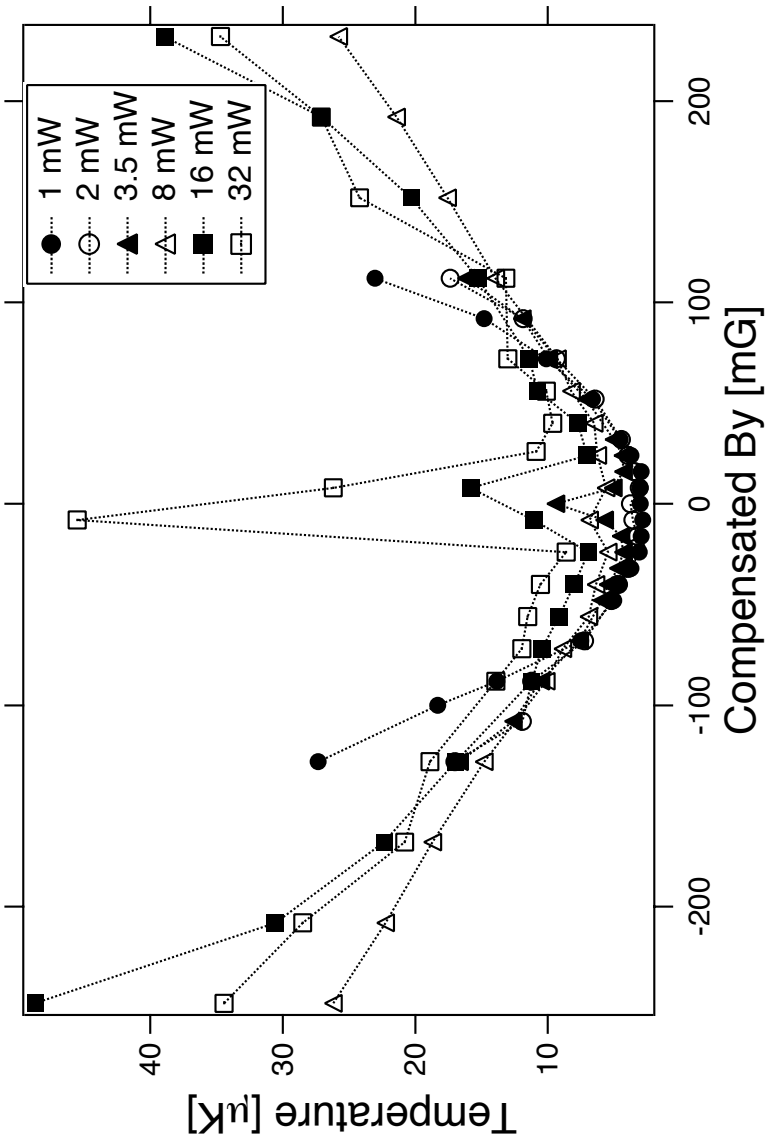


**Figure 5.13**: Transverse temperature variation as a function of the applied transverse magnetic field for different cooling laser power values. Experimental parameters as in Fig. 5.11. Note that the shape of each curve is well fitted by a parabola (more details in the text).

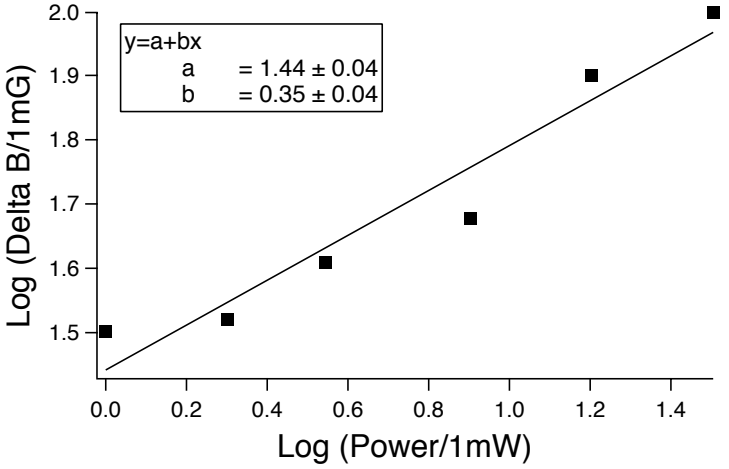


**Figure 5.14**: Graph Log-Log to underline the dependence of the dip width ($DeltaB$) when we plot the flux density vs the transverse magnetic field. The linear fit $y = a + bx$ is compatible with the hypothesis that this width varies as the cube root of the cooling laser power.

### 5.4.2 Cooling on the red side of $F = 4 \Rightarrow F' = 5$.

Before concluding our study of the MILC mechanism we have changed the configuration of the optical lattice, switching to a situation where the cooling laser is tuned to the $F = 4 \Rightarrow F' = 3, 4, 5$ transitions and the D2 pumper laser locked on either $F = 3 \Rightarrow F' = 3$ or $F = 3 \Rightarrow F' = 4$ atomic resonance. In these conditions, we have stored the fluorescence signal due to the atomic flux by scanning the cooling laser frequency over all the D2 line. In Fig. 5.17 one can see that without applying a transverse magnetic field there is no cooling (Fig. 5.17a); with a magnetic field we observe cooling on the red side of the 45' and on the blue side of the 44' transitions (as expected from the theory). The fluorescence signal is higher in the configuration with the pumper laser locked on 34' (Fig. 5.17c) rather than on 33' (Fig. 5.17b), the branching ratio being favorable for the first case (see Appendix A). In fact the fluorescence signal in the red side of the 45' cycling transition is the same for both configurations of the pumper laser, while in the blue side of the 44' open transition we need an efficient pumping and the branching ratio plays an essential role. Note that the cooling mechanisms on the blue of 44' and on the red of 45' work together and the resulting collimation is higher than the one expected from a simple model with a coupled and a non-coupled state. There is no cooling on the blue side of the 43' transition, result surprising because we have observed it in the similar 32' transition. The probable explanation has to be searched once again in the pumping process: for the more efficient

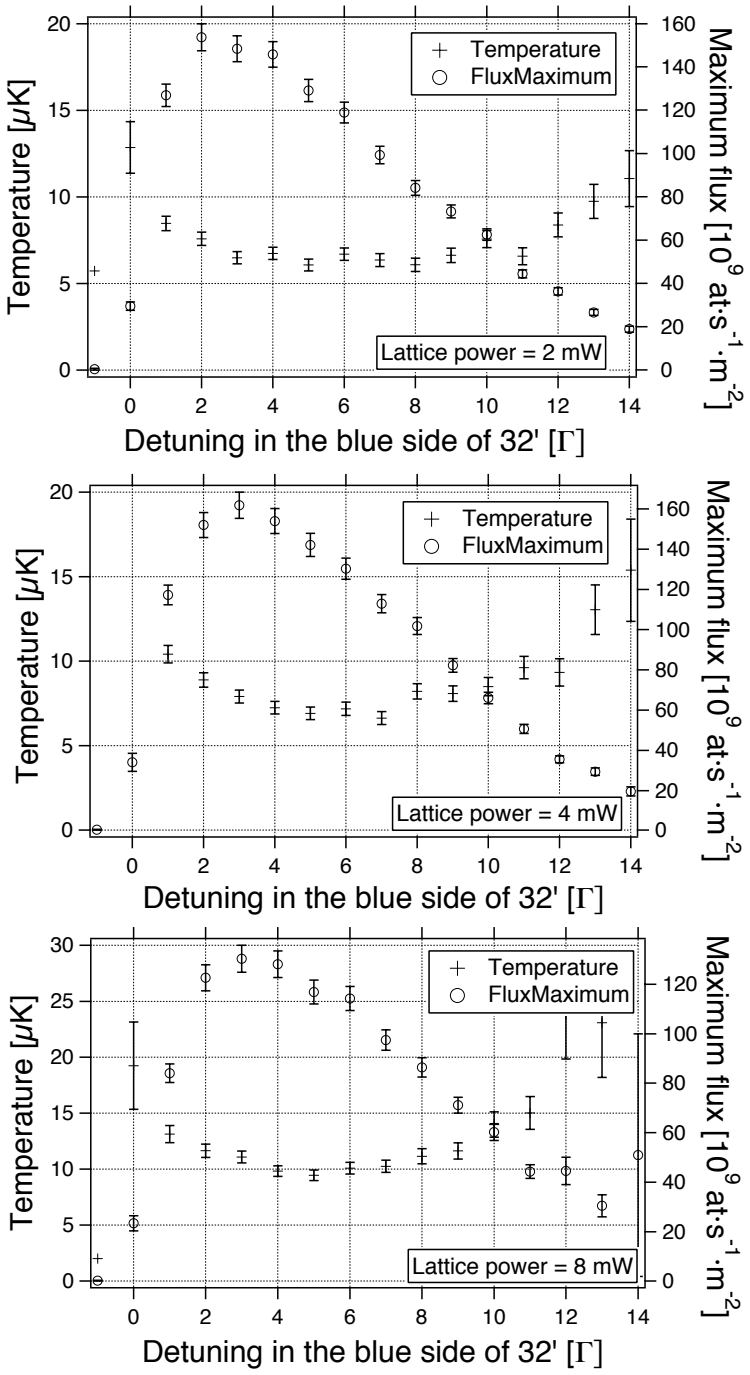


**Figure 5.15**: Transverse temperature and atomic flux density as a function of the frequency detuning of the cooling laser around the atomic transition 32'. The three curves are obtained for different cooling laser powers. Same experimental parameters as in the previous graphs. Note that the frequency detuning that optimise the detected flux increases by increasing the laser power.

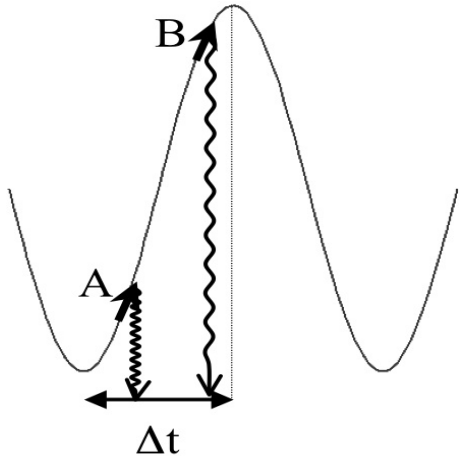


**Figure 5.16**: Relation between optical pumping time and the time required to the atoms to move from the antinode to the node of the potential well. For a too low frequency detuning the pumping rate is more important than this time ($\Delta\ t$) and the atoms are pumped into the ground state level when they are in position A along the potential well instead of reaching the region of the apogee, in B. The cooling process is thus less efficient.

34' pumper laser frequency, atoms are put luckily in $m_F$=0[1], already on the top of the potential hill, and they do not loose potential energy before be optically pumped into the less coupled state $m_F$=4. In the case of the cooling on the 32' transition, the pumper laser was locked on the atomic resonance 44' and the transition probability was enhanced for the Zeeman sub-levels $m_F$=±3, that are the less coupled states in the cooling mechanism. Thus the atoms climb the potential hill and loose potential energy before being optically pumped back into $m_F$=±3. On the other hand in this case the pumper laser is less important, the atomic transition being closed.

Experimental conditions: cooling laser power 10 mW and pumper laser power 0.1 mW.

[1]The quantization axis is along $z$ and the light polarisation is $\pi$ for both the cooling laser and the pumper laser.

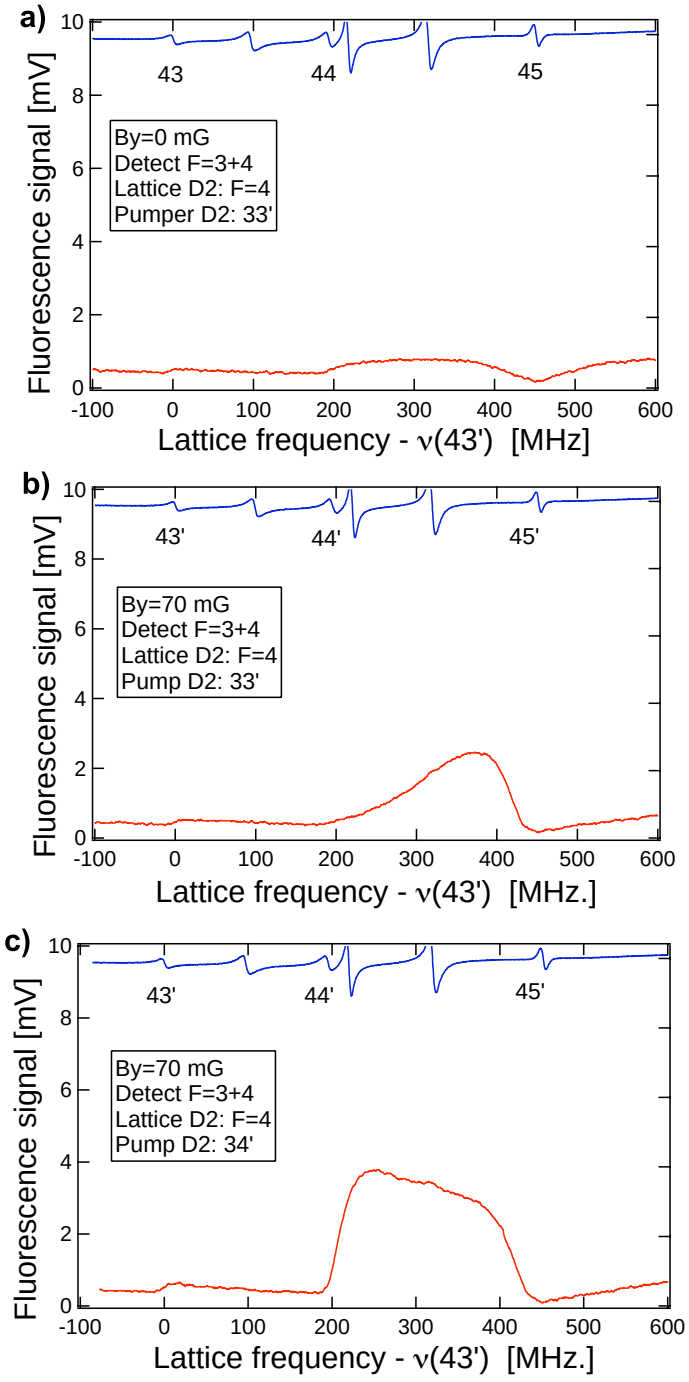


**Figure 5.17**: Cooling laser frequency scan around the atomic transitions $F = 4 \Rightarrow F'$. The cooling laser power is equal to 10 mW. First graph obtained with no magnetic field and the D2 pumper locked on the 33' atomic transition. Second and third graphs obtained with a transverse magnetic field (70 mG) and with the D2 pumper (power 0.1 mW) locked respectively on the 33' and 34' atomic transition. Upper curve in each graphs is the saturated absorption error signal, used as reference.

### 5.4.3 Comparison with gray molasses

The two different cooling mechanisms presented in this chapter and in the previous one give very similar results. The physics itself has strong analogies, with a cooling cycle that works between a coupled state whose potential hill is climbed by the atoms and a non-coupled state where atoms are pumped once they reach the top of the hill. The substantial difference between the two processes is the way to realise the mixing between the non-coupled state and the coupled one. In the gray molasses this is done by the motional coupling due to the polarisation gradient, while in the MILC is the transverse magnetic field that redistributes the atoms among the different Zeeman sub-levels. In Fig. 5.18 we compare, for the two cooling mechanisms, the atomic flux density and the transverse temperature as a function of the applied static magnetic field in identical experimental conditions. Note that the cooling in a gray molasses works better than in the MILC. By using this technique we have reached lower transverse temperatures and higher atomic flux densities.

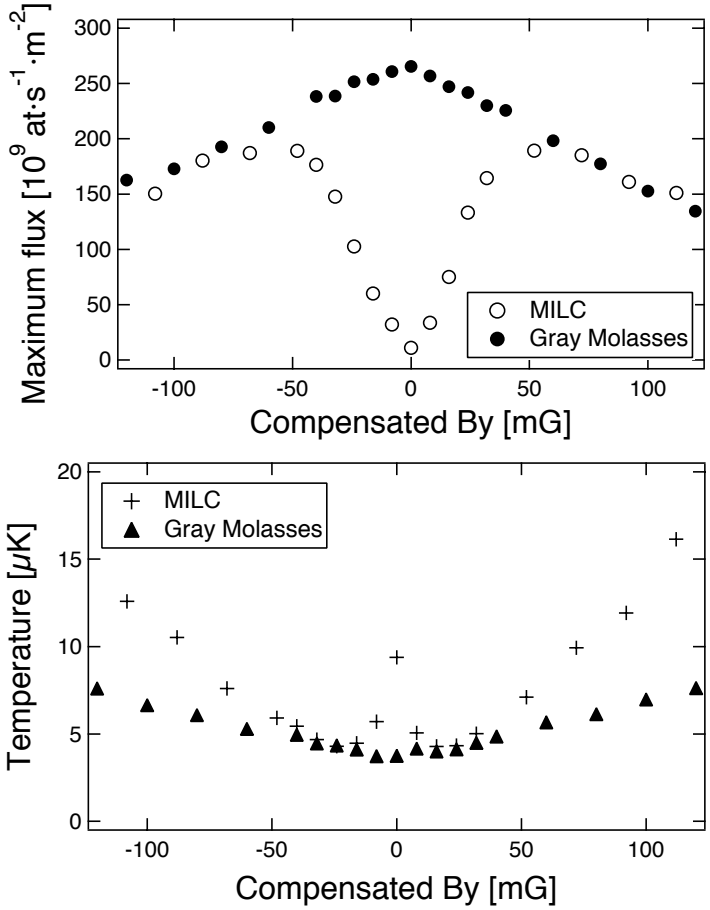


**Figure 5.18**: Comparison between the results obtained with the cooling in a gray molasses and with the MILC. The upper graph shows the measured flux density for the two cooling mechanisms, the lower one the final transverse temperature. For both processes the cooling laser power was of 3.5 mW, the detuning $\delta$=3$\Gamma$ and the pumper laser power of about 0.1 mW.

## 5.5 Conclusion

To summarise the results obtained in this chapter, we can underline the following points:

- We have observed the cooling mechanism due to the Magnetically Induced Laser Cooling (MILC) as expected from the theory on the transitions of the type $F \Rightarrow F' = F - 1$, $F \Rightarrow F' = F$ (for a blue detuning) and $F \Rightarrow F' = F + 1$ (for a red detuning).
- This mechanism can work in the blue side of a transition $F \Rightarrow F' = F$ together with the cooling in the red side of a transition $F \Rightarrow F' = F + 1$.
- The MILC works if we apply a static magnetic field; this characteristic allows one to find the zero-magnetic field point looking for the minimum of the atomic flux.
- Using a D1 pumper laser we have measured the minimum transverse temperature $T$=5 $\mu$K and the maximum flux density $\varphi \sim 0.7 \cdot 10^{11}$ at$\cdot$s$^{-1}\cdot$m$^{-2}$ for a cooling laser power of 5 mW, a detuning of 3$\Gamma$ and an applied magnetic field of 70 mG.
- Switching to a D2 pumper laser we have obtained $T$=5 $\mu$K and $\varphi \sim 1.8 \cdot 10^{11}$ at$\cdot$s$^{-1}\cdot$m$^{-2}$ for a cooling laser power of only 3.5 mW, a detuning of again 3$\Gamma$ and an applied magnetic field of 70 mG along the $y$-axis.

The conclusion is the same as for the gray molasses. The aim of the study of this collimation technique was an improvement of the results obtained by performing the Sisyphus cooling in a two-dimensional phase stable optical lattice. We expected lower transverse temperatures and higher atomic flux, due to the low fluorescence rate. Given the results, we envisage to implement in FOCS2 the Sisyphus cooling technique to perform the atom transverse collimation.

# Chapter 6

# Loading the fountain source with a slow beam

We describe the design and performance of a slow atom source based on a 2D magneto-optical trap (MOT) that uses an innovative simple optical configuration. Metal-coated retro-reflecting prisms replace mirrors and quarter-wave plates so the optical power of the cooling laser beam is recycled. This source has been characterised for three different configurations: with and without transverse magnetic field gradient, and with a pusher beam to obtain a $2D^+$-MOT. The longitudinal velocity is of the order of 25 $m{\cdot}s^{-1}$, with a transverse velocity spread $\leq 1$ $m{\cdot}s^{-1}$, while the typical atomic flux density obtained is up to $1.3{\times}10^{14}$ $at{\cdot}s^{-1}{\cdot}m^{-2}$ for a cesium vapour pressure of $\sim 4{\times}10^{-8}$ mbar in the source. We use this slow atom beam, instead of cesium vapour, to load a 3D moving optical molasses that feeds a continuous cold atom fountain. We obtain a gain of a factor $\sim 20$ in the atomic flux launched by the fountain. Part of the work presented here is also discussed in Ref. [31].

## 6.1 Introduction

Slow atomic beam sources represent a useful tool for many applications: atom interferometers [1], [32, 33, 34, 35], tests of fundamental symmetries [36], [37], atomic clocks [3], [4], [38], Bose-Einstein condensation [2] and atomic and molecular spectroscopy [39]. In the case of atomic clocks, continuous fountains [9] have the advantage of a lower atomic density for a given signal-to-noise ratio than their pulsed counterparts, which helps minimise density related frequency shifts [4]. Furthermore, the use of such a fountain enables one to eliminate the intermodulation (*a.k.a.* Dick) effect associated with local oscillator noise [7]. In order to take full advantage of the continuous fountain approach however, we need to increase the useful flux. One way is to launch more atoms to begin with. This can be achieved by loading the moving optical molasses source from a slow beam rather than by capture

from the low-velocity tail of a thermal vapour.

Slow beam sources can be produced in various ways [17, 40, 41, 42, 43, 44]. Zeeman slowing of an atomic beam [41] allows a continuous source but is somewhat cumbersome and requires strong magnetic fields, while chirp slowing [45] provides only packets of atoms. Slow beams with low longitudinal velocity can be obtained by drilling a hole in one of the mirrors in a 3D-magneto-optical trap (3D-MOT) [46, 47] or in a pyramidal trap [40, 42]. In [48] the authors slow a thermal beam by using a counter-propagating laser beam and trap the atoms in a 3D-optical molasses superimposed to a 2D-magnetic field gradient. These techniques require a laser beam to be superimposed with the atomic beam. Slow beams can also be extracted from a static 3D-optical molasses superimposed to a 2D-magnetic field gradient using a static magnetic field along the beam axis [49]. Here we report on a much simpler solution, namely the development and characterization of a 2D magneto-optical trap (MOT) of cesium atoms producing a continuous low velocity beam ($v \simeq$ 25 m/s). While 2D MOT's have already been employed [35, 46, 49, 50, 51, 52], the devices in question are usually somewhat expensive, requiring many large ($\sim 30$ mm) polarising beam splitter cubes, quarter- and half-wave plates, all of which are anti-reflection coated. Furthermore, the laser power is divided at each stage so several hundred milliwatts are often necessary at the input. In our own version, gold-coated prisms replace mirrors and quarter-wave plates and the optical power ($< 200$ mW) is recycled. The net result is a considerable saving both in complexity and financial cost without degrading performance as regards the useful flux extracted from the source.

In this chapter we describe the characterisation of the slow beam (longitudinal and transverse velocity distribution, spatial profile) and the optimisation of various parameters (laser power and polarisation, magnetic field gradient henceforth $\nabla$B, laser detuning, cesium vapour pressure). We compare the results obtained with a magnetic gradient (2D-MOT), without one, *i.e.* the so-called 2D optical molasses (2D-OM), and in a third configuration where a pusher laser co-propagates with the atomic beam ($2D^+$-MOT).
The chapter is organised as follows. Section 6.2 is a short memorandum of the trapping mechanism in a MOT. Section 6.3 describes the experimental set-up. In Section 6.4 we describe the method used to calibrate the atomic flux density. In Section 6.5 we present the measurement techniques and diagnostics of the atomic beam emerging both from the 2D-MOT and 2D-OM configurations. A comparison with other beam sources is given in Sec. 6.6. In Section 6.7 we compare the capture efficiency in a 3D static optical molasses fed by the slow atomic beam with that obtained using thermal vapour loading. In Section 6.8 we treat the situation where the atomic beam captured in the molasses is launched vertically. We analyse the upward flux from the optical molasses loaded from the 2D-MOT and $2D^+$-MOT beam sources and

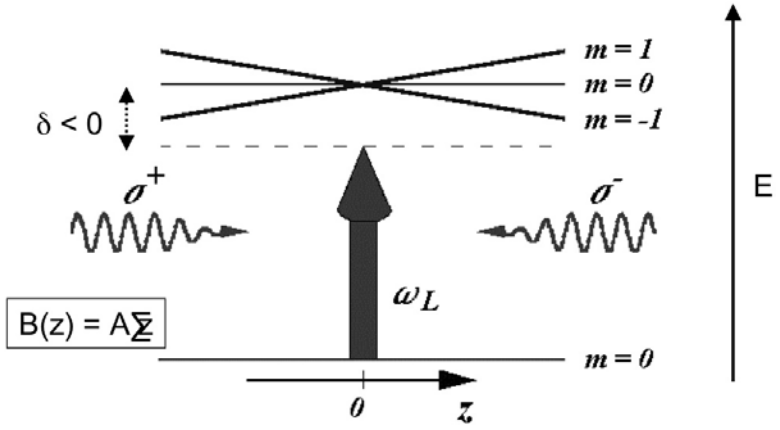


**Figure 6.1**: Mechanism of a magneto-optical trap in a simplified model $J_g = 0 \rightarrow J_e = 1$. The applied magnetic field induces the Zeeman splitting of the atomic sub-levels. Two counter-propagating laser beams red-detuned with respect to the atomic resonance frequency and circularly polarised illuminate the atoms. The selection rules for transitions between the Zeeman sub-levels lead to an imbalance in the radiative force that pushes the atoms towards the centre of the trap. $\delta$ is the frequency detuning, $\omega_L$ the laser frequency, $m$ indicates the Zeeman sub-levels and $\sigma^{\pm}$ the laser light polarisation.

compare results with thermal vapour loading. This study is important for evaluating the potential improvement in stability achievable for an atomic fountain clock [9] using such a pre-source.

## 6.2 Physics of the Magneto-Optical Traps

Optical and magnetic fields can be combined together to accumulate the atoms in a magneto-optical trap. The principal idea of these devices was suggested by J. Dalibard and demonstrated at Bell Laboratories (USA) in collaboration with a group from MIT. The trapping mechanism is illustrated in Fig. 6.1 for a simple one-dimensional scheme $J_g = 0 \rightarrow J_e = 1$. The atoms move in a linearly inhomogeneous magnetic field whose map is a magnetic quadrupole field. Zeeman splitting of the hyperfine sub-levels is induced with an orientation given by the sign of the magnetic field: positive in the right hand side of Fig. 6.1, where the magnetic field is positive, and negative in the left hand side.

Two counter-propagating laser beams of opposite circular polarised light $\sigma^+$ and $\sigma^-$ and red-detuned with respect to the resonance frequency $\omega_0$ induce optical pumping of the atoms. The $\sigma^+$ polarised beam moves in the positive $z$-direction, $\sigma^-$ propagates itself in the opposite direction. Due to the red-detuning and to the Zeeman splitting, the atoms in the positive region of the magnetic field ($z>0$) absorb with a stronger probability the $\sigma^-$ component of the light field, and viceversa for $z<0$ where the $\sigma^+$ is enhanced

in the absorption process. The result is an imbalance in the radiative force that pushes the atoms towards the centre of the trap, where the magnetic field is null. To describe mathematically the magneto-optical trap we can incorporate the frequency shift caused by the Zeeman effect into the expression of the radiative force:

$$F_{\pm} = \pm \frac{\hbar\ k\Gamma}{2} \cdot \frac{s_0}{1 + s_0 + (2\delta_{\pm}/\Gamma)^2} \tag{6.1}$$

where $F_+$ is the force induced by the $\sigma^+$ light component and $F_-$ the one due to the absorption of the $\sigma^-$ light component. The total force acting on an atom is given by $F = F_+ + F_-$. $s_0$ is the saturation parameter and the detuning $\delta_{\pm}$ is equal to

$$\delta_{\pm} = \delta \mp\ k \cdot\ v \pm \mu' B/\hbar \tag{6.2}$$

here $\mu' \equiv (g_e m_e - g_g m_g)\mu_B$ is the effective magnetic moment for the transition considered, $\mu_B$ being the Bohr magneton. $\delta$ is the frequency detuning $(\omega_L - \omega_0)$, $v$ the atom velocity and $k$ the wave vector. For small Zeeman and Doppler shift compared to the frequency detuning we can expand the denominator of the force obtaining the well known expression:

$$F = -\beta\ v - \xi\ z \tag{6.3}$$

where we have taken into account that $\mathbf{B}$=B($\mathbf{z}$) $\equiv\ Az$. In the expression above $\beta$ is the damping coefficient and $\xi$ the spring constant

$$\beta = \frac{8\hbar\ k^2\delta\ s_0}{\Gamma(1 + s_0 + (2\delta\Gamma)^2)^2} \tag{6.4}$$

$$\xi = \frac{\mu'\ A}{\hbar\ k}\beta \tag{6.5}$$

The force of Eq. 6.3 leads to damped harmonic motion of the atoms, where the damping rate is given by $\Gamma_{MOT} = \beta/M$ and the oscillation frequency is $\omega_{MOT} = \sqrt{\xi/M}$; in the two previous expressions $M$ is the atom mass. A complete analysis of the magneto-optical traps physics can be found in Refs. [2, 53].

## 6.3 Experimental set-up

An overview of the set-up is given in Fig. 6.2. The 2D-MOT pre-source to be described in Sec. 6.3.1 provides a slow atomic beam directed towards a 3D-optical molasses region (described in Sec. 6.3.2) where it is captured and then launched vertically in a cold atom fountain. We define two coordinate

systems, {*x,y,z*} and {*x',y',z'*} related to the laboratory and to the pre-source respectively. $x$ and $y$ represent the horizontal plane and $z$ the vertical launch direction of the fountain. $z'$ designates the cell axis, inclined at 45 ° to the vertical, and $x'$ and $y'=y$ lie in the transverse plane. All laser beams are transmitted from the same optical table (see Fig. 6.3) to the slow atom beam apparatus through polarisation-maintaining optical fibres. Collimators at the fibre exits allow adjustment of beam diameters.

### 6.3.1 Pre-source

A scheme of the pre-source is represented in Fig. 6.4.

The glass cell (internal dimensions 30 mm × 30 mm × 150 mm) is connected to a UHV chamber via a titanium adaptor flange of internal diameter 16 mm that widens to 40 mm towards the vacuum chamber. The former diameter constitutes the smallest constriction between the pre-source and the 3D-OM region (Fig. 6.2), centre of the UHV chamber 500 mm downstream. Cs is injected directly into the pre-source cell. An adjustable bellows allows angular adjustment of cell axis while a gate valve enables one to isolate the pre-source from the vacuum system if necessary. Fig. 6.6 shows the scheme of the mechanical connections between the pre-source and the UHV chamber.

The required $\nabla$B is generated by four identical rectangular coils wired in series, fixed to a chassis that surrounds the pre-source. The resulting magnetic field map has a quadrupole distribution in the transverse $x'y'$ plane with a zero field line lying along $z'$ (see Fig. 6.5). A high thermal conductivity silicone gum ensures efficient dissipation of Joule heat from the coils to the chassis. In fact under the optimal operating conditions there is a negligible temperature rise.

The cooling laser beam has a diameter of 30 mm and a total power up to 200 mW, divided by a polarising beam splitter (PBS) to supply both the $x'$ and $y'$ cooling directions, as shown in Fig. 6.2. A half-wave plate situated before the PBS is used to balance the light intensity of the two orthogonal beams, while two quarter-wave plates at the entrance of the glass cell provide the required circular polarisation. The laser ((4) in Fig. 6.3) is a home-made Extended Cavity Diode Laser (ECDL) centred on 852 nm (cesium D2 line) and injected into a Master Oscillator Power Amplifier (MOPA); it is red detuned from the transition $6S_{1/2}, F = 4 \rightarrow 6P_{3/2}, F' = 5$ by typically 1.5Γ. This detuning, adjusted using the Zeeman effect in a saturation spectroscopy Cs vapour cell [55], is monitored continuously using the beat between this laser frequency and the frequency of the 3D-molasses laser (described in Subsec. 6.3.2). A pumper laser beam (an ECDL, (5) in Fig. 6.3), overlapped with the cooling beam and locked to $6S_{1/2}, F = 3 \rightarrow 6P_{3/2}, F' = 4$, recovers the atoms pumped into $F = 3$. It has a power of 1.5 mW and the same dimensions as the cooling beam, both being transmitted through the same

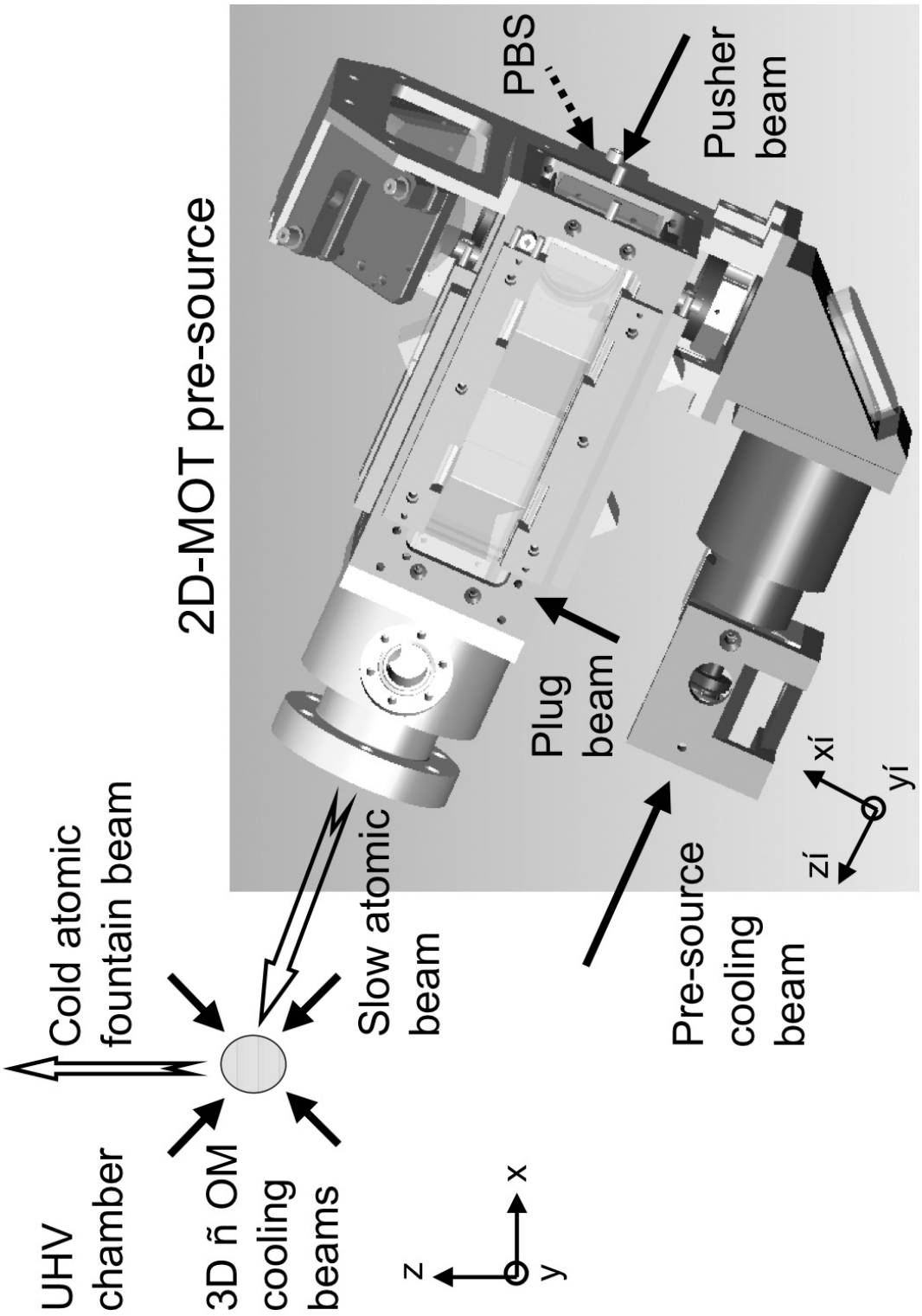


**Figure 6.2**: Pre-source in an overview of the experimental set-up. The cooling beam is split into two parts by a polarising beam splitter (PBS). Each then propagates along the glass cell, glued to a titanium flange, itself connected to the UHV chamber.

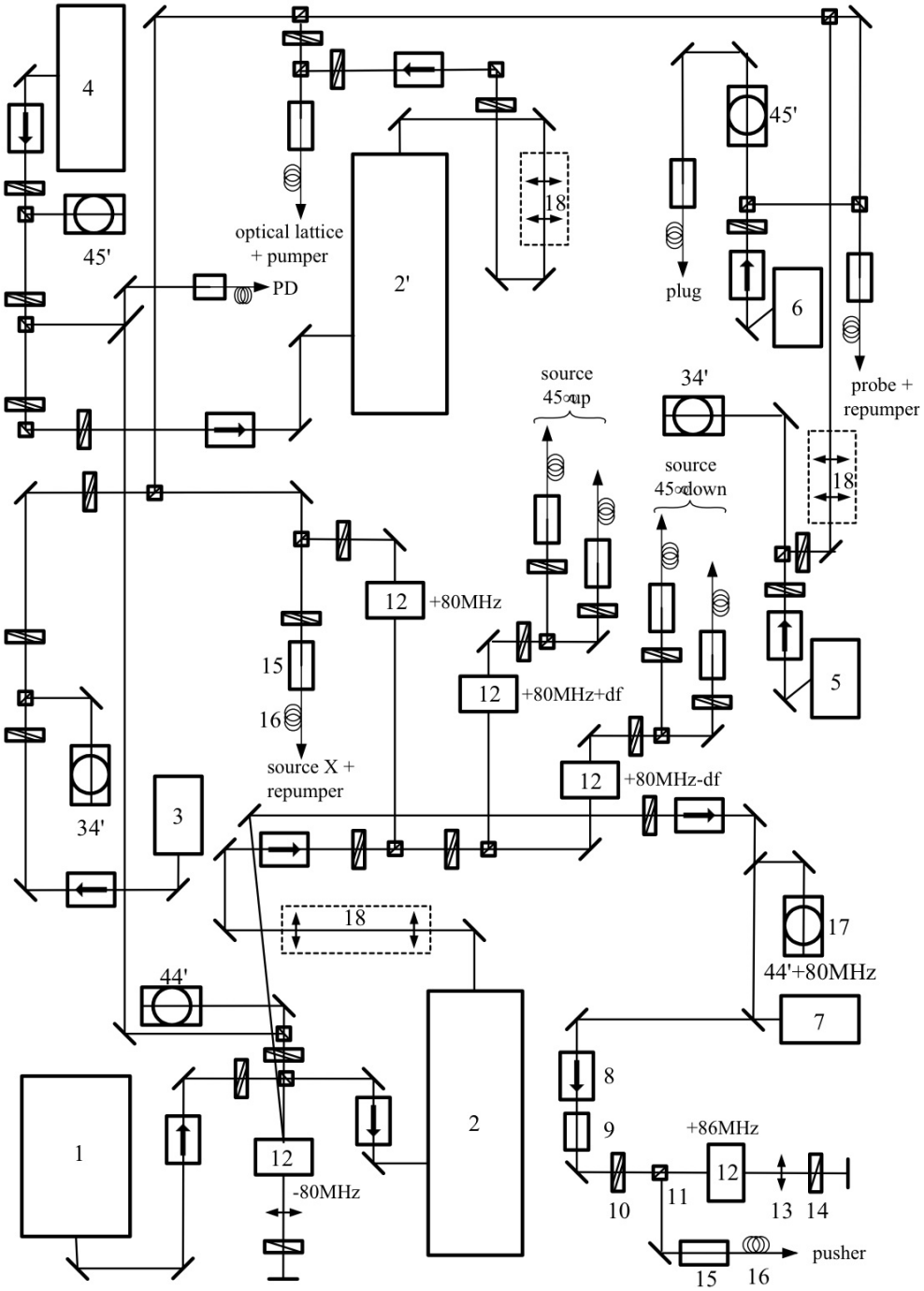


**Figure 6.3**: Optical table scheme. 1: master laser (ECDL); 2: optical amplifier (MOPA); 3: repumper laser (DBR); 4: cooling laser (ECDL); 5: pumper laser (ECDL); 6: probe laser (ECDL); 7: push laser (Diode injectée); 8: optical isolator; 9: astigmatic compensation prisms; 10: half-wave plates; 11: polariser beam splitter; 12: acoustic-optics modulator; 13: achromatic lenses; 14: quarter-wave plates; 15: optical fibres coupling; 16: polarisation maintaining optical fibres; 17: saturated absorption Cs cells; 18: telescope; PD: fast photo-detector for beat.

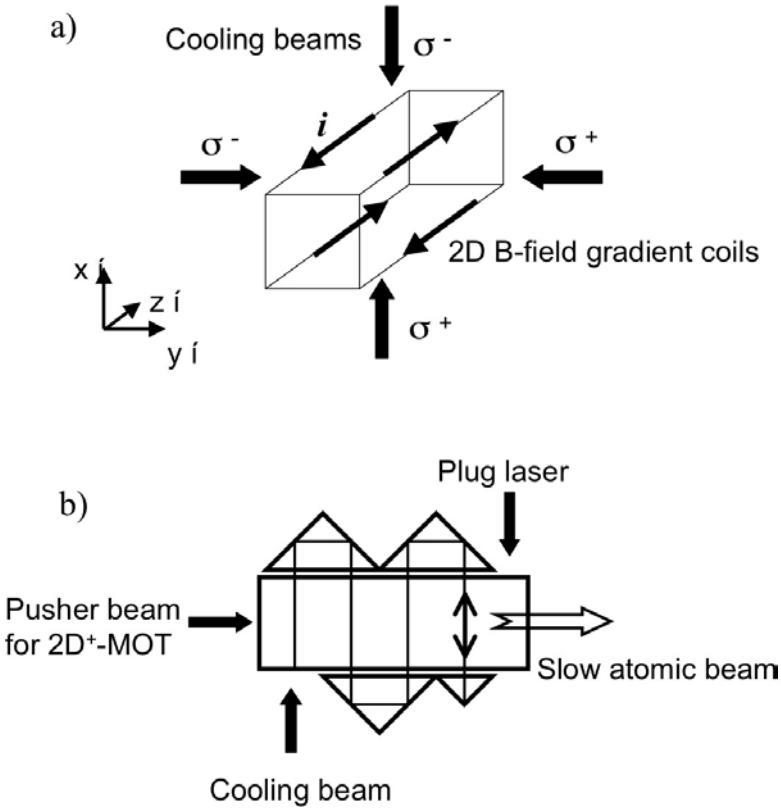


**Figure 6.4**: Scheme of our pre-source: a) The four perpendicular cooling beams and the coils that generate the transverse magnetic field gradient. b) Beam geometry (for clarity only one of the two cooling directions is represented), see Sec. 6.3.1 for details.

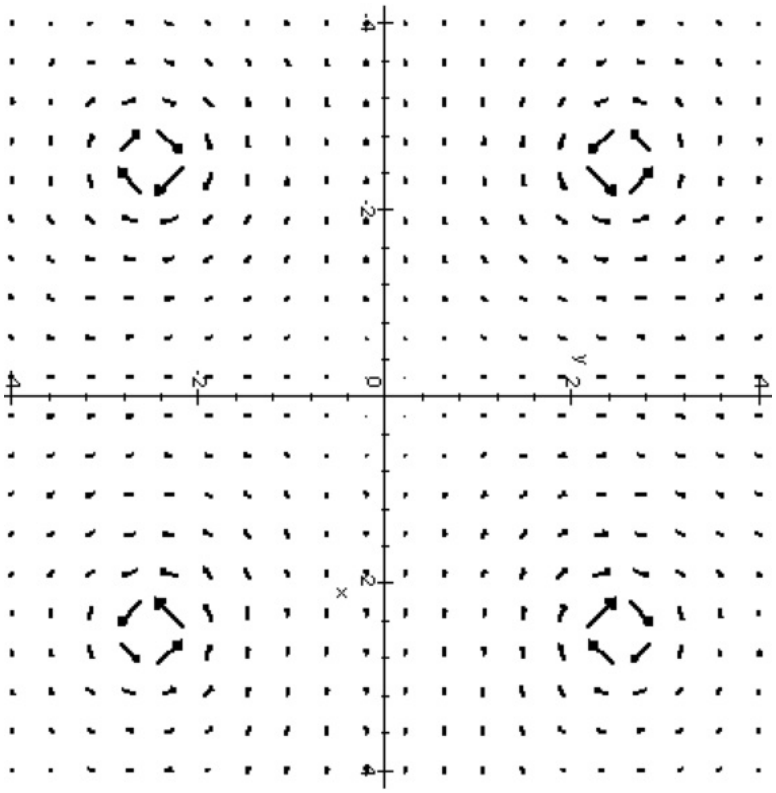


**Figure 6.5**: Magnetic field map in the plane *x'y'* obtained when a current passes through the four rectangular coils described in the text. The plot is the result of a theoretical modelisation presented in Ref. [54] that well fits with the experimental measurements of the magnetic field gradient inside the pre-source. The dimensions are expressed in centimeters.

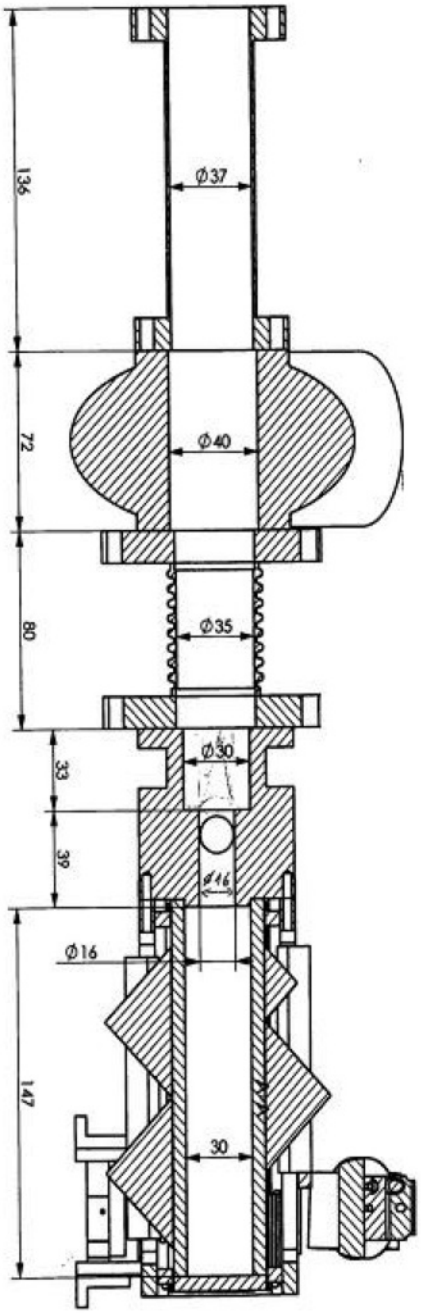


**Figure 6.6**: Scheme of the mechanical connections between the pre-source and the experimental fountain. The dimensions are expressed in millimeters.

optical fibre and expanded after passage through the collimator described in Fig. 6.7. Such choice of the lenses minimises the spherical aberration and guarantees a diameter of the output beam of 30 mm[1]. Fig. 6.8 shows the hyperfine transitions used.

The cooling beam and the pumper cover the volume of the cuvette by total internal reflection from a series of gold-coated right-angle optical prisms, see Fig. 6.4b. When the beam arrives on the first prism, 42.4 mm × 42.4 mm × 30.0 mm in dimensions, it is reflected successively from one perpendicular sloping face to the next before crossing the glass cell again, shifted by 30 mm and with opposite circular polarisation with respect to the previous passage. It is subsequently reflected by a second prism then a third, arriving finally on the fourth. The dimensions of the latter are 21.2 mm × 21.2 mm × 30 mm, so the laser beam covers all its surface; here it is doubly reflected but not translated and so retraces its steps. The gold coating on the two catheti of the prisms preserves the purely $\sigma^+ - \sigma^-$ polarisation. A film of index matching fluid (glycerine) between the cuvette and the prisms helps minimize reflection losses at the air-glass interfaces (reduced from 4% to a negligible level) and an AR coating reduces losses at the internal faces of the cuvette. While we still measured a loss of 4% for each reflection on the gold surfaces due to the absorption, this would be reduced if we used silver-coated prisms instead [2]. Added to the cesium absorption inside the cell, these losses create an imbalance of the cooling beam intensity that might be detrimental to pre-source performance. The smallest prism was placed nearest the cell exit to minimise this effect. Due to this effect it is well probable that the effective length of the pre-source is smaller than the actual one.
The optical set-up of the pre-source is completed by another couple of laser beams, both shown in Fig. 6.4: a plug (part of laser (6)) and a pusher (laser (7) in Fig. 6.3). The plug beam (power 3 mW) tuned to $F = 4 \rightarrow F' = 5$ transition allows one to measure the longitudinal velocity distribution (see Sec. 6.5.4). The pusher beam (power up to 2 mW, typical diameter 20 mm) is used to make a $2D^+$-MOT configuration; it is tuned independently near resonance with the $F = 4 \rightarrow F' = 5$ transition.

### 6.3.2 Optical molasses and detection

The collimated atomic beam exiting from the pre-source reaches the centre of the UHV chamber 500 mm downstream where we perform diagnostics using another ECDL beam ((6) in Fig. 6.3) that crosses the atomic beam

[1]More details about the compensation of the spherical aberration in an optical system can be found on the catalogue Melles Griot, section *Fundamental Optics*.

[2]C.W. Goodwin, private communication. Calculations for a 45 ° angle of incidence and $\lambda = 852$ nm give $R_P = 96.66\%$ and $R_S = 97.45\%$ for Au and $R_P = 98.45\%$ and $R_S = 99.21\%$ for Ag.

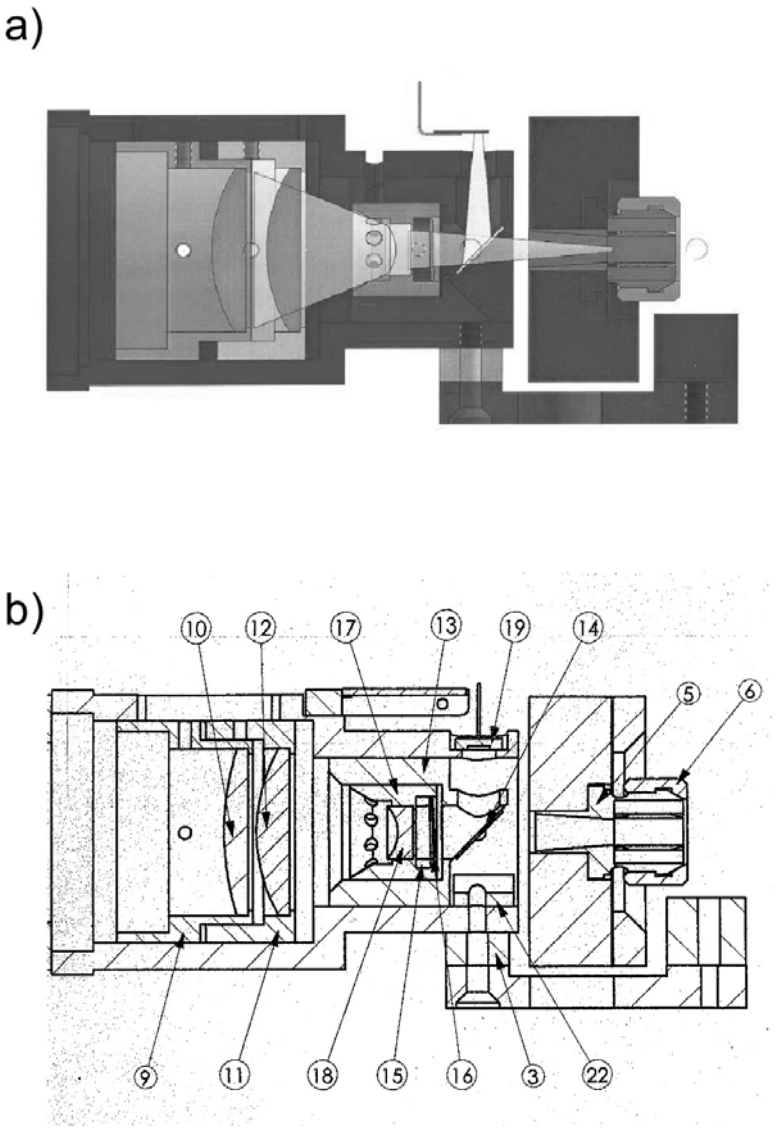


**Figure 6.7**: Collimator used to expand the cooling laser beam exiting from the optical fibre. a) View of the ensemble of the collimator. b) Detailed description of the collimator components. The numbering is not complete because we have omitted for clarity part of the technical draw. 3: spacer; 5: fibre coupling; 6: washer; 9: tube for the convex lens $L_1$; 10: convex lens $L_1$, focal length $f_1$=100 mm, ∅=31.5 mm; 11: mounting for the convex lens $L_2$; 12: convex lens $L_2$, focal length $f_2$=60 mm, ∅=31.5 mm; 13: mounting for optical components; 14: plate to deflect partially the laser light on the photodiode; 15: mounting for the plate; 16: quarter-wave plate, ∅=13 mm; 17: tube for the system quarter-wave plate+plate; 18: concave lens $L_3$, focal length $f_3$=-10 mm, ∅=10 mm; 19: photodiode to measure the laser light retro-reflected after passage through the 2D-MOT; 22: light trap in graphite.

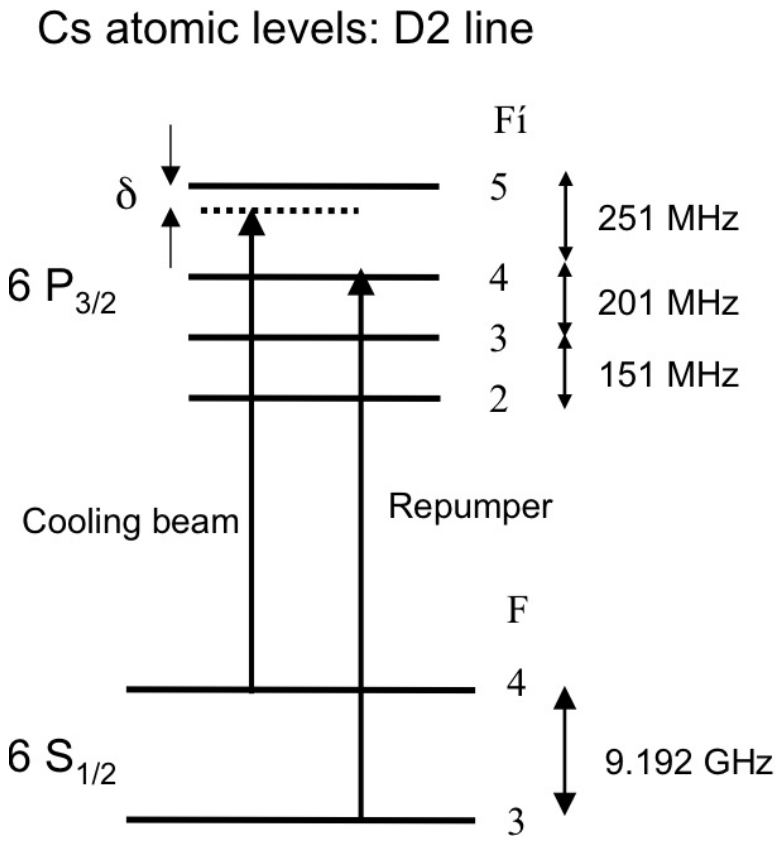


**Figure 6.8**: Hyperfine transitions of the $^{133}$Cs D2 line (852 nm) used for the pre-source and diagnosis. The cooling beam is red detuned with respect to the $F = 4 \rightarrow F' = 5$ transition by $\delta$, typically -8 MHz.

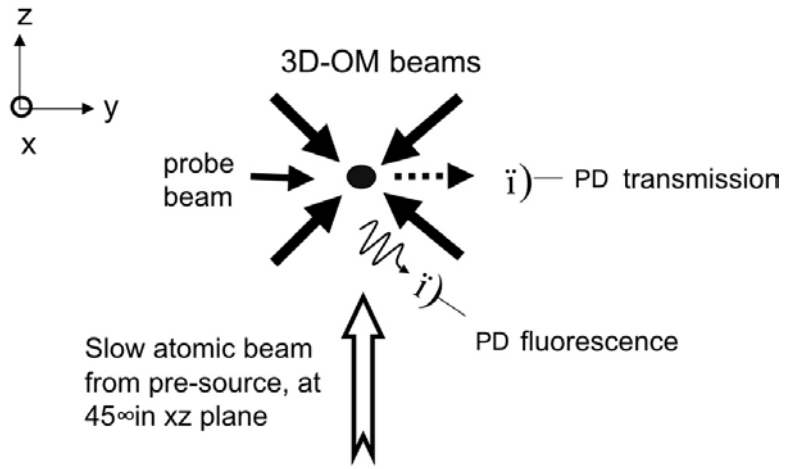


**Figure 6.9**: Scheme of the 3D static optical molasses region. Six counter-propagating laser beams (the horizontal retro-reflected beam along $x$ not shown) with opposite circular polarisation capture the cesium atoms travelling through the intersection region. Two photodetectors (PD) allow simultaneous monitoring of the fluorescence and transmission signals induced by the probe beam.

transversely along the $y$ direction. This probe laser, scanned over the $F = 4 \rightarrow F' = 5$ transition, has a power up to 2 mW and a gaussian beam waist radius of 2.8 mm. We select an output diameter of 5 mm using a diaphragm. A weak repumper laser beam (0.2 mW from a Distributed Bragg Reflector diode laser, DBR, (3)) stabilised on the $F = 3 \rightarrow F' = 4$ transition is overlapped with the probe laser in order to recycle atoms inevitably pumped into the $F = 3$ level. Two photodetectors, one opposite the probe laser and the second in the same plane but oriented along the $x$ direction, allow simultaneous detection of the transmission and fluorescence signals (see Fig. 6.9).

In this region we can switch on a 3D optical molasses (3D-OM) to capture the atomic beam. This is formed by six counterpropagating beams (see Fig. 6.9), red detuned by 12 MHz from the $F = 4 \rightarrow F' = 5$ transition and circularly polarised (each pair of counterpropagating beams has opposite $\sigma^+ - \sigma^-$ polarisation). The horizontal retro-reflected beam ($x$-axis) is overlapped with a weak repumper beam (power 0.1 mW, small component of laser (3)). The central frequency of the upward and downward pairs of beams can be modified independently using different Acoustic-Optical Modulators (AOMs) to produce either a static or a continuous moving optical molasses [17]. The beams originate from a common laser (henceforth the 3D-molasses laser, (1)), an ECDL offset-locked by 160 MHz above the $F = 4 \rightarrow F' = 4$ transition and amplified by injection into a MOPA. The output of the MOPA passes through an AOM centered on 80 MHz to produce the desired cooling frequency. The power per beam is 7 mW and the waist radius 13 mm.

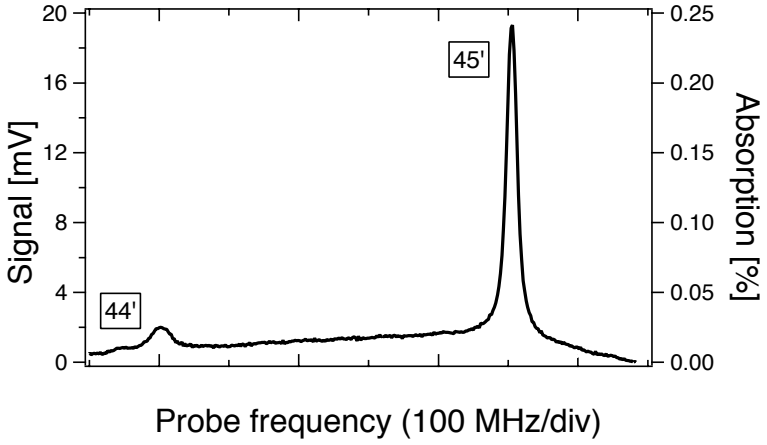


**Figure 6.10**: Probe absorption by the slow atomic beam for low intensity light (total power 0.15 mW, diameter 5 mm) near the atomic resonances $F = 4 \rightarrow F' = 4$ and $F = 4 \rightarrow F' = 5$ without repumper. Here, the pre-source is a 2D-MOT with a cesium pressure of $\simeq 4{\times}10^{-8}$ mbar.

## 6.4 Flux calibration

We have calibrated the atomic flux using probe absorption without repumper rather than fluorescence signals to be independent of light collection efficiency. We exploit the two $F = 4 \rightarrow F' = 4$ and $F = 4 \rightarrow F' = 5$ atomic resonances. Strictly we detect only atoms present in the $F = 4$ ground hyperfine level. On the former *open* transition, absorption is limited by the hyperfine pumping time with an *absolute* value independent of probe beam intensity and size. The power subtracted from the beam yields directly the atomic flux. This method, illustrated in Sec. 6.4.1, is the most reliable but gives small signals. For this reason, we also use the $F = 4 \rightarrow F' = 5$ transition as a transfer standard since it provides better S/N. On this *closed* (cycling) transition the absorption is limited by the transit time and the *relative* absorption gives access to the atomic density. We have also exploited it to cross-check the 44' calibration (Sec. 6.4.2).

### 6.4.1 Absorption on the $F = 4 \rightarrow F' = 4$ component (pumping transition)

Atoms excited by the probe beam to the $6P_{3/2}, F' = 4$ level undergo spontaneous emission that puts them in either the $F = 3$ or $F = 4$ ground state, with a probability given by the branching ratio (see Appendix A). Since there is no repumper, 12/5 photons on average are emitted per atom before it is pumped into $F = 3$ and lost. This rate is obtained by the geometrical series

$$n_{ph} = \left(\frac{5}{12}\right) \cdot \sum_{k=1}^{\infty} k \cdot \left(\frac{7}{12}\right)^{k-1} \tag{6.6}$$

that gives the probability for an atom to be pumped into $F = 3$ after $k$ cycles[3]. The corresponding emitted power equals the absorbed probe power. From the absolute amplitude of the absorption peak $S_{abs}$ one can deduce this power $P$, given the photodetector transimpedance $R_f$ and quantum efficiency $\eta_{PD}$, and the transmission of the detection optics $\eta_{Op}$. This power divided by the energy removed per atom yields the atomic flux traversing the probe beam and thereby the atomic flux density

$$\varphi = \frac{S_{abs}}{R_f \ \eta_{PD} \ \eta_{Op} \ (12/5 \ h\nu) \ \Sigma_{det}} \tag{6.7}$$

where $\Sigma_{det}$ = probe diameter $\times$ the transverse size of the atomic beam is the detection area. With $S_{abs}$=1 (0.3) mV (see Fig. 6.10), $R_f$=1 MΩ, $\eta_{PD}$=0.5 A/W, $\eta_{Op}$=0.5 and $\Sigma_{det}$=5×10 mm$^2$ (*i.e.* the transverse beam profile $\times$ the probe beam diameter), we obtain

$$\varphi_{44'} = 1.5 \ (0.5) \times 10^{14} \ \text{at}\cdot\text{s}^{-1}\cdot\text{m}^{-2}. \tag{6.8}$$

The uncertainty here is mainly statistical.

### 6.4.2 Absorption on the $F = 4 \rightarrow F' = 5$ component (cycling transition)

In the limit of negligible optical saturation and negligible off-resonant hyperfine pumping, the resonant probe *relative* absorption $\Delta I/I$ by the atomic beam of column length $\Delta y$ gives the atomic density $n$ (using for instance Ref. [2]). Multiplying by the mean longitudinal velocity $v$, one obtains the flux density :

$$\varphi \ = \ n \ v = -\frac{27}{11} \ \frac{\Delta I}{I} \ \frac{1}{\sigma} \ \frac{v}{\Delta y}. \tag{6.9}$$

Here $\sigma = 3\lambda^2/2 \ \pi$ is the resonant cross section and 11/27 the relative oscillator strength for the $F = 4 \rightarrow F' = 5$ transition, see Appendix A. For $\Delta I/I$=0.23% (Fig. 6.10), $v$=25 m·s$^{-1}$, $\Delta y$=10 mm (atomic beam transverse size), we obtain

[3]Here we make the hypothesis that all the atoms have had the time to be pumped into $F = 3$. To satisfy this hypothesis the pumping time must be smaller than the transit time through the probe laser beam. Thus, there is a low limit $I_{min}$ for the probe laser beam intensity that has to be respected. Considering that $t_{transit}$=0.28 ms and the probe laser total power is 0.150 mW with a beam diameter of 5 mm, the condition is widely fulfilled: $I_{probe}$=0.6 mW/cm$^2$ $\gg$ $I_{min}$=1.1· 10$^{-3}$ mW/cm$^2$

$$\varphi_{45'} = 0.5 \times 10^{14} \text{ at}\cdot\text{s}^{-1}\cdot\text{m}^{-2}. \quad (6.10)$$

The difference between the results of the two calibration methods we attribute to the difficulty of estimating all the uncertainties in the factors involved in the 45' calibration (*e.g.* Zeeman pumping, optical saturation, beam geometry, velocity spread, *etc.*). We consider the 44' calibration to be more reliable and thus place a conservative lower limit of $1.0\times10^{14}$ at$\cdot$s$^{-1}\cdot$m$^{-2}$ on the atomic flux density for the slow beam provided by the pre-source in the 2D-MOT configuration and for a cesium pressure of $\simeq 4\times10^{-8}$ mbar.

### 6.4.3 Fluorescence

Many signals presented in this chapter show fluorescence. They were calibrated by simultaneous recording of absorption signals characterised above.

## 6.5 Main characteristics of pre-source and influence of parameters: experimental results

In the following we present the experimental characterisation of the slow atomic beam obtained for the 2D-MOT (2D$^+$-MOT) and for the configuration with no $\nabla$B (2D-OM). We studied the detected atomic flux as a function of cooling laser beam power, *x'-y'* power imbalance, frequency detuning and polarisation. We measured the transverse and longitudinal velocity distributions of the collimated atomic beam by Doppler broadening and Time of Flight (TOF), respectively. Finally, we analysed the transverse beam profile by translating the whole detection system perpendicularly to the atomic beam.

In this section all the results were obtained for a cesium pressure in the pre-source of $\sim 4\times10^{-8}$ mbar and calibrated as described in Sec. 6.4.

### 6.5.1 Atomic flux density

We have studied the influence of the parameters on the detected atomic flux density. We collect the fluorescence emitted from the atomic beam excited by the probe laser (see Fig. 6.9). Some experimental parameters are fixed: the pumper beam overlapped on the cooling beam has a power of 1.6 mW, the probe laser 2 mW and its repumper 0.2 mW.
First, we varied the power of the cooling laser beam between 0 and 200 mW searching for a saturation effect of the fluorescence atomic signal. The result is shown in Fig. 6.11: for the maximum power available, the signal still

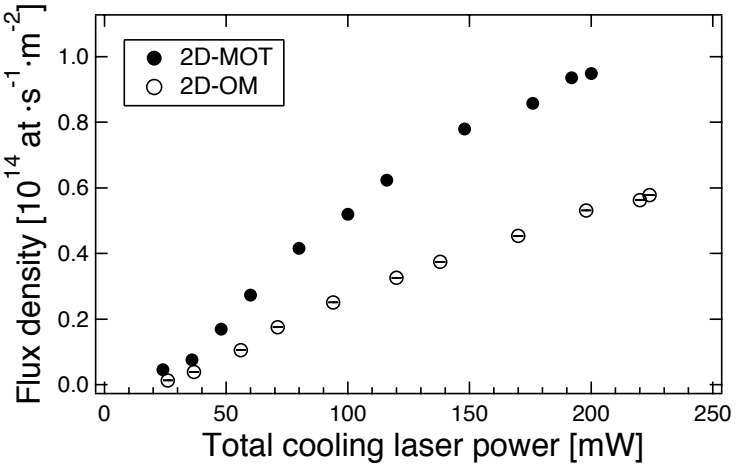


**Figure 6.11**: Atomic flux density versus total cooling laser power. The data points were obtained observing the fluorescence induced by the probe laser beam transverse to the atomic beam with a weak repumper overlapped. The cooling beam detuning from the $F = 4 \rightarrow F' = 5$ transition is -8 MHz for both 2D-MOT and 2D-OM configurations. $\nabla$B=2.6 G/cm for the MOT.

increases though less than linearly. This means that we do not reach a saturation regime and more laser power could increase even more the pre-source performance. With the maximum power available of the cooling laser, we have done a similar test varying the pumper laser power. In this case we observe a saturation effect yet at 0.7 mW (see Fig. 6.12).

We changed then the laser cooling detuning. Figure 6.13 gives us information about the optimum value around -1.5 $\Gamma$ for the 2D-MOT and somewhat higher for the 2D-OM (-2.0 $\Gamma$). As expected, in the blue region of the $F = 4 \rightarrow F' = 5$ transition the cooling mechanism does not work at all. The magnetic field gradient chosen for these measurements was equal to 2.6 G/cm. This value optimises, as shown in Fig. 6.14, the atomic flux at the detection. As mentioned later in Sec. 6.6, similar experiments in other labs require a stronger magnetic field gradient because they have a smaller exit hole at the output of the trap, which needs a higher collimation. In the course of our pre-source characterisation we have converged to an optimal magnetic gradient even smaller, namely 1.3 G/cm.

We also studied the sensitivity of the detected signal due to an imbalance of the cooling laser light intensity along the 2D-trap axes, obtained by rotating a half-wave plate. The maximum flux is observed for the orientation of the plate that balances the laser power along the two directions. In the extreme case of a 1D-configuration, *i.e.* when the cooling mechanism acts only in one direction of the MOT, the fluorescence signal is reduced by almost an order of magnitude (Fig. 6.15).

Finally we varied the cooling laser polarisation by rotating the quarter-

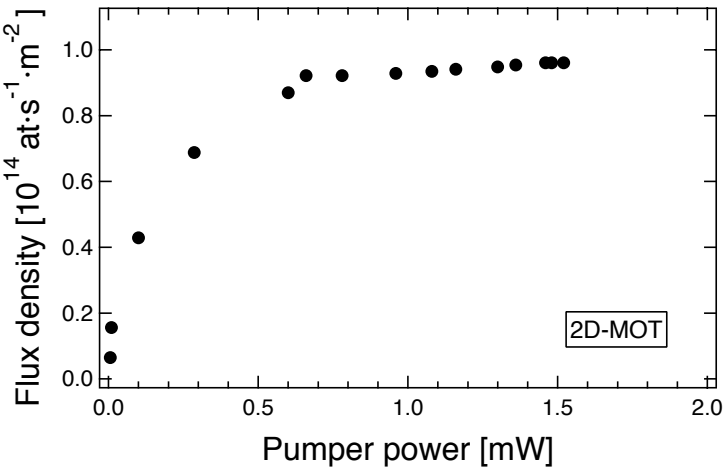


**Figure 6.12**: Atomic flux density versus total pumper laser power. The cooling laser power is 200 mW. Other experimental parameters as in Fig. 6.11.

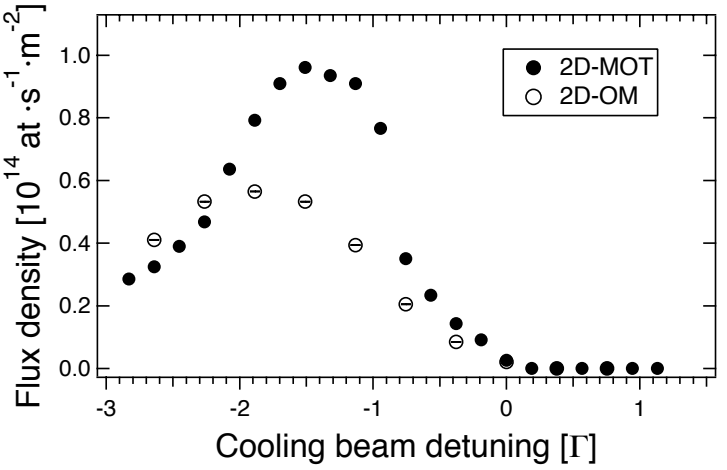


**Figure 6.13**: Atomic flux density versus cooling laser detuning. The cooling laser power is 200 mW. Other experimental parameters as in Fig. 6.11.

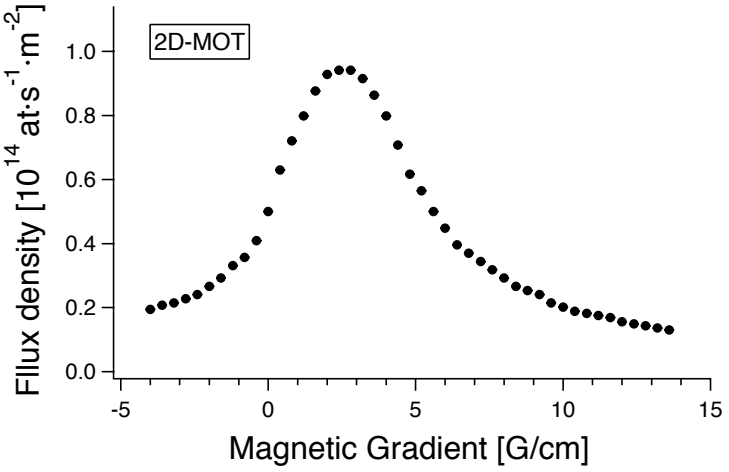


**Figure 6.14**: Atomic flux density versus magnetic field gradient. The cooling laser power is 200 mW. Other experimental parameters as in Fig. 6.11.

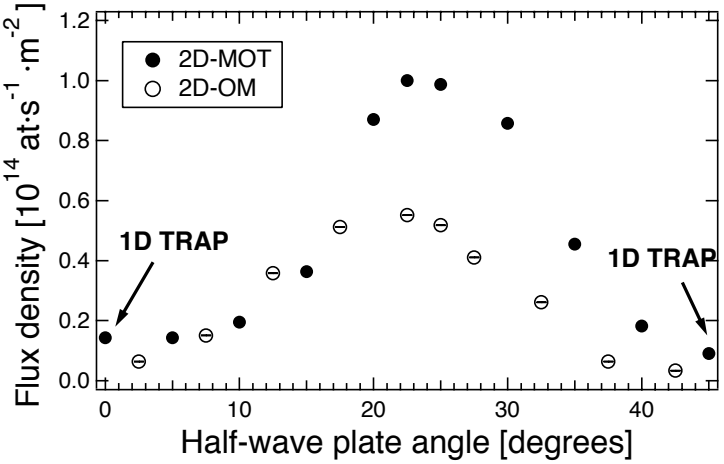


**Figure 6.15**: Atomic flux density as a function of the 2D-trap axes power imbalance. The cooling laser beam has a power of 200 mW and a detuning of -8 MHz. The other parameters are the same as in Fig. 6.11. The imbalance is generated by rotation of the half-wave plate placed before the polarising beam splitter shown in Fig. 6.2; an angle of $0\,^\circ$ corresponds to a one-dimensional trap along the $y$'-axis, while for a rotation of $45\,^\circ$ the trap operates only along the $x$'-axis.

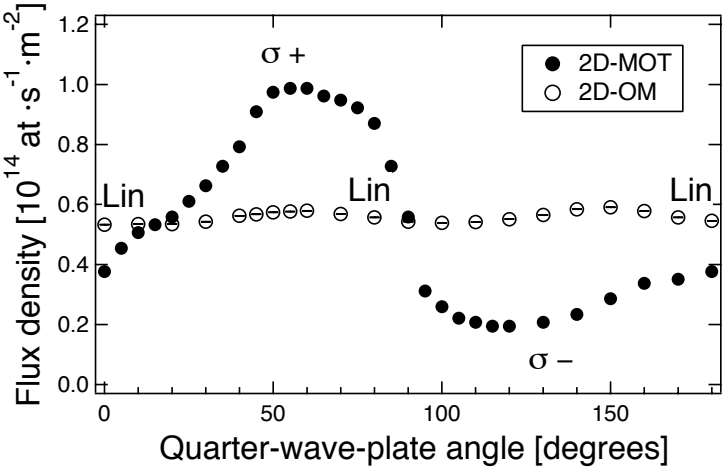


**Figure 6.16**: Atomic flux density versus the polarisation of the cooling beams changed by rotating simultaneously the two quarter-wave plates placed at the entrance of the glass cell, along the 2D-MOT axes. The polarisation is $\sigma^+$ for an angle of 45 °, linear for 0 °, 90 ° and 180 ° and $\sigma^-$ for 135 °. Other parameters as in Fig. 6.11.

wave plates at the entrance of the glass cell. In the 2D-OM configuration no dependence upon laser polarisation is observed, *i.e.* essentially Doppler cooling acts with no evidence of sub-Doppler cooling. By contrast in the 2D-MOT there is a strong variation of the fluorescence signal, confirming that the 2D-MOT needs circular polarisation to work: consistent with the orientation of the magnetic field gradient, the atomic flux is maximum for purely $\sigma^+$ polarisation and almost null for the opposite $\sigma^-$ value (Fig. 6.16).

### 6.5.2 Transverse velocity

To deduce the transverse velocity spread of the collimated atomic beam, we observed the transmission of a weak probe laser beam oriented along $y$ perpendicularly to the atomic beam. For an atom at rest we would obtain a resonance curve with a lorentzian shape whose FWHM were given by the 5.22 MHz natural width. Ideally, once the slight saturation broadening is accounted for, the resonance curve would be only broadened by the transverse velocity distribution of the atomic beam. The one observed has a FWHM of at most 6.3 MHz (see Fig. 6.17 for a typical result). However, some of this broadening is almost certainly attributable to slight irreproducibility of the frequency scan ramp. By fitting this curve with a Voigt profile (convolution between a gaussian velocity distribution and a lorentzian distribution with the natural width), we obtain a conservative upper limit of the full velocity spread of about 1 m·s$^{-1}$. For a longitudinal velocity of 25 m·s$^{-1}$ (see Sec. 6.5.4) this corresponds to a full beam divergence $\leq$ 40 mrad. We observed no significant difference between the three pre-source configurations.

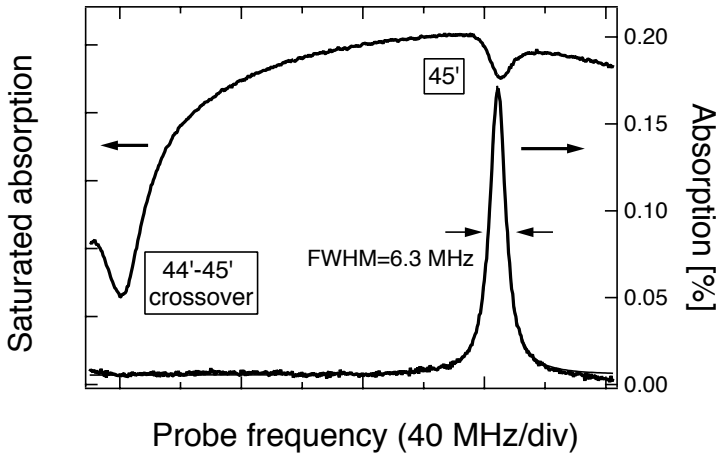


**Figure 6.17**: Absorption spectrum of a probe laser beam transverse to the atomic beam 500 mm downstream. Probe saturation parameter of 0.2. The width of the resonance gives us information about the transverse velocity spread. Upper trace: saturated absorption signal providing frequency calibration.

### 6.5.3 Atomic beam profile

We measured the transverse beam density profile by translating the whole detection system (probe laser and transmission photodetector) perpendicularly to the axis of the atomic beam, with the probe transverse to the atomic beam. The probe beam diameter was reduced from 5 to 2 mm to provide better spatial resolution. The probe frequency was locked to the centre of the $F = 4 \rightarrow F' = 5$ transition.

The width (FWHM) of the spatial distribution is found to be 9 mm for $\nabla$B $\simeq$1.3 G/cm (value optimising the atomic flux) and 15 mm for $\nabla$B= 0 (Fig. 6.18). For a point source these would correspond to a maximum full beam divergence of 18 and 30 mrad respectively, compatible with the limit inferred from Doppler spectroscopy (see Sec. 6.5.2). The narrower profile obtained in the MOT configuration was expected since the Doppler cooling process operates in a tighter spatial confinement than in the OM. However, this difference in divergence translated into transverse velocity spread is too small to be distinguished by the transverse Doppler spectroscopy presented above. We conclude that the source is highly directional, a valuable attribute for efficient loading of a 3D-optical molasses.

### 6.5.4 Longitudinal velocity

For TOF measurements, the plug laser, modulated by a mechanical chopper wheel (f=7 Hz), cuts the slow atomic beam into slices of 1.5 ms duration. For each of these, at a distance L=500 mm downstream, we record the fluores-

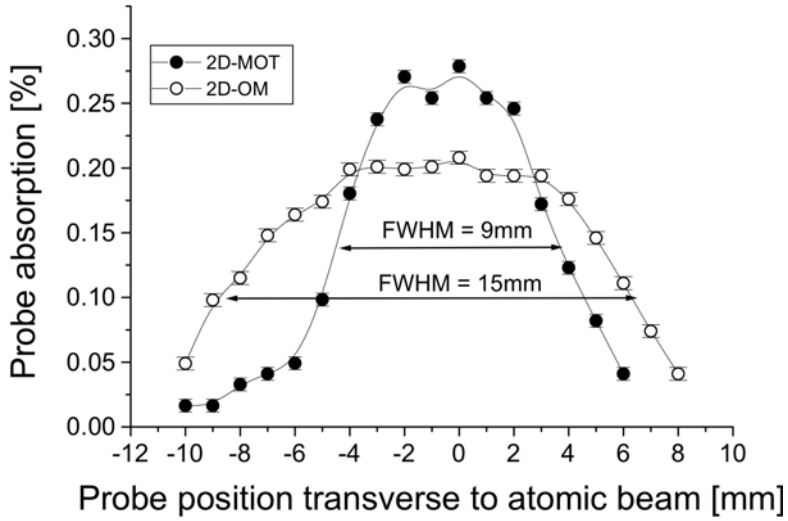


**Figure 6.18**: Atomic beam profiles measured by probe absorption at a distance of 500 mm from the exit of the pre-source. Filled circles: standard 2D-MOT configuration; open circles: configuration with no magnetic field gradient (2D-OM); the solid lines are guidelines.

cence induced by the cw transverse probe beam tuned to the $F = 4 \rightarrow F' = 5$ transition. The fluorescence signal (Fig. 6.19a) is proportional to the instantaneous atomic density *n(L,t)*:

$$Signal_{TOF} = n(L,t) \tag{6.11}$$

The integral function of *n(L,t)* converges to the total atomic density $N(L)$. Passing from a temporal to a velocity distribution (by using $v = L/t$) and imposing the atom total number conservation we can write:

$$\frac{dN(v)}{dv}\, dv = \frac{dN(L,t)}{dt}\, dt \;\Rightarrow\; n(v)\, dv = n(L,t)\, dt \tag{6.12}$$

The atomic flux density $\varphi(v)$ can be calculated using the equation:

$$\varphi(v) = v \cdot\; n(v) \tag{6.13}$$

thus, replacing $n(v)$ by using the Eq. 6.12, we obtain:

$$\varphi(v) = v \cdot\; n(L,t)\, \frac{dt}{dv} = v \cdot\; n(L,t)\, \frac{L}{v^2} = n(L,t) \cdot\; t \tag{6.14}$$

$\varphi = \int \varphi(v)\, dv$ is the total flux density. Multiplying by the transverse beam size measured at the distance L we find the total flux $\Phi$.

The experimental conditions ($\nabla$B and cooling beam detuning) were optimised to yield the maximum flux in continuous operation. Fig. 6.19 shows the results for the different pre-source configurations. No essential difference is observed between the 2D-OM and 2D-MOT: peak velocity around

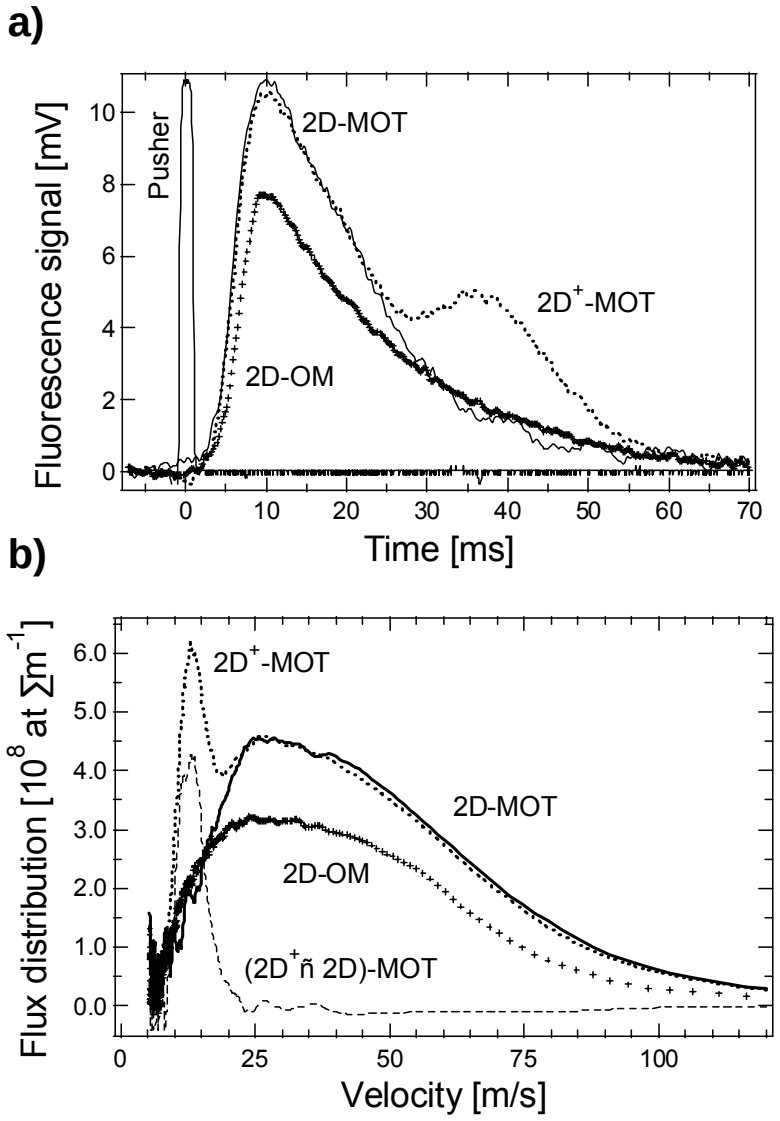


**Figure 6.19**: a) Time of flight fluorescence signal and b) Corresponding flux distribution as a function of the longitudinal velocity $v$ for the three configurations of the pre-source. Crosses: 2D-OM, solid line: 2D-MOT, dots: $2D^+$-MOT and dashed line: difference between the $2D^+$- and 2D-MOT's. Cooling laser detuning -10 MHz, $\nabla B \simeq 1.3$ G/cm for the MOT's. The probe laser beam is tuned to the $F = 4 \rightarrow F' = 5$ transition with the repumper overlapped.

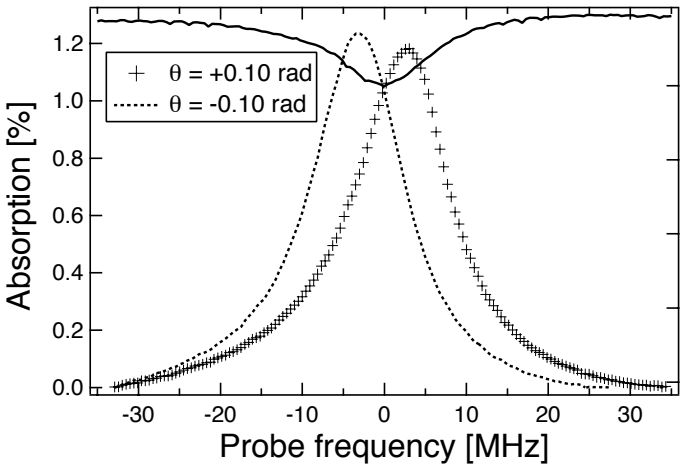


**Figure 6.20**: Absorption spectra in the region of $F = 4 \rightarrow F' = 5$ of a probe laser beam that crosses the atomic beam with an angle of +0.1 rad and -0.1 rad towards the atomic beam axis. The saturated absorption curve partially shown (solid line) provides frequency calibration. 2D-MOT parameters as in Fig. 6.19.

25 m·s$^{-1}$ and full velocity spread about 50 m·s$^{-1}$, slightly larger for the OM case together with a reduction in total flux of $\simeq 30\%$. However, for the 2D$^+$-MOT configuration, in addition to the distribution found in the 2D-MOT case, a narrow peak (FWHM 5 m·s$^{-1}$) appears centred at the low velocity of 13 m·s$^{-1}$. This structure increases the total flux, though by no more than 30%. Incidentally, we find the same gain in total flux for a configuration 2D$^+$-OM with respect to the simple 2D-OM.

We have confirmed these results by Doppler absorption spectroscopy. Due to limited optical access, we cannot align the probe along the atomic beam axis, as desired for maximum sensitivity to the longitudinal velocity. In a first experiment the initially transverse probe beam (power 0.15 mW, diameter 5 mm) was tilted at an angle $+\theta$ then $-\theta$ ($\theta \simeq 0.1$ rad) towards the axis of the atomic beam and the transmission of this laser beam in the region of the $F = 4 \rightarrow F' = 5$ transition was recorded. The frequency shift between the absorption resonance and the centre of a reference atomic resonance (simultaneously monitored by saturated absorption in a dedicated cell) is the Doppler shift associated with a given longitudinal velocity. Fig. 6.20 shows the results obtained for the 2D-MOT. At the absorption peak the shift is $\simeq 6$ MHz, while for the 2D$^+$-MOT it is $\simeq 4.7$ MHz.

Using the first order Doppler shift formula:

$$\nu - \nu_0 = \frac{\overrightarrow{k}}{2\pi} \cdot \overrightarrow{v} = \frac{v}{\lambda} \sin\theta \tag{6.15}$$

where $\nu$ is the probe frequency, $\nu_0$ the atomic resonance frequency, $\overrightarrow{k}$ the wave vector, $\overrightarrow{v}$ the beam velocity and $\lambda$ the wavelength, we find an average

longitudinal velocity of $\simeq 26$ m·s$^{-1}$ and 20 m·s$^{-1}$ for the 2D- and 2D$^+$-MOT configurations respectively, values consistent with the velocity distributions given by the TOF technique.

In a second experiment the probe was aligned along the $\pm X$ horizontal axis at $\pm 45^\circ$ to the atomic beam. With no repumper, the Doppler shifted probe absorption signal directly yields the atomic beam *flux* distribution $\varphi(v)$. Fig. 6.21 shows the results for the 2D- and 2D$^+$-traps and both co- and contra-propagating probe beams. Though noisier, they compare favourably with the distributions obtained using TOF (see Fig. 6.19). In particular the 2D$^+$ distributions are shifted towards lower velocities (peak around $15 \pm 2$ m·s$^{-1}$) compared to the 2D's (peaked around $23 \pm 2$ m·s$^{-1}$).

It is possible to enhance the signal-to-noise ratio using a repumper tuned to $F = 3 \rightarrow F' = 4$. However, care must be taken in this case to avoid velocity selective hyperfine pumping since the repumper frequency is fixed. Thus we employed a 30 mm-dia. repumper *transverse* to both probe and atomic beams. Note that here one measures the atomic beam *density* distribution *dn/dv* from which the flux distribution *v·dn/dv* can be recovered. The results also agree well for both the 2D- and 2D$^+$-MOTs and for co- and contra-propagating probe beams.

## 6.6 Comparison with other similar work

As already pointed out, our device differs from other MOTs via the use of gold-coated optical prisms in place of mirrors and quarter-wave plates. Yet this novel simplification does not hinder performance and the source stands comparison with similar work. To illustrate this we discuss the traps of references [35, 46, 51] and mention some important differences. In Tab. 6.1 we summarise the characteristics of the slow beams analysed in this section as well as those of references [33, 42, 49, 52].

- In our pre-source the cooling laser power is recycled, which allows one to work with cooling beams of at most 220 mW. In [35] the total power is similar to ours but is split into four beams while in [51] the cooling laser light, provided by a Ti:sapphire laser, has a power of 160 mW per beam. The trap in [46] is a compact magneto-optical source where the total power is only 60 mW, carefully distributed among the four beams. Indeed, a possible criticism of our design concerns the imbalance of the light intensity due to absorption losses in vapour and optics; lower losses would surely improve performance.

- We employ an optimised magnetic field gradient in the range of $1.0-1.5$ G/cm, a value more than an order of magnitude lower than that used in [35, 51] though the cell dimensions are quite similar. In [46] this difference is

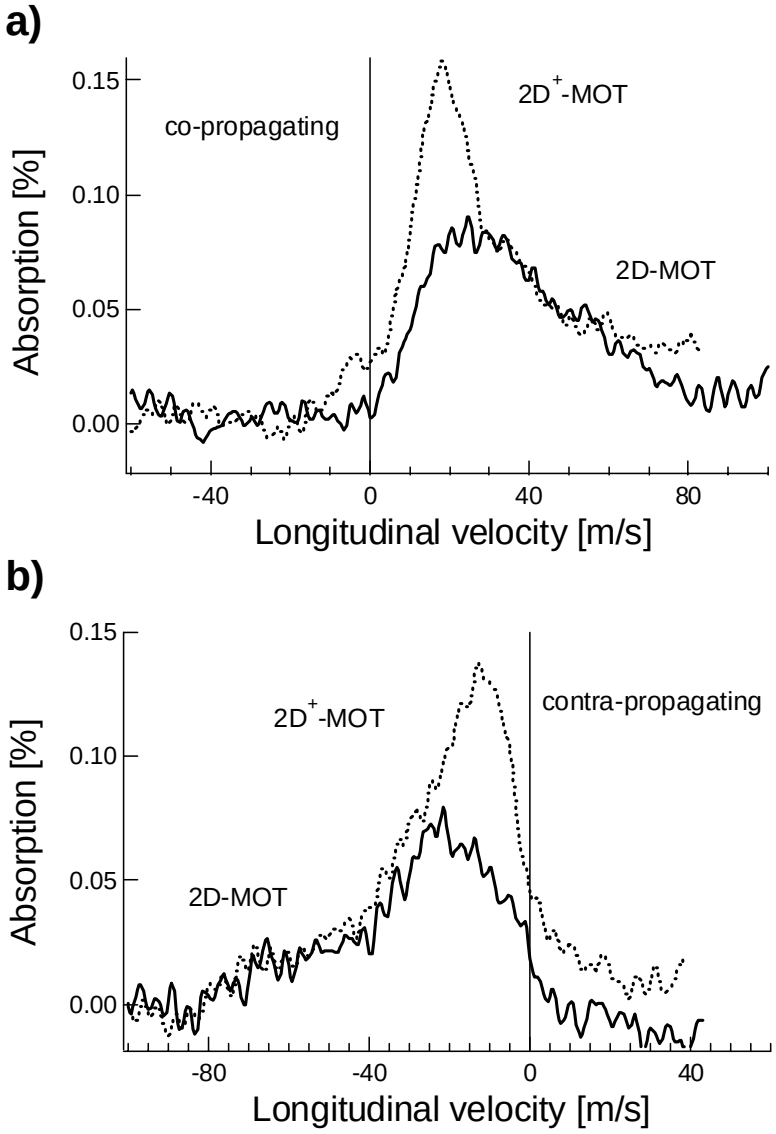


**Figure 6.21**: Doppler shifted absorption spectra in the region of the $F = 4 \rightarrow F' = 5$ transition for a probe beam oriented at $\pm 45\,^\circ$ to the atomic beam (a and b for co- and contra-propagating geometries), without repumper. Saturating power $\simeq$2 mW, diameter 5 mm. The scanned probe frequency is calibrated in atomic beam longitudinal velocity ($\Delta v = \sqrt{2}\lambda \cdot \Delta\nu$). Dotted and full lines for $2D^+$- and 2D-MOT pre-source.

less though their trap has a considerably smaller volume. A low magnetic field gradient is desirable for many applications where stray fields are harmful (atomic clocks for instance). Moreover, our source works almost as well with no gradient at all, which is even better from this point of view. This behaviour we attribute to the large size of the exit hole (16 mm) which allows cold atoms to contribute to the slow beam be they close to the axis or not. Note that this large exit hole allows an efficient pumping (the total conductance between the UHV chamber and the pre-source is equal to 7.35 l/s) without introduction of undesired Cs background in the region where we have performed the characterisation, even if we do not use Cs getters in our device.

- Our measured atomic flux, even if obtained at the lower vapour pressure in the pre-source of $\sim 4\times10^{-8}$ mbar, is twice higher than that of [46] and of the same order as the one in [35]. In [51] the atomic flux is 6 times higher than ours for a vapour pressure in their cell set to the optimum value of $2\times10^{-6}$ mbar though long-term contamination by Cs might be an issue at such high density.

- Finally, the longitudinal velocity of the atomic beam measured in this work has a broad distribution centred around 27 $\mathrm{m{\cdot}s^{-1}}$ for the 2D-MOT configuration, a value higher than those of [35] (20 $\mathrm{m{\cdot}s^{-1}}$) and [46] ($\sim$10 $\mathrm{m{\cdot}s^{-1}}$). A low longitudinal velocity would be an advantage for Doppler capture and in fact for the $2D^{+}$-MOT configuration, the longitudinal velocity distribution is reminiscent of that described in [51], with a narrow peak around 15 $\mathrm{m{\cdot}s^{-1}}$, ideal for loading a 3D molasses, as discussed below.

| Parameter | Present Work[a] | Petelski Ref. [33, 34][b] | Chelkowski Ref. [35][b] | Kohel Ref. [42][c] | Ovchinnikov Ref. [46][a] | Berthoud Ref. [49][d] | Schoser Re. [51][a] | Dieckmann Ref. [52][a] |
|---|---|---|---|---|---|---|---|---|
| Atomic flux [$10^9$ at·s$^{-1}$] | 13 | 11 | 11 | 2.2 | 8 | 0.13 | 60 | 9 |
| Cs pressure [$10^{-8}$ mbar] | 4 | 12 | n.a. | 0.25 | 32 | 4 | 160 | 15 |
| $\nabla\mathbf{B}$ [G·cm$^{-1}$] | 1.0-1.5 | 20 | 19 | n.a. | 6 | 12.5 | 17 | 12.6 |
| $v_L$ [m·s$^{-1}$] | 20 | 20 | 20 | 15 | 11 | 0.7-3 | 15 | 8 |
| $P_{tot}$ [mW] | 220 | 140 | 220 | 600 | 60 | 60 | 640 | 34 |

[a] 2D$^+$-MOT, [b] 2D-MOT, [c] Pyramidal trap, [d] 2D-MOT+3D-OM.

**Table 6.1**: Summary of the characteristics of various slow beam sources. $\nabla\mathbf{B}$ is the magnetic field gradient, $v_L$ the peak longitudinal velocity and $P_{tot}$ the cooling laser total power.

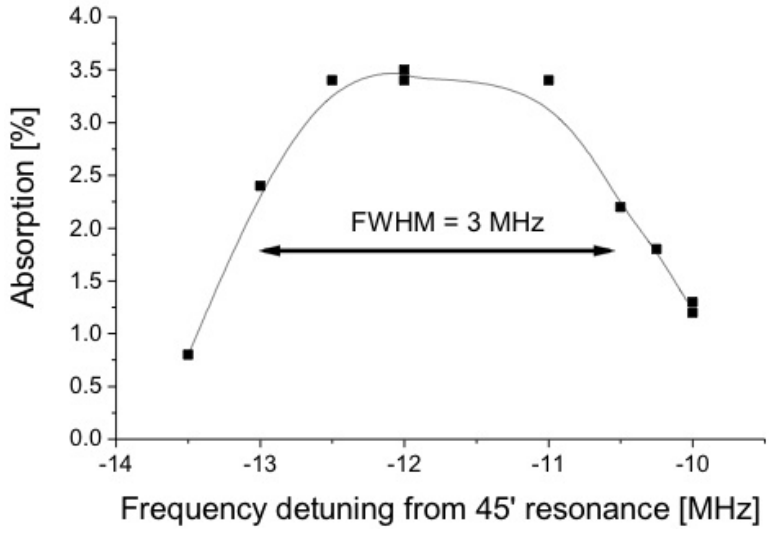


**Figure 6.22**: Probe absorption by the 3D-optical molasses loaded by the slow atomic beam: dependence on the molasses laser detuning from the $F = 4 \rightarrow F' = 5$ transition. Probe laser tuned to the $F = 4 \rightarrow F' = 5$ transition.

## 6.7 Capturing the atomic beam in the static 3D optical molasses

It has to be emphasized that the purpose of building a pre-source is to improve the useful atomic flux in a continuous cesium fountain clock [9]. Currently, we feed the atomic clock by loading a 3D-OM from a thermal cesium vapour. In this section we analyse the gain obtainable by loading it by the slow atomic beam exiting from the 2D-MOT (see Fig. 6.9 for the experimental schematic).

The detuning that maximises the capture by Doppler cooling was determined using probe absorption by the slow beam loaded 3D-OM. The result, shown in Fig. 6.22, is a frequency profile centered around -12 MHz, the optimum being independent of loading technique.

Then the parameters of the pre-source were adjusted to optimise the absorption signal: we found them to be slightly different (cooling laser detuning $\delta_{2D} \simeq$-11 MHz and $\nabla B \simeq 0.8$ G/cm) than without capture. When we switched from the 2D- to the 2D$^+$-MOT configuration, most remarkably, the absorption signal was increased by a factor of $\simeq 1.8$ while without capture the gain was only 30% (see Fig. 6.19). A similar behaviour was observed for a 2D- versus 2D$^+$-OM comparison. These effects we ascribe to increased 3D-OM capture efficiency for slow atoms.

Next we compare probe absorption for the 3D-OM loading by a thermal cesium vapour or by the slow atomic beam. For this purpose we use a second reservoir and isolate the pre-source from the UHV chamber by closing the

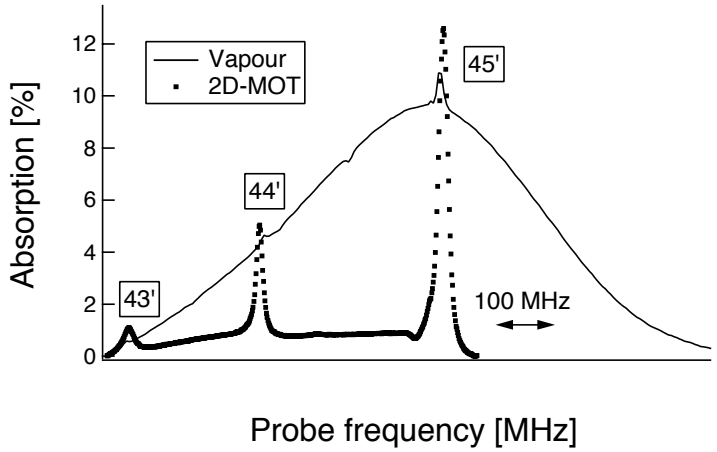


**Figure 6.23**: Spectrum of the probe absorption across D2 line in the 3D-optical molasses region. Loading by cesium vapour (solid line) or from the 2D-MOT slow atomic beam (dotted line). Probe laser beam (diameter 5 mm and total power 0.15 mW) overlapped by a weak repumper beam for vapour loading.

gate valve. Typical results are shown in Fig. 6.23. For loading from a vapour $\sim 10^{-8}$ mbar we observed a Doppler broadened absorption of the order of 10−15% along 250 mm of vapour column (internal diameter of the chamber) with small sub-Doppler peaks centered on the $F = 4 \rightarrow F' = 4$ and $F = 4 \rightarrow F' = 5$ atomic resonances due to slow atoms captured in the 3D-OM. These have to be compared with the peaks associated with slow beam loading: the capture efficiency is $\sim 8$ times higher in the latter case. A second positive aspect provided by using the pre-source is highlighted by the images recorded by a CCD camera (Fig. 6.24). The striking difference is the presence of fluorescent light along the 3D-molasses laser beam axes in Fig. 6.24b, indicating diffuse vapour absent in Fig. 6.24a. This confirms the confinement of the atoms in the region of interest and *quasi*-absence ($4\times10^{-10}$ mbar) of thermal background atoms for pre-source loading the 3D-OM despite the large exit hole and the absence of getters.

Finally, we increased the useful atomic flux still further by raising the cesium pressure inside the pre-source (kept constant until now at about $4\times10^{-8}$ mbar). This aspect is analysed in the next section, where we deal with the launch of the slow atoms captured by the 3D-OM in a vertical fountain.

## 6.8 Launch configuration

The set-up was modified as shown in Fig. 6.25 where we transferred the detection system from the 3D-OM region to a point 470 mm above it while

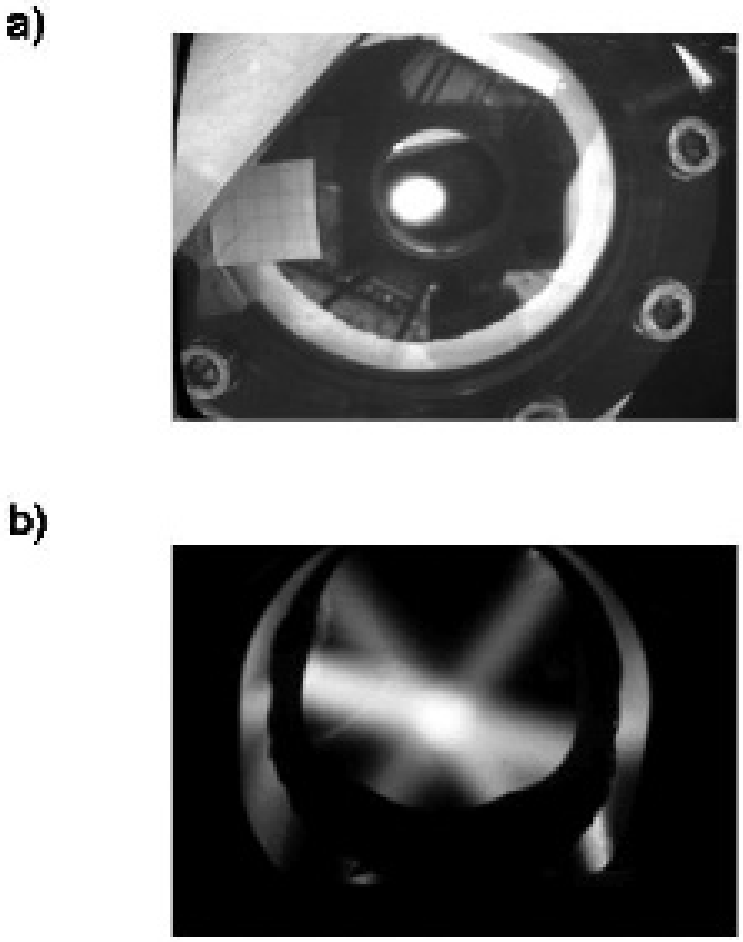


**Figure 6.24**: Pictures showing the fluorescent light emitted in the 3D static optical molasses. a) Loading by the slow atomic beam: bright central spot of ∼15 mm diameter. Note the absence of fluorescence from the six molasses beams. b) Loading by a Cs vapour: the fluorescence induced by thermal vapour absent in a) is conspicuous along the 3D-molasses laser beam axes.

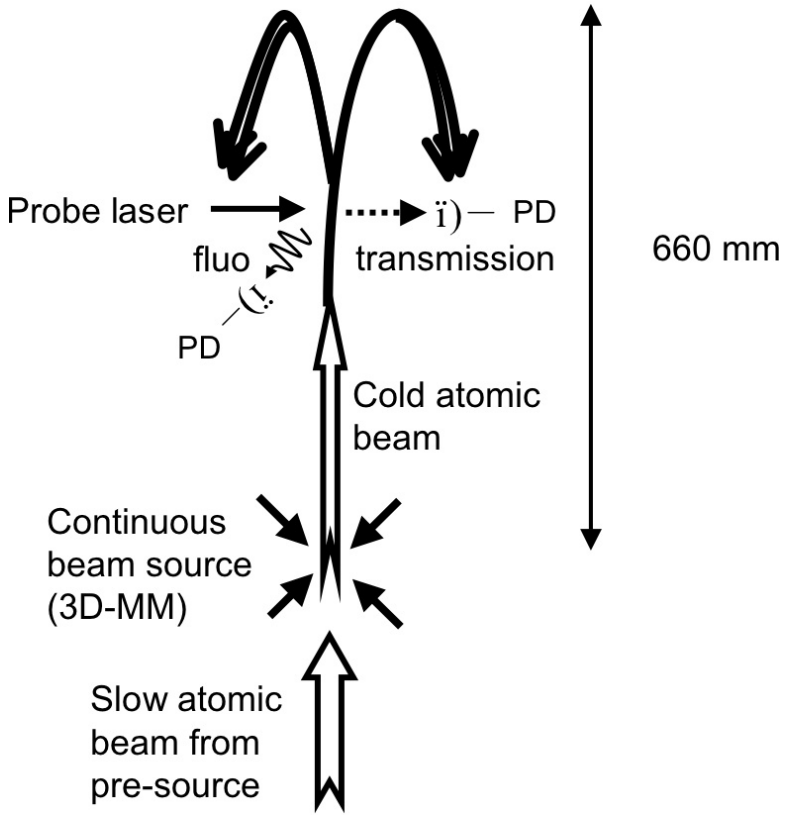


**Figure 6.25**: Schematic of the launch configuration for the fountain. PD: Photodetector, MM: Moving optical Molasses. Note that the slow atomic beam is at 45 ° to the vertical.

retaining the possibility to monitor both transmission and fluorescence. The cold atoms captured by the 3D-OM are launched vertically using a *moving* optical molasses. Here the two up-going (down-going) beams are detuned by +3 MHz (−3 MHz) with respect to the horizontal retro-reflected beam, held at −12 MHz from the $F = 4 \rightarrow F' = 5$ transition. This frequency difference provides a vertical launch velocity of 3.6 m·s$^{-1}$.

In this configuration we measured both fluorescence and absorption induced by the probe laser beam (0.5 to 2 mW power, 5 mm diameter) for different loading techniques of the source.

Fig. 6.26 shows the main result of this work, namely that *2D-MOT-slow-beam loading gives 10 times more flux than vapour capture; the 2D$^+$-MOT almost doubles this.* The transverse cold beam profiles also recorded for the 2D-MOT- and vapour-loading of the 3D-OM were quite similar. Tab. 6.2 summarises these results.

As regards the impact of the cesium pressure inside the pre-source (Fig. 6.27), we find a maximum atomic flux density ($\varphi = 8.5{\times}10^{13}$ at $\cdot$ s$^{-1}\cdot$ m$^{-2}$) for the rather high value of $1.2{\times}10^{-7}$ mbar, corresponding to an absorption of 17% in the pre-source (for a 3 cm transverse path). While this is encouraging,

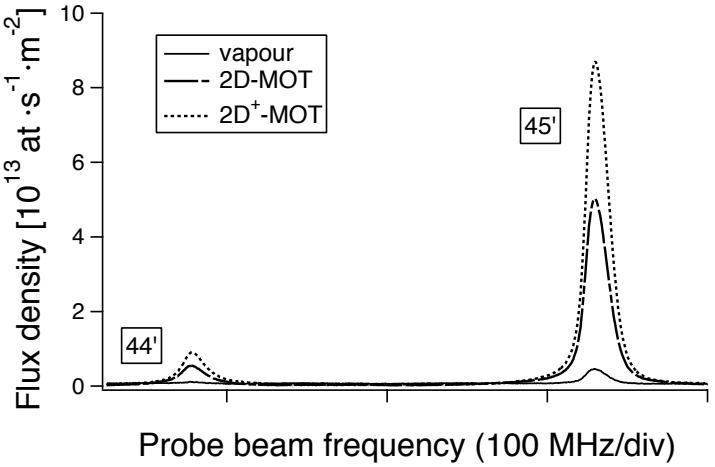


**Figure 6.26**: Fluorescence spectrum calibrated in flux density detected 470 mm above the 3D-OM source in a launch configuration upwards. Comparison between the two different techniques to load the source: from cesium vapour (full line) or from the slow atomic beam produced by the pre-source in either the 2D-MOT (dashed line) or the 2D$^+$-MOT (dotted line) configuration. Vapour pressure $\simeq 1.2\times10^{-7}$ mbar in the pre-source and $\simeq 10^{-8}$ mbar in the UHV chamber.

**Table 6.2**: Summary of methods for loading a continuous cold atom fountain. Atomic flux density $\varphi$ and transverse diameter ø of fountain beam at a distance of 470 mm above the 3D-OM source, with a vertical launch velocity of 3.6 m·s$^{-1}$. Comparison for pre-source (2D- and 2D$^+$-MOT) at Cs vapour pressure $1.2\times10^{-7}$ mbar and for vapour loading at $0.8\times10^{-8}$ mbar.

| | Vapour | 2D-MOT | 2D$^+$-MOT |
|---|---|---|---|
| $\varphi$ ($10^{13}$ at·s$^{-1}$·m$^{-2}$) | 0.4 | 4.5 | 8.5 |
| ø (mm) | 16.4 (0.3) | 15.0 (0.1) | - |

in practice a somewhat lower pressure might be used to extend the working lifetime of the device. For even higher pressure, the detected flux falls owing to the greater collision rate and increased imbalance of the cooling laser beams due to higher absorption in the pre-source.

## 6.9 Conclusions and perspectives

We have developed and completely characterised a two-dimensional source of slow Cs atoms with the aim of loading a continuous atomic beam fountain. A comparison of the characteristics for the 2D-MOT, 2D-OM and 2D$^+$-MOT configurations is summarised in Tab. 6.3. The innovative set-up with *i*) low cost optics, *ii*) absence of differential pumping and *iii*) exit hole with no diaphragm, is shown not to limit the performance of our de-

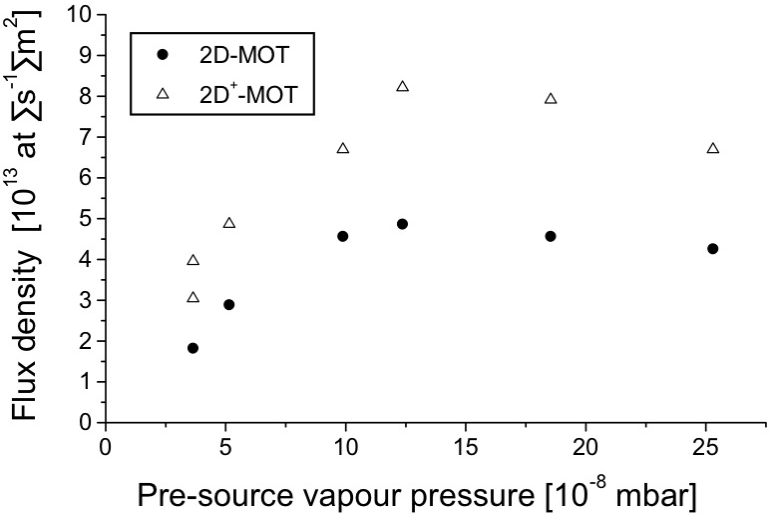


**Figure 6.27**: Atomic flux launched vertically from a 3D moving molasses as a function of the cesium vapour pressure inside the pre-source used to load it, for both the 2D-MOT and the $2D^+$-MOT configurations. Detection by induced fluorescence with probe beam tuned to the $F = 4 \rightarrow F' = 5$ transition.

vice. The slow atomic beam provided by the pre-source has been captured in a UHV chamber by a 3D-OM 500 mm downstream and then launched in a vertical flight. Loading the molasses using the 2D-MOT provides a gain in the detected flux by a factor of $\simeq 10$ compared with thermal cesium vapour capture, the method used heretofore to feed our atomic clock fountain. An added advantage is the *quasi*-absence of thermal background atoms. The introduction of a pusher beam in the pre-source ($2D^+$-MOT) increases the fountain flux by a further factor of $\simeq 1.8$, as a result of a more favorable longitudinal velocity distribution. This suggests we might boost the fountain flux even more by shortening the length of the pre-source cell, as demonstrated in [51]. At the optimum vapour pressure in the pre-source of $1.2\times10^{-7}$ mbar and for a $2D^+$-MOT configuration we achieved a highest flux density of $8.5\times10^{13}$ at $\cdot\ s^{-1}\cdot\ m^{-2}$. Our results yield a potential gain of $\sqrt{20}$ in stability of an *atomic shot noise limited* fountain clock, though the signal-to-noise remains to be investigated. In particular it must be verified that the obtained improvement in atomic flux corresponds to a real improvement of the signal-to-noise ratio, *i.e.* any new source of noise does not depend on the atomic flux and is negligible with respect to the atomic shot noise.

**Table 6.3**: Comparison of the characteristics of the slow atomic beam for the 2D-MOT, 2D-OM and 2D$^+$-MOT configurations. $\varphi$ is the maximum atomic flux density, $v_L$ the peak longitudinal velocity, $\Delta v_T$ the transverse velocity spread and $\Phi$ the atomic flux. The total flux is calculated using the transverse beam size measured at 500 mm from the exit (see fig. 6.18) and assuming it to be the same for the 2D- and the 2D$^+$-MOT configurations. Note that Cs vapour pressure in the pre-source is $\sim 4\times10^{-8}$ mbar, namely one third of the optimum value for fountain flux measurements, see Tab. 6.2 and Fig. 6.27.

| | 2D-MOT | 2D-OM | 2D$^+$-MOT |
|---|---|---|---|
| $\varphi$ ($10^{14}$ at·s$^{-1}$·m$^{-2}$) | 1.0 | 0.7 | 1.3 |
| $v_L$ (m·s$^{-1}$) | 27 | 25 | 20* |
| $\Delta v_T$ (m·s$^{-1}$) | $\leq 1$ | $\leq 1$ | $\leq 1$ |
| $\Phi$ ($10^{10}$ at·s$^{-1}$) | 1 | 1 | 1.3 |

* This value is found by averaging the two peaks that characterise the longitudinal velocity distribution for the 2D$^+$-MOT configuration (Fig. 6.19).

# Chapter 7

# Conclusion

In this work we have continued the study and characterisation of transverse collimation techniques and methods to increase the detected atomic flux in a fountain clock begun at ON more than 6 years ago. In the following we summarise the obtained results and then we present some future perspectives.

## 7.1 Results obtained in this work

### 7.1.1 Two-dimensional transverse collimation

We have studied two different transverse collimation techniques: atom cooling in a gray optical molasses and magnetically induced laser cooling. The two mechanisms present several analogies in the cooling process. The main difference between them is the way to perform the Zeeman mixing between a state not coupled with the light field of the two-dimensional optical molasses and a coupled one. While in gray molasses the population redistribution is realised by motional coupling, given the polarisation gradient, in MILC the mixing is done by a transverse static magnetic field, and the optical molasses has no polarisation gradient.

For similar experimental conditions (same cooling laser power, detuning and diameter for the two techniques) we have obtained the results summarised in Tab. 7.1, where we have inserted for comparison also the results obtained by G. Di Domenico in Ref. [10].

Given the results, we envisage to implement in FOCS2 the Sisyphus cooling in a phase stable two-dimensional optical lattice, this cooling technique being the more performing than the other cooling mechanisms studied. With respect to the Sisyphus cooling performed by using two independent laser beams (as in FOCS1), we expect a gain in the detected atomic flux by a factor 2 (ratio between the measured transverse temperature obtained with the two cooling techniques).

**Table 7.1**: Comparison of the results obtained with a two-dimensional transverse collimation performed on the $F = 3 \Rightarrow F' = 2$ transition in a gray molasses (GM) or in an optical molasses with superimposed a static magnetic field (MILC). The cooling laser power was of 3.5 mW, the frequency detuning of $3\Gamma$. For comparison we have inserted also the results obtained by performing Sisyphus cooling on the red side of the $F = 4 \Rightarrow F' = 5$ transition in a phase stable optical lattice. $\varphi$ is the maximum atomic flux density and $T_{trans}$ the transverse temperature after the collimation. Note that the experimental fountain where these techniques have been implemented is loaded by a Cs vapour whose pressure is of $\sim 10^{-8}$ mbar.

| | $\varphi$ ($\mathrm{at{\cdot}s^{-1}{\cdot}m^{-2}}$) | $T_{trans}$ ($\mu$K) |
|---|---|---|
| GM | $2.7 \times 10^{11}$ | 3.5 |
| MILC | $1.8 \times 10^{11}$ | 5 |
| Sisyphus | $3.6 \times 10^{11}$ | 3.5 |

**Table 7.2**: Comparison of the results obtained by loading a continuous cold atom fountain by using a pre-source. Atomic flux density $\varphi$ and transverse diameter ø of fountain beam at a distance of 470 mm above the atomic beam source, with a vertical launch velocity of 3.6 $\mathrm{m{\cdot}s^{-1}}$. Comparison for pre-source (2D- and $2D^+$-MOT) at Cs vapour pressure $1.2{\times}10^{-7}$ mbar and for vapour loading at $0.8{\times}10^{-8}$ mbar.

| | Vapour | 2D-MOT | $2D^+$-MOT |
|---|---|---|---|
| $\varphi$ ($10^{13}$ $\mathrm{at{\cdot}s^{-1}{\cdot}m^{-2}}$) | 0.4 | 4.5 | 8.5 |
| ø (mm) | 16.4 (0.3) | 15.0 (0.1) | - |

### 7.1.2 Two-dimensional magneto-optical trap as pre-source for FOCS2

We have built a magneto-optical trap to load the experimental fountain by a slow atom beam instead of Cs vapour pressure. This pre-source has been characterised under three different configurations: classical 2D-MOT, $2D^+$-MOT (with a pusher laser beam along the longitudinal direction of the pre-source) and 2D-OM (no magnetic field, is a two-dimensional optical molasses). Best performances are reached in the $2D^+$-MOT configuration, for which we detect, 470 mm above the atomic beam source, an atomic flux 20 times greater than the one measured when the fountain is loaded by a Cs vapour (see Tab. 7.2). Note that in our experimental set-up either we perform transverse collimation or we load the source using the pre-source, for practical reasons; thus the transverse temperature of the atomic beam in the configuration with the pre-source is equal to 60 $\mu$K. In FOCS2 we will be able to perform both transverse collimation and loading by the pre-source.

## 7.2 Perspectives

The next step in our investigations to find the best configuration (both source loading and transverse collimation technique) for FOCS2 will be the realisation of a pre-cooling before the collimation in the same optical lattice. This project is motivated by the intention of implementing the sideband Raman cooling induced by Stark effect. Last year we tried to perform this cooling technique with encouraging results; we think that the temperature of the atoms when they reach the collimation region is still too high, so as they are not efficiently captured into the potential wells of the optical lattice. A pre-cooling step could be the solution. The interest of the sideband cooling induced by Stark effect (see Ref. [11]) is that the atoms are accumulated in the $|F = 3, m_F = 0\rangle$ clock state, with a gain of a factor 7 (number of Zeeman sub-levels of $F = 3$) in the atomic flux. More than this, the absence of any magnetic field to perform the collimation is a remarkable advantage in an application where stray fields are harmful.

## 7.3 Higher flux, but better performance?

The obtained increase of the detected atomic flux is really a gain if the dominant noise source is still the atomic shot noise. If this condition is satisfied, then the factor 40 gained (after the introduction of the pre-source and the Sisyphus transverse collimation in a phase stable optical lattice) in the detected flux is a gain also for the clock frequency stability. The latter would be improved by a factor $\sqrt{40}$. If we make the hypothesis that the frequency stability of our clock is improved by a factor $\sqrt{40}$, then we need also that the local oscillator does not limit the frequency stability. For this reason we envisage to replace the local oscillator by an optical comb.
On the other hand, the increased fluorescence in the detection region could represent a limit on the frequency accuracy, with a light shift that could perturb the atomic levels. In Appendix B we make the calculation of the light shift due to the fluorescent light in the detection area. This frequency shift acts only on the $F = 4$ hyperfine ground state and not on $F = 3$, not coupled to the light field. We find, with respect to the clock atomic frequency $\nu_0$, a relative light shift of -1.7·10$^{-15}$ (red shift). This value is too small to limit the frequency accuracy of the fountain, but if the detected flux were increased by a factor 40 the light shift would reach a value of $\sim$7·10$^{-14}$. We can measure the light shift with an uncertainty of the order of 1%, but it is not enough to respect the frequency accuracy budget indicated for FOCS2 ($\sim$4·10$^{-16}$). Since the beginning, a second light trap for the detection region was planned. It is however possible that the light shift won't be so high, the calculated value being an upper limit. On the other hand, given the increased atomic flux at the detection, we can simply envisage to reduce the

probe laser power: in this way we would measure the same fluorescent light as in FOCS1 but with an improved signal-to-noise ratio.

# Appendix A

# Characteristics of the $^{133}$Cs atom

This Appendix summarises some of the characteristics of the cesium atom used or mentioned in this work. Figures A.1, A.2 and A.3 are taken from Ref. [10] with the kind permission of the author. The reader can find an extremely detailed description of all the properties of this atom in Ref. [56].

**Table A.1**: Mean characteristics of the cesium atom. The saturated intensity has been calculated as indicated in Ref. [2]

.

| *Propriety* | *Notation* | *Value* |
|---|---|---|
| Atomic number | $Z$ | 55 |
| Atomic masse unity | $A$ | 133 |
| Lifetime of the upper state (D1 line) | $\tau_{D1}$ | 34.90 ns |
| Natural width (D1 line) | $\gamma_{D1}/2\pi$ | 4.56 MHz |
| Saturated intensity (41'-41' D1 line) | $I_{sD1}$ | 2.5 mW·cm$^{-2}$ |
| Lifetime of the upper state (D2 line) | $\tau_{D2}$ | 30.49 ns |
| Natural width (D2 line) | $\gamma_{D2}/2\pi$ | 5.22 MHz |
| Saturated intensity (44'-55' D2 line) | $I_{sD2}$ | 1.1 mW·cm$^{-2}$ |
| Zeeman splitting | $\Omega$ | 350 kHz/G |

## A.1 Atomic energy levels: D1 and D2 lines

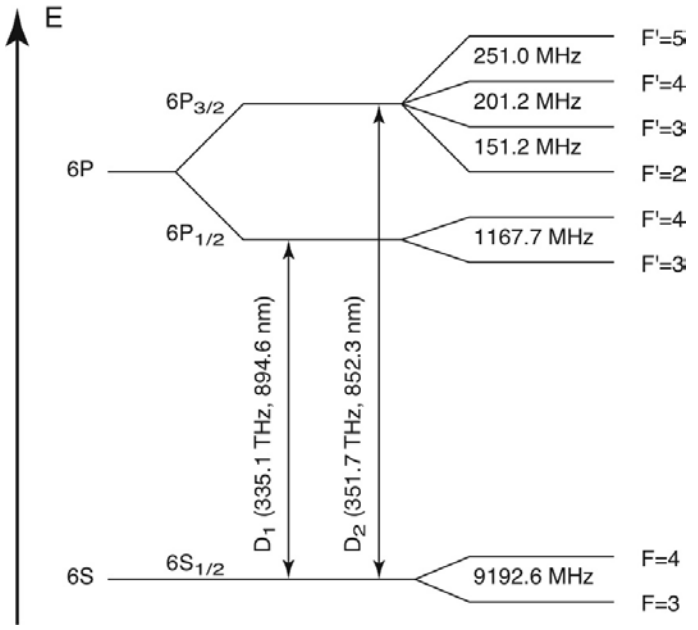


**Figure A.1**: Hyperfine transitions of the $^{133}$Cs D1 and D2 lines. Note that the hyperfine splitting of the D1 line exceeds the thermal Doppler width whereas for the D2 line this is note the case.

## A.2 Transition probability of the D1 line

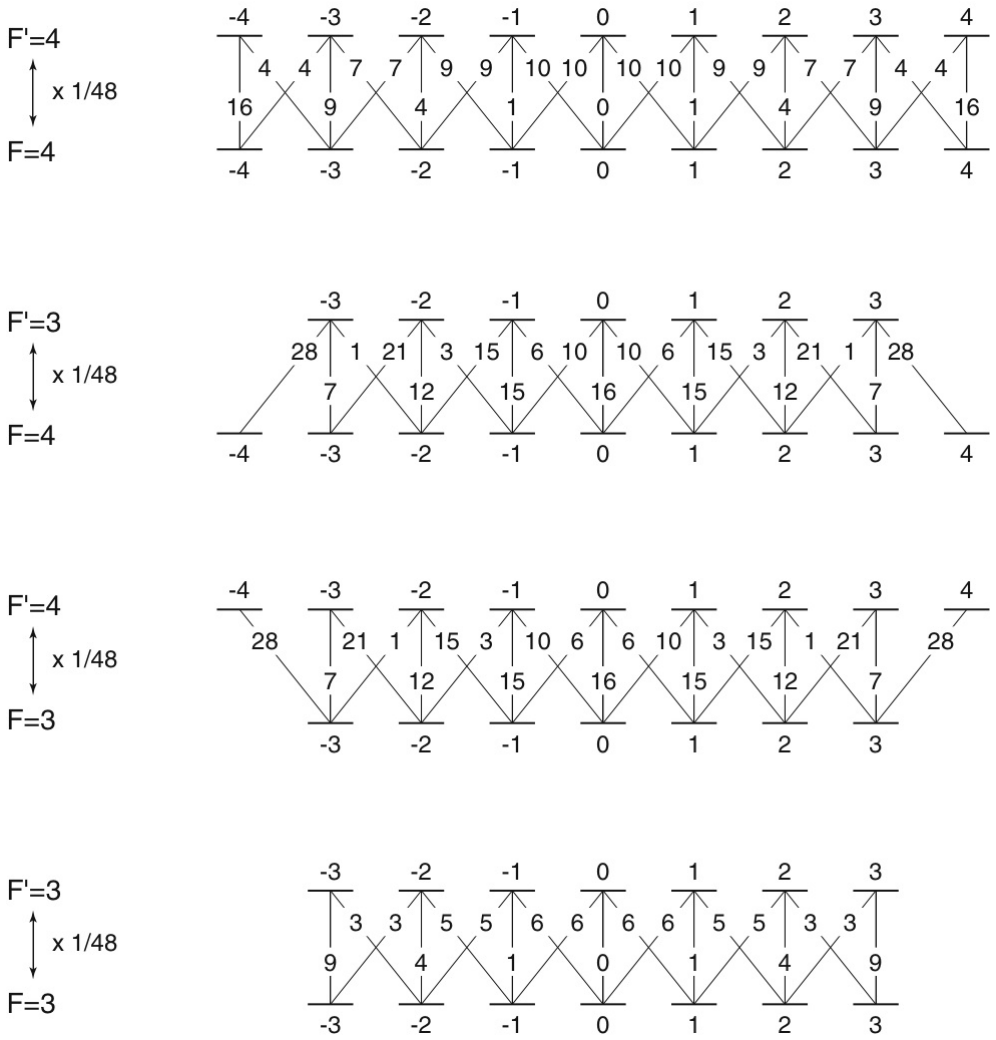


**Figure A.2**: Probability amplitudes $\left(cg_{m_F}^{\Delta m_{F'}}\right)^2$ for electric dipole transitions between Zeeman sub-levels of the $^{133}$Cs D1 line. The probability is normalised to the transition $|F = 4, m_F = 4\rangle \Leftrightarrow |F' = 5, m_{F'} = 5\rangle$ of the D2 line. $F$ is the hyperfine level, $m_F$ the Zeeman sub-level and $\Delta m_F$ the change of magnetic quantum number ($\Delta m_F$=0, $\pm$1).

## A.3 Transition probability of the D2 line

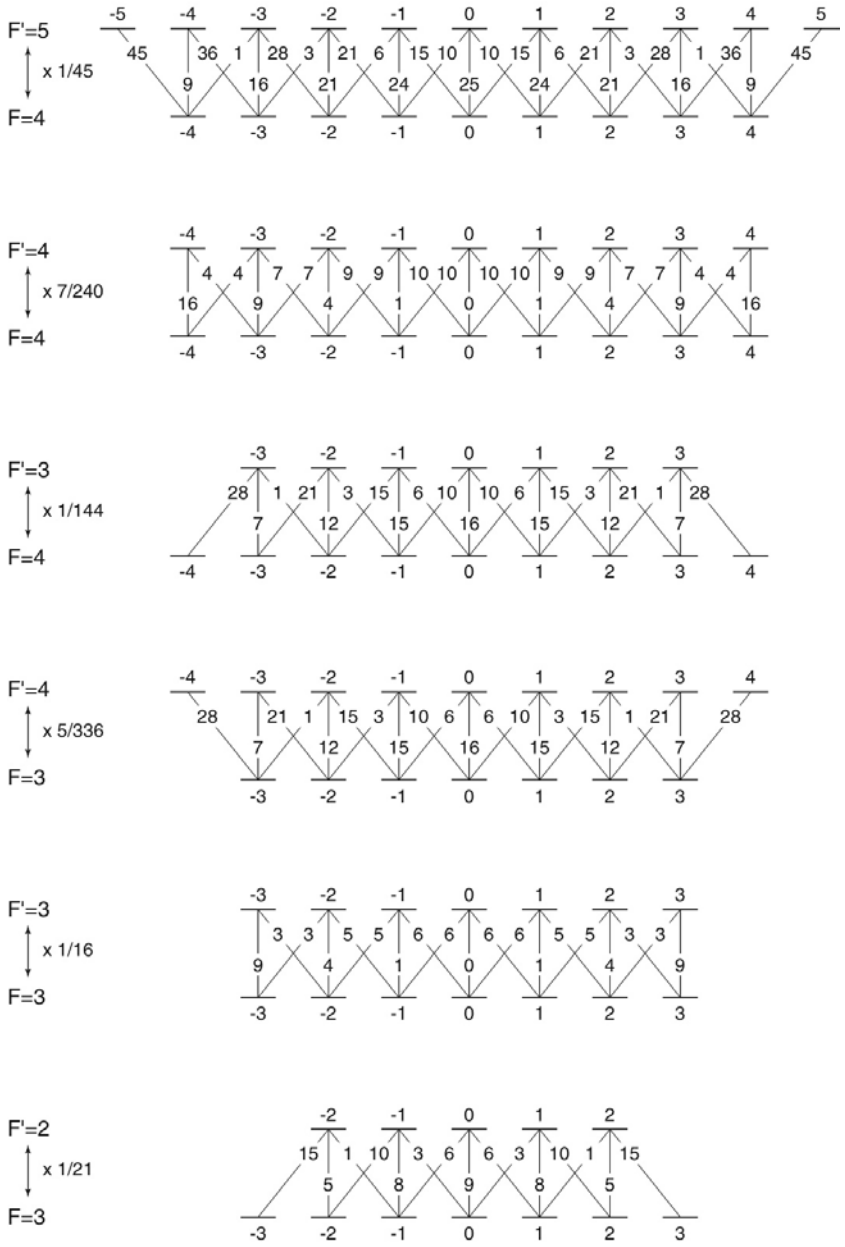


**Figure A.3**: Probability amplitude $\left(cg_{m_F}^{\Delta m_{F'}}\right)^2$ for electric dipole transitions between Zeeman sub-levels of the $^{133}$Cs D2 line. The probability is normalised to the transition $|F = 4, m_F = 4\rangle \Leftrightarrow |F' = 5, m_{F'} = 5\rangle$. $F$ is the hyperfine level, $m_F$ the Zeeman sub-level and $\Delta m_F$ the change of magnetic quantum number ($\Delta m_F$=0, ±1).

## A.4 Branching ratio and relative transition strengths

When the atom is unpolarised we cannot use the amplitudes given in the previous section to calculate the transition probability. We have instead to take the value of the coefficients $\left(cg_{m_F}^{\Delta m_{F'}}\right)^2$ averaged over all the Zeeman sub-levels involved. We obtain in this way the branching ratio $a_{e'g}$ for spontaneous emission and the relative transition strengths for absorption $w_{ge'}$ and stimulated emission $w_{e'g}$. Here $g$ stands for the ground state and $e'$ the excited state.

$$w_{ge'} = \frac{1}{2F+1} \sum_{\substack{m_F \\ \Delta m_{F'}=0}} \left(cg_{m_F}^{\Delta m_{F'}}\right)^2 \tag{A.1a}$$

$$w_{e'g} = w_{ge'} \tag{A.1b}$$

$$a_{e'g} = \frac{1}{2F'+1} \sum_{\substack{m_F \\ \Delta m_{F'}=0,\,\pm 1}} \left(cg_{m_F}^{\Delta m_{F'}}\right)^2 \tag{A.1c}$$

In the following subsections we give the values corresponding to the mean transition probability in emission and absorption for both cesium D1 and D2 lines.
Note that while in Eq. (A.1c) the expression is summed over the three possible electric dipole transitions $\pi$, $\sigma^+$ and $\sigma^-$, in Eqs. (A.1a) and (A.1b) it is calculated for only one of the three transitions (we have considered the transition $\pi$).

### A.4.1 D1 line

Tables A.2 and A.3 give respectively the relative transitions strengths and the branching ratio for the hyperfine components of the D1 line.

**Table A.2**: Relative transition strengths in absorption $w_{ge'}$ and in stimulated emission $w_{e'g}$ between a ground state $g$ and an excited state $e'$ for the $^{133}$Cs D1 line.

| $w_{ge'} = w_{e'g}$ | $F'=3$ | $F'=4$ |
|---|---|---|
| F=3 | 1/12 | 1/4 |
| F=4 | 7/36 | 5/36 |

**Table A.3**: Branching ratio in spontaneous emission $w_{e'g}$ between an excited state $e'$ and a ground state $g$ for the $^{133}$Cs D1 line.

| $a_{e'g}$ | $F'=3$ | $F'=4$ |
|---|---|---|
| F=3 | 1/4 | 7/12 |
| F=4 | 3/4 | 5/12 |

### A.4.2 D2 line

Tables A.4 and A.5 give respectively the relative transitions strengths and the branching ratio for the hyperfine components of the D2 line.

**Table A.4**: Relative transition strengths in absorption $w_{ge'}$ and in stimulated emission $w_{e'g}$ between a ground state $g$ and an excited state $e'$ for the $^{133}$Cs D2 line..

| $w_{ge'}=w_{e'g}$ | $F'=2$ | $F'=3$ | $F'=4$ | $F'=5$ |
|---|---|---|---|---|
| F=3 | 5/21 | 1/4 | 5/28 | 0 |
| F=4 | 0 | 7/108 | 7/36 | 11/27 |

**Table A.5**: Branching ratio in spontaneous emission $w_{e'g}$ between an excited state $e'$ and a ground state $g$ for the $^{133}$Cs D2 line.

| $a_{e'g}$ | $F'=2$ | $F'=3$ | $F'=4$ | $F'=5$ |
|---|---|---|---|---|
| F=3 | 1 | 3/4 | 5/12 | 0 |
| F=4 | 0 | 1/4 | 7/12 | 1 |

# Appendix B

# Light shift in FOCS1

In this Appendix we make a calculation of the relative frequency shift due to the light in the source region and in the detection region seen by the atoms during their interaction with the microwave field.

## B.1 Light shift calculation

The frequency shift $\Delta\nu = (\nu_{F=4} - \nu_{F=3})$ of the cesium hyperfine ground states relative to the clock frequency $\nu_0$ due to the perturbation of a light field is given by the formula:

$$\frac{\Delta\nu}{\nu_0} = \frac{1}{h\nu_0} \cdot \frac{\hbar \cdot \delta \cdot \ s_0}{1 + 4\frac{\delta^2}{\Gamma^2}} \tag{B.1}$$

where $s_0$ is the saturation parameter, $\delta$ the frequency detuning and $\Gamma$ the D2 line natural width already introduced. Because $F = 3$ is not coupled to the light field, whose frequency is near the $F = 4 \ \Rightarrow \ F = 5$ atomic resonance, this perturbation acts only on the $F = 4$ ground state. Fig. B.1 shows the light shift curve (calculated by using the parameters reported in Tab. B.1) as a function of the atom relative velocity $v_r$ calculated for a light intensity of 1 W·m$^{-2}$ and integrated over the natural width of the source atoms.

**Table B.1**: Parameters used to calculate the light shift in FOCS1.

| | Notation | Value |
|---|---|---|
| Atomic resonance | $\omega \ (F = 4 \ \Rightarrow \ F' = 5)$ | $2\pi{\cdot}352{\cdot}10^{12}$ Hz |
| Launch velocity | $v_0$ | 3.8 m·s$^{-1}$ |
| Distance cavity-source | $H_{cs}$ | 449 mm |
| Distance cavity-detection | $H_{cd}$ | 444 mm |

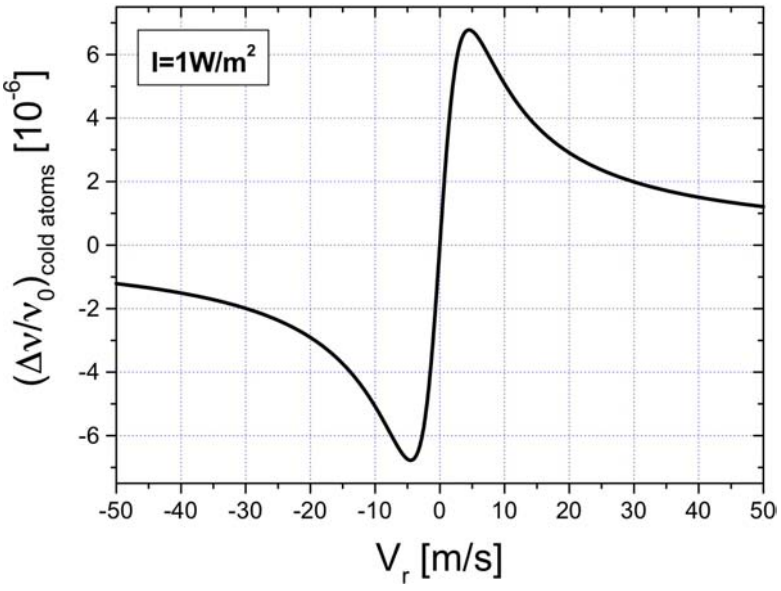


**Figure B.1**: Light shift due to the cold atoms calculated by using the parameters reported in Tab. B.1. The curve is calculated for a light intensity of 1 W·m$^{-2}$.

### B.1.1 Light shift due to the source light

We have already calculated the relative frequency shift of the hyperfine ground state $F = 4$ due to the fluorescent light emitted by the cold atoms in the region of the source. Fig. B.2 shows the part of the light shift curve of interest as a function of the atom relative velocity $v_r$ calculated for a light intensity of 1 W·m$^{-2}$. At the level of the microwave cavity ($H_{cs}$=449 mm) the cold atomic beam velocity is of 2.5 m·s$^{-1}$, thus $v_r$=1.3 m·s$^{-1}$. The measured fluorescent light intensity due to the 3D-optical molasses laser beams seen by the atoms during the interaction with the microwave is $\sim$4.8·10$^{-7}$ W·m$^{-2}$, which yields a light shift of +1.7·10$^{-12}$ (blue shift). The introduction of the light trap already presented in Chap. 1 will attenuate this undesired frequency shift of a factor $\sim$10$^4$ thus the frequency accuracy will be not limited by the uncertainty due to this effect.

### B.1.2 Light shift due to the detection light

If we consider now the detection region, the situation is symmetric with respect to the previous case. The fluorescent light due to the probe laser beam seen by the atoms during the microwave interaction yields this time a red frequency shift (the cold atomic beam relative velocity is $v_r$=-1.3 m·s$^{-1}$). In Fig. B.3 we have reported the part of the light shift curve of interest, always for a light intensity of 1 W·m$^{-2}$. Let's calculate the light shift induced by the detected atomic flux $\Phi$ of FOCS1, equal to 2·10$^5$at·s$^{-1}$. The light power

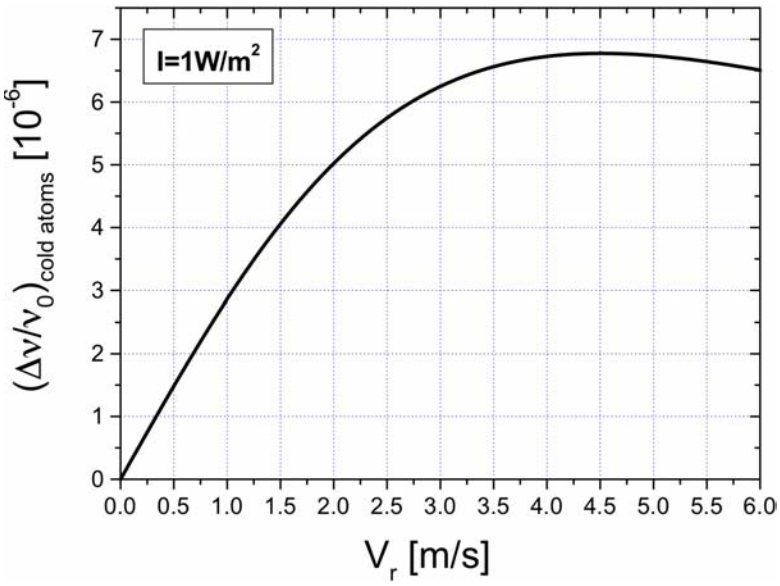


**Figure B.2**: Light shift due to the cold atoms calculated by using the parameters reported in Tab. B.1. The curve is calculated for a light intensity of 1 W·m$^{-2}$.

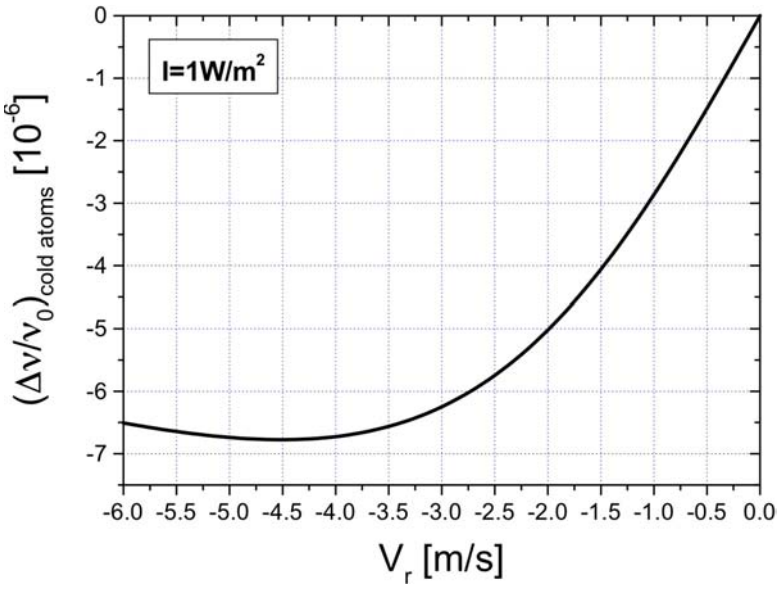


**Figure B.3**: Light shift due to the cold atoms calculated by using the parameters reported in Tab. B.1. The curve is calculated for a light intensity of 1 W·m$^{-2}$.

associated to this flux is given by:

$$P = \gamma_p \cdot \ t_{transit} \cdot \Phi \cdot \hbar\omega \tag{B.2}$$

where $\gamma_p$ is the scattering rate and $t_{transit}$ the transit time of the atoms through the probe laser beam. The probe laser beam (whose frequency $\omega/2\pi$ is locked on the atomic transition $F = 4 \ \Rightarrow \ F' = 5$) has a gaussian shape with $\sigma$=2.5 mm and a diameter of 8 mm fixed by a diaphragm. The total power is 2 mW and the polarisation is $\sigma^+$. By replacing these values into the Eq. B.2 we find $P = 1.2{\cdot}10^{-9}$ W. The light intensity $I$ measured at the level of the microwave cavity, at a distance $H_{cd}$=444 mm from the detection region, is given by:

$$I = \frac{P}{4\pi \ H_{cd}^2} \tag{B.3}$$

where we make the conservative hypothesis that all the light in the detection region can be seen from the Ramsey cavity. We find $I$=$4.8{\cdot}10^{-10}$ W$\cdot$m$^{-2}$. With this value of the light intensity and for $v_r$=-1.3 m$\cdot$s$^{-1}$ finally we obtain a light shift of -$1.7{\cdot}10^{-15}$ (red shift).

# Appendix C

# Publications and Conferences

In this Appendix we list the papers published during this work and the conferences where we have presented our results.

## C.1 Publications


[31] N. Castagna, J. Guéna, M.D. Plimmer and P. Thomann, *"A novel simplified two-dimensional magneto-optical trap as an intense source of slow cesium atoms"*, accepted by Eur. Phys. Jour. Appl. Phys. (2006).

[12] G. Di Domenico, N. Castagna, M.D. Plimmer, A.V. Taichenachev, P. Thomann and V.I. Yudin, *"On the stability of optical lattices"*, Laser Physics 15, No. 12, pp. 1674-1679 (2005).

[25] M.D. Plimmer, N. Castagna, G. Di Domenico, A.V. Taichenachev, P. Thomann and V.I. Yudin, *"2D laser collimation of a cold Cs beam induced by a transvers B-field"*, JETP Lett. 82, pp. 18-22 (2005).

[14] G. Di Domenico, N. Castagna, G. Mileti, A.V. Taichenachev, P. Thomann and V.I. Yudin, *"Laser collimation of a continuous beam of cold atoms using Zeeman-shift-degenerate-Raman-sideband cooling"*, Phys. Rev. A. 69, 063403 (2004).

## C.2 Conferences

- ✓ N. Castagna, J. Guéna, M.D. Plimmer and P. Thomann *"Low velocity, high flux, continuous source of cesium atoms"*, Proceedings of the 20th European Forum of Time and Frequency (EFTF), 27-30 March 2006, Braunschweig, (Germany) (2006).

- ✓ N. Castagna, J. Guéna, M.D. Plimmer and P. Thomann, *"Piège magnéto-optique bidimensionnel original pour le chargement efficace d'une mélasse mouvante"*, Société Franaises de Physique (SFP), 29 August-2 September 2005, Lille (France) (2005).

- ✓ N. Castagna, J. Guéna, M.D. Plimmer and P. Thomann, *"Novel inexpensive two-dimensional magneto-optical trap for efficient loading of a moving molasses"*, European Group of Atomic System (EGAS), 3-6 July 2005, Dublin (Ireland) (2005).

- ✓ N. Castagna, G. Di Domenico, G. Dudle, F. Füzesi, M.D. Plimmer, A.V. Taichenachev, P. Thomann and V.I. Yudin, *"Two-dimensional collimation of a continuous cesium fountain in an optical lattice"*, Proceedings of the 19th European Forum of Time and Frequency (EFTF), 21-24 March 2005, Besanon (France) (2005).

- ✓ M.D. Plimmer, G. Di Domenico, N. Castagna, G. Dudle, F. Füzesi, A.V. Taichenachev, P. Thomann and V.I. Yudin, *"Improving the stability of a continuous cesium fountain clock by increasing the useful atomic flux"*, 17th International Conference on Laser Spectroscopy (ICOLS), 21-25 June 2005, Cairngorms (Scotland) Technical Digest, pp. D6. (2005).

- ✓ N. Castagna, G. Di Domenico, G. Dudle, M.D. Plimmer, A.V. Taichenachev, P. Thomann and V.I. Yudin, *"Two-dimensional collimation of a continuous cesium fountain in an optical lattice induced by a transverse magnetic field"*, ICONO, (2005).

- ✓ N. Castagna, G. Di Domenico, M.D. Plimmer, A.V. Taichenachev, P. Thomann and V.I. Yudin, *"Transverse cooling of a continuous cold Cs beam in a 2D optical lattice"*, International Conference on Atomic Physics (ICAP), 25-30 July 2004, Rio de Janeiro (Brazil) (2004).

- ✓ N. Castagna, G. Di Domenico, G. Dudle, M.D. Plimmer, A.V. Taichenachev, P. Thomann and V.I. Yudin, *"Collimation of a continuous cold atomic beam using Raman sideband laser cooling"*, Proceedings of the 18th EFTF, 5-7 April 2004, Guildford (England) (2004).

- ✓ G. Di Domenico, N. Castagna, and P. Thomann, *"Collimation of a continuous cold atomic beam using Raman sideband laser cooling"*, Swiss Physical Society (SPS), 4 March 2004, Neuchtel (Switzerland), (2004).

- ✓ A. Joyet, N. Castagna, P. Thomann, G. Dudle, C. Mandache and T. Acsente, *"Metrological aspects of the ON-METAS continuous fountain standard"*, Proceedings of the joint meeting IEEE-FCS/17th EFTF, 5-8 May 2003, Tampa (Florida) (2003).

- ✓ G. Dudle, A. Joyet, N. Castagna, G. Mileti, P. Thomann, C. Mandache and T. Acsente, *"Preliminary evaluation of the ON-METAS continuous fountain standard"*, Proceedings of the 16th EFTF, 12-14 March 2002 (St. Petersburg State University of Aerospace Instrumentation, Russia), St. Petersburg, E-014 - E-016 (2002).

# Bibliography


[1] P.R. Berman. *Atom Interferometry.* Academic Press, 1997.

[2] H. Metcalf and P. van der Straten. *Laser cooling and trapping.* Springer, 1999.

[3] Y. Sortais, S. Bize, M. Abgrall, S. Zhang, C. Nicolas, C. Mandache, P. Lemonde, P. Laurent, G. Santarelli, N. Dimarcq, P. Petit, A. Clairon, A. Mann, A. Luiten, S. Chang, and C. Salomon. Cold atom clocks *Physica Scripta.* **50**, 50 (2001).

[4] R. Wynands and S. Weyers. Atomic fountain clocks *Metrologia.* **42**, S64–S79 (2005).

[5] P. Berthoud. *Développement d'une source continue d'atomes de césium refroidis par laser.* PhD thesis, Université de Neuchâtel, 2000.

[6] C. Vian, P. Rosenbusch, H. Marion, S. Bize, L. Cacciapuoti, S. Zhang, M. Abgrall, D. Chambon, I. Maksimovic, P. Laurent, G. Santarelli, A. Clairon, A. Luiten, M. Tobar, and C. Salomon. BNM-SYRTE Fountains :Recent Results *IEEE Trans. Instr. Meas.* **54**, 833 (2005).

[7] A. Joyet, G. Mileti, P. Thomann, and G. Dudle. Theoretical study of the Dick effect in a continuously operated Ramsey resonator *IEEE Trans. Instr. Meas.* **50**, 150–156 (2001).

[8] A. Joyet. *Aspects métrologiques d'une fontaine continue à atomes froids.* PhD thesis, Université de Neuchâtel, 2003.

[9] G. Dudle, A. Joyet, N. Castagna, G. Mileti, P. Thomann, C. Mandache, and T. Acsente. Preliminary evaluation of the ON-METAS continuous fountain standard. In *Proceedings of the 16th EFTF, St. Petersburg*, pages E–014 – E–016. St. Petersburg State University of Aerospace Instrumentation, Russia, 2002.

[10] G. Di Domenico. *Collimation d'un jet continu d'atomes de césium par refroidissement laser.* PhD thesis, Université de Neuchâtel, 2004.

[11] A.V. Taichenachev, A.M. Tumaikin, V.I. Yudin, and L. Hollberg. Two-dimensional sideband Raman cooling and Zeeman state preparation in an optical lattice *Phys. Rev. A.* **63**, 033402 (2001).

[12] G. Di Domenico, N. Castagna, M.D. Plimmer, P. Thomann, A.V. Taichenachev, and V.I. Yudin. On the stability of optical lattices *Laser Physics.* **15**, 1674–1679 (2005).

[13] A. Rauschenbeutel, H. Schadwinkel, V. Gomer, and D. Meschede. Standing light fields for cold atoms with intrinsically stable and variable time phases *Opt. Commun.* **148**, 45–48 (1998).

[14] G. Di Domenico, N. Castagna, G. Mileti, P. Thomann, A.V. Taichenachev, and V.I. Yudin. Laser collimation of a continuous beam of cold atoms using Zeeman-shift degenerate-Raman-sideband cooling *Phys. Rev. A.* **69**, 063403 (2004).

[15] S. Ghezali, Ph. Laurent, S.N. Lea, and A. Clairon. An experimental study of the spin-exchange frequency shift in a laser-cooled cesium fountain frequency standard *Europhys. Lett.* **36**, 25–30 (1996).

[16] K. Gibble and S. Chu. Laser-cooled Cesium Frequency Standard and a Measurement of the Frequency Shift due to Ultracold Collisions *Phys. Rev. Lett.* **70**, 1771 – 1774 (1993).

[17] P. Berthoud, E. Fretel, and P. Thomann. Bright, slow and continuous beam of laser-cooled cesium atoms *Phys. Rev. A.* **60**, R4241–R4244 (1999).

[18] N. Castagna, G. Di Domenico, G. Dudle, F. Füzesi, M.D. Plimmer, A.V. Taichenachev, P. Thomann, and V.I. Yudin. Two-dimensional collimation of a continuous cesium fountain in an optical lattice. In *Proceedings of the 19th EFTF*, pages 267–272, 2005.

[19] D. Boiron, C. Triché, D.R. Meacher, P. Verkerk, and G. Grynberg. Three-dimensional cooling of cesium atoms in four-beam gray optical molasses *Phys. Rev. A.* **52**, R3425R3428 (1995).

[20] D. Boiron, A. Michaud, P. Lemonde, Y. Castin, C. Salomon, S. Weyers, K. Szymaniec, L. Cognet, and A. Clairon. Laser cooling of cesium atoms in gray optical molasses down to 1.1$\mu$k *Phys. Rev. A.* **53**, R3734R3737 (1996).

[21] C. Triché, P. Verkerk, and G. Grynberg. Blue-Sisyphus cooling in cesium gray molasses and antidot lattices *Eur. Phys. J. D.* **5**, 225–228 (1999).

[22] C. Triché, D. Boiron, S. Guibal, D.R. Meacher, P. Verkerk, and G. Grynberg. Cesium atoms in grey optical lattices. study of temperature and capture efficiency *Opt. Commun.* **126**, 49–54 (1996).

[23] C. Triché. *Refroidissement et dynamique d'atomes dans des potentiels lumineux: mélasses grises, réseaux de plots et réseaux brillants.* PhD thesis, École Polytechnique de Paris, 1997.

[24] J. Dalibard and C. Cohen-Tannoudji. Laser cooling below the Doppler limit by polarization gradients: simple theoretical models *J. Opt. Soc. Am. B.* **6**, 2023 –2045 (1989).

[25] M.D. Plimmer, N. Castagna, G. Di Domenico, P. Thomann, A.V. Taichenachev, and V.I. Yudin. 2D laser collimation of a cold Cs beam induced by a transverse B-field *JETPL.* **82**, 18–22 (2005).

[26] B. Sheehy, S-Q. Shang, P. van der Straten, and H. Metcalf. Collimation of a rubidium beam below the Doppler limit *Chemical Physics.* **145**, 317 (1990).

[27] P. van der Straten, S-Q. Shang, B. Sheehy, H. Metcalf, and G. Nienhuis. Laser cooling at low intensity in a strong magnetic field *Phys. Rev. A.* **47**, 4160 – 4175 (1993).

[28] R. Gupta, S. Padua, C. Xie, H. Batelaan, and H. Metcalf. Simplest atomic system for sub-Doppler laser cooling *J. Opt. Soc. Am. B.* **11**, 537–541 (1994).

[29] S. Pádua. *Laser cooling and slowing of rubidium.* PhD thesis, SUNY, Stony Brook, 1993.

[30] C. Valentin, M.-C. Gagné, J. Yu, and P. Pillet. One-dimension sub-Doppler molasses in the presence of static magnetic field *Europhys. Lett.* **17**, 133 – 128 (1992).

[31] N. Castagna, J. Guéna, M.D. Plimmer, and P. Thomann. A novel simplified two-dimensional magneto-optical trap as an intense source of slow cesium atoms *accepted by EPJAP.* –, – (2006).

[32] J. Stuhler, M. Fattori, T. Petelski, and G.M. Tino. Magia: using atom interferometry to determine the Newtonian gravitational constant *J. Opt. B: Quantum Semiclass. Opt.* **5**, S75–S81 (2003).

[33] T. Petelski. *Atom Interferometers for Precision Gravity Measurements.* PhD thesis, Université Paris 6 and Università degli Studi di Firenze, 2005.

[34] P. Cheinet, F. Pereira Dos Santos, T. Petelski, J. Gouët, K.T. Therkildsen, A. Clairon, and A. Landragin. Transportable laser system for atom interferometry, ccsd-00012840 v1, 2005.

[35] S. Chelkowski. *Aufbau eines atomaren Sagnac-Interferometers zur hochauflösenden Rotationsmessung.* Diplomarbeit, Institut of Quantum Physics, University of Hannover, 2002.

[36] S. Sanguinetti, J. Guéna, M. Lintz, Ph. Jacquier, A. Wasan, and M.-A. Bouchiat. Prospects for forbidden-transition spectroscopy and parity violation measurements using a beam of cold stable or radioactive atoms *Eur. Phys. J. D.* **25**, 3–13 (2003).

[37] V. Natarajan. Proposed search for an electric-dipole moment using laser-cooled $^{171}Yb$ atoms *Eur. Phys. J. D.* **32**, 33–38 (2005).

[38] J. Vanier. Atomic clocks based on coherent population trapping: a review *Appl. Phys. B.* **81**, 421–442 (2005).

[39] A. Grabowski, R. Heidemann, R. Löw, J. Stuhler, and T. Pfau. High Resolution Rydberg Spectroscopy of Ultracold Rubidium Atoms, arXiv:quant-ph/0508082 v1, 2005.

[40] A. Camposeo, A. Piombini, F. Cervelli, F. Tantussi, F. Fuso, and E. Arimondo. A cold cesium atomic beam produced out of a pyramidal funnel *Opt. Commun.* **200**, 231–239 (2001).

[41] M.A. Joffe, W. Ketterle, A. Martin, and D.E. Pritchard. Transverse cooling and deflection of an atomic beam inside a Zeeman slower *J. Opt. Soc. Am. B.* **10**, 2257–2262 (1993).

[42] J. Kohel, J. Ramirez-Serrano, R.J. Thompson, L. Maleki, J.L. Bliss, and K.G. Libbrecht. Generation of an intense cold-atom beam from a pyramidal magneto-optical trap: experiment and simulation *J. Opt. Soc. Am. B.* **20**, 1161–1168 (2003).

[43] L. Cacciapuoti, A. Castrillo, M. de Angelis, and G.M. Tino. A continuous cold atomic beam from a magneto-optical trap *Eur. Phys. J. D.* **15**, 245–249 (2001).

[44] H. Wang and W.F. Buell. Velocity-tunable magneto-optical-trap-based cold Cs atomic beam *J. Opt. Soc. Am. B.* **20**, 2025–2030 (2003).

[45] R.N. Watts and C.E. Wieman. Manipulating atomic velocities using diode lasers *Opt. Lett.* **11**, 291–293 (1986).

[46] Y.B. Ovchinnikov. Compact magneto-optical sources of slow atoms *Opt. Commun.* **249**, 473–481 (2005).

[47] Z.T. Lu, K.L. Corvin, M.J. Renn, M.H. Anderson, E.A. Cornell, and C.E. Wieman. Low-velocity intense source of atoms from a magneto-optical trap *Phy. Rev. Lett.* **77**, 3331–3334 (1996).

[48] H. Chen and E. Riis. Cold atomic beam from a rubidium funnel *Appl. Phys. B.* **70**, 665–670 (2000).

[49] P. Berthoud, A. Joyet, G. Dudle, N. Sagna, and P. Thomann. A continuous beam of slow, cold cesium atoms magnetically extracted from a 2D magneto-optical trap *Europhys. Lett.* **41**, 141–146 (1998).

[50] P. Cren, C.F. Roos, A. Aclan, J. Dalibard, and D. Guéry-Odelin. Loading of a cold atomic beam into a magnetic guide *Eur. Phys. J. D.* **20**, 107–116 (2002).

[51] J. Schoser, A. Batär, R. Löw, V. Schweikhard, A. Grabowski, Y.B. Ovchinnikov, and T. Pfau. Intense source of cold Rb atoms from a pure two-dimensional magneto-optical trap *Phys. Rev. A.* **66**, 023410 (2002).

[52] K. Dieckmann, R.J.C. Spreeuw, M. Weidemüller, and J.T.M. Walraven. Two-dimensional magneto-optical trap as a source of slow atoms *Phys. Rev. A.* **58**, 3891–3895 (1998).

[53] C.J. Foot. *Atomic Physics.* Oxford, 2005.

[54] N. Sagna. *Refroidissement d'atomes de césium: étude expérimentale et théorique sur les caractéristiques du piégeage.* PhD thesis, Université de Neuchâtel, 1996.

[55] S. Lecomte, E. Fretel, G. Mileti, and P. Thomann. A self-aligned extended-cavity diode laser stabilized by Zeeman effect on Cesium $D_2$ line *Appl. Opt.* **39**, 1426–1429 (2000).

[56] D.A. Steck Los Alamos National Laboratory. Cesium D line data, http://steck.us/alkalidata, Rb and Na data are available there, 2002.